Materials Characterization 147 (2019) 464–511

Contents lists available at ScienceDirect

Materials Characterization

journal homepage: www.elsevier.com/locate/matchar

Review

# *Ab initio* phase stabilities and mechanical properties of multicomponent alloys: A comprehensive review for high entropy alloys and compositionally complex alloys

Yuji Ikeda[a,b,*], Blazej Grabowski[a], Fritz Körmann[a,c]

[a] Computational Materials Design Department, Max-Planck-Institut für Eisenforschung GmbH, Düsseldorf 40237, Germany
[b] Department of Materials Science and Engineering, Kyoto University, Kyoto 606-8501, Japan
[c] Materials Science and Engineering, Delft University of Technology, CD Delft 2628, Netherlands

ARTICLE INFO

*Keywords:*
High entropy alloys
Compositionally complex alloys
First principles
Phase stability and thermodynamic properties
Mechanical properties
Comprehensive overview and review

ABSTRACT

Multicomponent alloys with multiple principal elements including high entropy alloys (HEAs) and compositionally complex alloys (CCAs) are attracting rapidly growing attention. The endless possibilities to explore new alloys and the hope for better combinations of materials properties have stimulated a remarkable number of research works in the last years. Most of these works have been based on experimental approaches, but *ab initio* calculations have emerged as a powerful approach that complements experiment and serves as a predictive tool for the identification and characterization of promising alloys.

The theoretical *ab initio* modeling of phase stabilities and mechanical properties of multi-principal element alloys by means of density functional theory (DFT) is reviewed. A general thermodynamic framework is laid down that provides a bridge between the quantities accessible with DFT and the targeted thermodynamic and mechanical properties. It is shown how chemical disorder and various finite-temperature excitations can be modeled with DFT. Different concepts to study crystal and alloy phase stabilities, the impact of lattice distortions (a core effect of HEAs), magnetic transitions, and chemical short-range order are discussed along with specific examples. Strategies to study elastic properties, stacking fault energies, and their dependence on, e.g., temperature or alloy composition are illustrated. Finally, we provide an extensive compilation of multi-principal element alloys and various material properties studied with DFT so far (a set of over 500 alloy-property combinations).

## 1. Introduction

Multicomponent alloys with multiple principal elements — including the class of high entropy alloys (HEAs) and compositionally complex alloys (CCAs) — have attracted remarkable attention in the last decade from both experimentalists and theoreticians. This is evidenced by the exponentially growing number of research articles on these alloys shown in Fig. 1. Originally, HEAs were loosely defined as single-phase solid solutions with at least five principal elements each with an atomic concentration between 5% and 35% (see, e.g., Refs. [1-3]). These alloys owe their name to the assumption that the solid solution is stabilized by a high configurational entropy of mixing. Meanwhile, the definition has been broadened to also include four-component alloys. Alloys with three and four principal elements are sometimes referred to as medium entropy alloys [4]. More recently, interest has emerged in multi-principal element alloys forming secondary phases and these alloys have been generally called CCAs.

Although the field of multi-principal element alloys is still comparably young — the seminal works by Yeh et al. [5] and Cantor et al. [6] are less than 15 years old — the underlying key concept of exploring the previously unknown compositional space has stimulated not only an amazing number of original research articles (Fig. 1) but already two books and more than thirty review papers (see Table 1). In 2017, the number of research articles published per year reached 300, mainly dominated by experimental studies. It is, however, clear that the immense compositional space spanned by HEAs and CCAs cannot be explored by experimental efforts alone.

A particularly important computational tool is first-principles, i.e., *ab initio*, calculations. Such calculations are based only on quantum mechanical laws and natural constants and enable thus the prediction and investigation of materials properties without empirical input. The most common practical realization of *ab initio* calculations is density

* Corresponding author at: Computational Materials Design Department, Max-Planck-Institut für Eisenforschung GmbH, Düsseldorf 40237, Germany.
*E-mail address:* y.ikeda@mpie.de (Y. Ikeda).

https://doi.org/10.1016/j.matchar.2018.06.019
Received 7 March 2018; Received in revised form 30 May 2018; Accepted 13 June 2018
Available online 20 June 2018

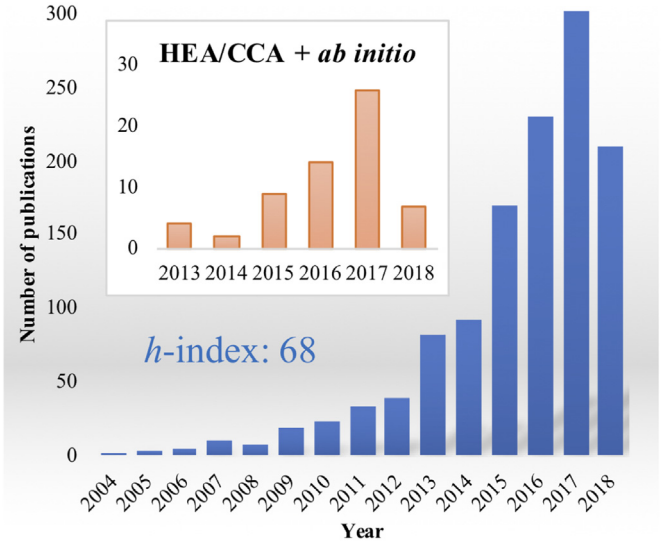


**Fig. 1.** Number of published articles on HEAs and CCAs until the present (mid-2018). Inset: Works including *ab initio* calculations. Source: Web of Science. Employed keywords: "high entropy alloy" OR "compositionally complex alloy" OR "concentrated solid solution". For *ab initio* works in addition: "density functional theory" OR "*ab initio*" OR "first principles". Created on 14.05.2018.

functional theory (DFT) [40] in the Kohn-Sham formalism [41] in which the quantum mechanical many-electron Schrödinger equation is mapped onto an effective one-electron problem utilizing the electron density as a key variable. DFT has become one of the dominant approaches in theoretical solid state physics for exploring materials properties [42,43]. It is therefore not surprising that, with some delay, DFT calculations also entered the field of HEAs and CCAs and that the number of corresponding studies is now greatly increasing, see inset in Fig. 1. To the best of our knowledge, previous *ab initio* works on HEAs/CCAs have been exclusively based on DFT calculations and we will take the liberty to use the two terms, *ab initio* and DFT, interchangeably in most of our survey.

In practice, the DFT formalism comes along with an inherent limitation. The exchange-correlation functional of the electron density is not known exactly and must be approximated. The two most frequently used approximations are the local density approximation (LDA) [44,45] and the generalized gradient approximation (GGA) [46,47]. For selected unaries and ordered compounds, LDA and GGA (partly including the +U correction) have been shown to provide an *ab initio* confidence interval for experimental materials properties [48-51]. As for HEAs and CCAs, the vast majority of studies have employed GGA. One reason is that many of the interesting alloys are magnetic and thus require a treatment with the spin-polarized version of DFT [52]. One of the early successes of GGA was the correct prediction of ferromagnetic bcc as the ground state of Fe, while LDA is notorious for predicting the wrong ground state (non-magnetic fcc) [53]. In this respect, it is important to note that the non-magnetic (spin unpolarized) version of DFT is generally not applicable to study materials in the paramagnetic regime where, despite the loss of long-range magnetic order, finite local magnetic moments are preserved. Part of our review will deal with different approaches to simulate HEAs and CCAs in the paramagnetic state and to predict the critical magnetic ordering temperature.

DFT in its original formulation is a ground state theory, i.e., strictly speaking DFT only provides the ground state energy at 0 K for a given configuration of atoms. Finite-temperature excitations such as, e.g., lattice vibrations are not *a priori* included. Fortunately, DFT can be combined with thermodynamic concepts and statistical sampling techniques allowing us to bridge from 0 K towards finite temperatures. A major part of this review will introduce the necessary tools for that purpose.

The overarching goal of the present work is to provide a comprehensive overview of the key theoretical concepts for simulating HEAs and CCAs and their properties from *ab initio* with a focus on phase stabilities (Section 3) and mechanical properties (Section 4). Along with this discussion of the theory, we provide a comprehensive review of the original works on the relevant topics. An extensive compilation of multi-principal element alloys investigated up to now with *ab initio* is presented in the Appendix in Table 9.

The general thermodynamic framework for multicomponent alloys and its relation to *ab initio* simulations is laid down in Section 2. Building upon this framework, Section 3 discusses phase stabilities. Specifically, in Section 3.1, challenges related to phase decomposition are described. A generic feature of HEAs and CCAs is their chemical randomness and we introduce different techniques to cope with chemical disorder within DFT in Section 3.2. Practical approaches for including finite-temperature effects due to electronic excitations, magnetic excitations, and lattice vibrations in multicomponent alloys are at the heart of Section 3.3. More elaborate *ab initio* techniques for capturing vibrations of random solid solutions are summarized in Section 3.4. Magnetic properties of HEAs and CCAs and in particular schemes to efficiently predict the magnetic ordering temperatures are provided in Section 3.5. Lastly, Section 3.6 introduces the state-of-the-art techniques for addressing chemical short-range order and predicting chemical phase stabilities beyond the concept of ideal mixing.

Section 4 is devoted to *ab initio* concepts related to mechanical properties and it reviews related works on this topic. Most of these works focused on computing elastic properties, which is the subject of Section 4.1. Recent works suggest a relation between local lattice distortions, one of the original core effects of HEAs [2,3], and solid solution strengthening as discussed in Section 4.2. A key quantity linking atomistic simulations and hence DFT with macroscopic mechanical properties is the stacking fault energy. Corresponding simulation techniques as well as associated previous works are summarized in Section 4.3. We conclude Section 4 by reviewing recent efforts to achieve better mechanical properties that utilize *ab initio* phase stabilities in order to promote the formation of secondary phases in the spirit of CCAs (Section 4.4).

We would like to stress that the introduced concepts are based on the assumption of thermodynamic equilibrium. It should be clear that thermodynamic equilibrium may not always be attained in experiments due to kinetic limitations and thus some of the predicted phase decompositions may not be observed in experiments under realistic time scales. Unfortunately, *ab initio* works on the topics of diffusion and kinetics in multicomponent alloys are still rare and kinetic aspects will be therefore touched only very briefly at the end of Section 3.3 and will otherwise not be part of the present review. We further note that apart from *ab initio* calculations there are also a number of atomistic studies mainly based on empirical potentials which we will not discuss in this work.

We have attempted to provide a careful and comprehensive review of all the related literature, but may have unintentionally missed articles owing to the extremely rapid pace of research in this field.

## 2. General Gibbs Energy Approach

The thermodynamic stability of HEAs and CCAs is in general determined by the same thermodynamic rules that have been applied since many decades for the computation of multicomponent phase diagrams, e.g., within the CALPHAD methodology [54-56]. The central quantity is the extensive Gibbs energy of the total system, $G^{ext}(P,T,\{n_i\})$, as a function of pressure $P$, temperature $T$, and the number of moles $n_i$ for each element $i = 1, \ldots, N$ with $N$ the number of elements. For HEAs and CCAs, $N \geq 4$ typically. The total Gibbs energy is typically decomposed into a sum

**Table 1**
Books and reviews on HEAs/CCAs. Number of pages (#pp) in bold indicates *ab initio* content.

| Year | Reference | Title | #pp |
|---|---|---|---|
| 2014 | Murty et al. [2] | High-entropy alloys (book) | **218** |
| 2016 | Gao et al. [3] | High-entropy alloys: Fundamentals and applications (book) | **516** |
| 2006 | Yeh [7] | Recent progress in high-entropy alloys | 18 |
| 2007 | Yeh et al. [4] | High-entropy alloys — a new era of exploitation | 9 |
| 2011 | Guo and Liu [8] | Phase stability in high entropy alloys: Formation of solid-solution phase or amorphous phase | 14 |
| 2012 | Zhang et al. [9] | Alloy design and properties optimization of high-entropy alloys | 9 |
| 2013 | Tsai [10] | Physical properties of high entropy alloys | **8** |
| 2014 | Cantor [11] | Multicomponent and high entropy alloys | 20 |
| | Tsai and Yeh [12] | High-entropy alloys: A critical review | **17** |
| | Zhang et al. [13] | Microstructures and properties of high-entropy alloys | **93** |
| 2015 | Diao et al. [14] | Local structures of high-entropy alloys (HEAs) on atomic scales: An overview | **5** |
| | Kozak et al. [15] | Single-phase high-entropy alloys: An overview | 14 |
| | Lu et al. [16] | An assessment on the future development of high-entropy alloys: Summary from a recent workshop | 10 |
| | Troparevsky et al. [17] | Beyond atomic sizes and Hume-Rothery rules: Understanding and predicting high-entropy alloys | **14** |
| | Raabe et al. [18] | From high-entropy alloys to high-entropy steels | 12 |
| | Yeh [19] | Physical metallurgy of high-entropy alloys | 8 |
| 2016 | Pickering and Jones [20] | High-entropy alloys: A critical assessment of their founding principles and future prospects | **20** |
| | Tsai [21] | Three strategies for the design of advanced high-entropy alloys | 14 |
| | Ye et al. [22] | High-entropy alloy: Challenges and prospects | **14** |
| 2017 | Diao et al. [23] | Fundamental deformation behavior in high-entropy alloys: An overview | **15** |
| | Gao et al. [24] | Thermodynamics of concentrated solid solution alloys | **13** |
| | Gao et al. [25] | Computational modeling of high-entropy alloys: Structures, thermodynamics and elasticity | **15** |
| | Li and Raabe [26] | Strong and ductile non-equiatomic high-entropy alloys: Design, processing, microstructure, and mechanical properties | 8 |
| | Miracle [27] | High-entropy alloys: A current evaluation of founding ideas and core effects and exploring “nonlinear alloys” | 7 |
| | Miracle and Senkov [28] | A critical review of high entropy alloys and related concepts | **64** |
| | Qiu et al. [29] | Corrosion of high entropy alloys | 15 |
| | Shi et al. [30] | Corrosion-resistant high-entropy alloys: A review | 18 |
| | Tian [31] | A review of solid-solution models of high-entropy alloys based on *ab initio* calculations | **36** |
| | Toda-Caraballo et al. [32] | Simulation and modeling in high entropy alloys | **13** |
| | Wu et al. [33] | Phase stability, physical properties and strengthening mechanisms of concentrated solid solution alloys | **18** |
| | Zhang et al. [34] | Atomic-level heterogeneity and defect dynamics in concentrated solid-solution alloys | **17** |
| | Zhao et al. [35] | Unique challenges for modeling defect dynamics in concentrated solid-solution alloys | **8** |
| 2018 | Chen et al. [36] | Fatigue behavior of high-entropy alloys: A review | 11 |
| | Praveen and Kim [37] | High-entropy alloys: Potential candidates for high-temperature applications — An overview | 22 |
| | Senkov et al. [38] | Development and exploration of refractory high entropy alloys — A review | **37** |
| | Zhang et al. [39] | Science and technology in high-entropy alloys | **21** |

$$G^{\text{ext}}(P,\,T,\,\{n_i\}) = \sum_{\alpha} G_{\alpha}^{\text{ext}}(P,\,T,\,\{n_i^{\alpha}\}), \tag{1}$$

where $\alpha$ runs over the different phases that can be stabilized in the considered system (fcc A1, bcc A2, hcp A3, B1, B2, $L1_0$, …) and $G_{\alpha}^{\text{ext}}$ is the extensive Gibbs energy of phase $\alpha$ for $n_i^{\alpha}$ moles. Note that the same crystallographic structure can be sometimes stabilized at different compositions which results into different phases that need to be separately considered in Eq. (1) (e.g., fcc A1 #1, fcc A1 #2, …). Whether and how many different phases can form for a certain global composition is determined by the chemical potentials $\mu_i^{\alpha} = \partial G_{\alpha}^{\text{ext}}/\partial n_i^{\alpha}$. Only when the chemical potentials of each element are equal in different phases ($\alpha$, $\beta$, $\gamma$, …, max),

$$\begin{aligned}
\mu_1^{\alpha} &= \mu_1^{\beta} = \mu_1^{\gamma} = \cdots = \mu_1^{\max},\\
\mu_2^{\alpha} &= \mu_2^{\beta} = \mu_2^{\gamma} = \cdots = \mu_2^{\max},\\
&\vdots \qquad\quad \vdots \qquad\quad \vdots \qquad\qquad \vdots\\
\mu_N^{\alpha} &= \mu_N^{\beta} = \mu_N^{\gamma} = \cdots = \mu_N^{\max},
\end{aligned} \tag{2}$$

the phases can coexist in equilibrium. According to the Gibbs phase rule, there is a maximum number of phases that can coexist. For example, for a five-component alloy at constant pressure the maximum is six phases. (Note that the maximum number of phases can coexist only at a single invariant point in the phase diagram.) When some of the chemical potentials do not match the potentials in other phases, the number of coexisting phases is smaller. When none of the chemical potentials matches any other one, only a *single phase* will be present and the system will constitute a HEA. Otherwise, the system will be a CCA.

From a simulation perspective, it is convenient to rewrite Eq. (1) in terms of intensive, molar Gibbs energies, $G = G^{\text{ext}}/n$ and $G_{\alpha} = G_{\alpha}^{\text{ext}}/N_{\alpha}$ where $n = \sum_i n_i$ and $n_{\alpha} = \sum_i n_i^{\alpha}$, and molar fractions, $x_i = n_i/n$ and $x_i^{\alpha} = n_i^{\alpha}/n_{\alpha}$, as

$$G(P,\,T,\,\{x_i\}) = \sum_{\alpha} f_{\alpha} G_{\alpha}(P,\,T,\,\{x_i^{\alpha}\}), \tag{3}$$

where $f_{\alpha} = n_{\alpha}/n$ is the fraction of the phase $\alpha$. For a HEA, $f_{\alpha} = 1$ for a single phase while all other fractions become zero. Above equation can be also interpreted as a multi-dimensional minimization problem where, at a given $P$ and $T$, the phase fractions $f_{\alpha}$ and the phase concentrations $\{x_i^{\alpha}\}$ are optimized such as to give the minimum molar Gibbs energy $G$ ($P$,$T$, $\{x_i\}$) under the condition $\sum_{\alpha} f_{\alpha} = 1$.

A main challenge for a phenomenological theory (such as the CALPHAD approach) is to obtain $G_{\alpha}(P,\,T,\,\{x_i^{\alpha}\})$. The great advantage of *ab initio* calculations is that they can be used to compute $G_{\alpha}(P,\,T,\,\{x_i^{\alpha}\})$ without any experimental input. Typically, the Helmholtz free energy $F_{\alpha}$ is calculated first and $G_{\alpha}$ is obtained from a Legendre transformation:

$$G_{\alpha}(P,\,T,\,\{x_i^{\alpha}\}) = F_{\alpha}(V,\,T,\,\{x_i^{\alpha}\}) + PV, \tag{4}$$

where $V$ is the volume per mole. The computation of $F_{\alpha}$ requires in principle a sampling over all relevant degrees of freedom, i.e., atomic configurations, electrons, magnetism, and vibrations, including mutual coupling effects. Such a complete sampling is not possible in practice and approximations need to be introduced. Since the configurational degree of freedom is significantly slower than the remaining ones, an adiabatic decomposition (see, e.g., Ref. [57]) is a very reasonable first approximation and we thus write the free energy as

$$F_{\alpha'}(V,\,T,\,\{x_i^{\alpha'}\}) = -k_B T \ln \sum_{c\,\in\,\alpha'} \exp\left(-\frac{F_c^{\text{el,mag,vib}}(V,\,T,\,\{x_i^{\alpha'}\})}{k_B T}\right), \tag{5}$$

where $k_B$ is the Boltzmann constant and $c$ runs over different atomic configurations with corresponding free energies $F_c^{\mathrm{el,mag,vib}}$ that are evaluated from averages over the electronic, magnetic, and vibrational degrees of freedom, i.e., excluding the configurational degree of freedom. The prime in $\alpha'$ indicates that this index distinguishes only between different lattices (fcc, bcc, hcp, …) in contrast to $\alpha$ which additionally distinguishes between different chemical orderings, since by explicitly sampling over different atomic configurations (on the same lattice) the system will automatically attain the equilibrium chemical order or disorder (i.e., fcc A1 vs. $L1_0$, or bcc A2 vs. B2) in Eq. (5).

Solving Eq. (5) is a formidable task and further approximations need to be applied, typically along the following two routes. The first route focuses on the configurational degree of freedom and typically approximates $F_c^{\mathrm{el,mag,vib}}(V, T, \{x_i^{\alpha'}\})$ by the total electronic energy $E_c(V, \{x_i^{\alpha'}\})$ at $T = 0$ K for each configuration $c$. Still, further approximations and elaborate techniques are required to practically solve Eq. (5); those will be discussed in Section 3.6. The second route focuses on phases that can be reasonably well approximated by a single representative atomic configuration and for which the configurational entropy can be expressed analytically (ordered, disordered, or partially disordered phases). The majority of HEA/CCA works so far has utilized this second route and we will devote the main part of Section 3 to the corresponding techniques.

To calculate the free energy of the representative atomic structure, a further approximation is typically applied, i.e., an adiabatic decomposition of the remaining degrees of freedom by utilizing the free energy Born-Oppenheimer approximation [58-60] which is justified by the different time scales. The free energy is then written as follows, using again the unprimed index $\alpha$ because different lattices and chemical orderings are now explicitly distinguished:

**Adiabatic free energy decomposition**

$$\begin{aligned} F_\alpha(V, T, \{x_i^\alpha\}) &= E_\alpha(V, \{x_i^\alpha\}) - TS_\alpha^{\mathrm{conf}}(\{x_i^\alpha\}) \\ &\quad + F_\alpha^{\mathrm{el}}(V, T, \{x_i^\alpha\}) + F_\alpha^{\mathrm{mag}}(V, T, \{x_i^\alpha\}) \\ &\quad + F_\alpha^{\mathrm{vib}}(V, T, \{x_i^\alpha\}). \end{aligned} \tag{6}$$

Here, $E_\alpha(V, \{x_i^\alpha\})$ is the total electronic energy of the representative atomic structure of the $\alpha$ phase with all atoms relaxed to their $T = 0$ K equilibrium positions, $S_\alpha^{\mathrm{conf}}(\{x_i^\alpha\})$ the chemical configurational entropy, $F_\alpha^{\mathrm{el}}(V, T, \{x_i^\alpha\})$ is the free energy due to electronic excitations, $F_\alpha^{\mathrm{mag}}(V, T, \{x_i^\alpha\})$ is the magnetic free energy, and $F_\alpha^{\mathrm{vib}}(V, T, \{x_i^\alpha\})$ is the free energy due to atomic vibrations. For a magnetic system, the magnetic energy is often absorbed into $E_\alpha(V, \{x_i^\alpha\})$ (for example of a ferromagnetic or a paramagnetic state; see Section 3.5). Note that adiabatic coupling contributions, for example changes of the electronic density of states due to explicit vibrations affecting the electronic and magnetic free energy [61,62], are implicitly included in Eq. (6).

Computing the full set of contributions to Eq. (6) is still a challenging task even for lower order systems (binaries, ternaries), in fact even for unary materials [63-65]. For HEAs and CCAs, further approximations are at present unavoidable. Different approaches and their application will be discussed in Section 3. Yet, it is useful to state already here that for a disordered multicomponent phase with high concentrations of the elements, as given in HEAs and CCAs, an important role is played by the configurational entropy. This is particularly true when phase decomposition into ordered phases is investigated for which $S_\alpha^{\mathrm{conf}} = 0$. A reasonable approximation for the configurational entropy of a fully disordered system is to assume an ideal mixing behavior (i.e., no short-range order),

**Ideal mixing configurational entropy**

$$S_\alpha^{\mathrm{conf}}(\{x_i^\alpha\}) = -k_B \sum_{i=1}^{N} x_i^\alpha \ln x_i^\alpha. \tag{7}$$

Clearly, the virtue of Eq. (7) is that $S_\alpha^{\mathrm{conf}}$ is immediately available not requiring any involved computation. If a system is partially disordered, for example ordered on one sublattice and disordered on another, the ideal mixing entropy can be applied to the disordered part of the system (see, e.g., Ref. [66]). When a system is close to its order-disorder transition temperature, the entropy cannot be well approximated by Eq. (7), it may become additionally temperature and even volume dependent, and its calculation can be rather involved. In such cases, the representation of the system by a single atomic structure [Eq. (6)] becomes inappropriate as well (at least in DFT accessible supercells). Then one has to resort to a proper sampling of the configurational degree of freedom [Eq. (5)] using the techniques discussed in Section 3.6.

The discussion of mechanical properties in Section 4 can be nicely connected to the above framework. Relatively straightforward is the connection to the stacking fault energy (SFE; Section 4.3) and the multiple phase alloys (Section 4.4) where only phase stability differences (i.e., differences between different $G_\alpha$'s or $F_\alpha$'s) are required. For the case of the SFE, the phases can be (mostly disordered) fcc, hcp, and/or dhcp [ANNNI model discussed in Section 4.3; Eqs. (42) and (43)] or fcc and a stacking fault supercell (explicit SFE). In general, elastic properties (Section 4.1) require an extension to a generalized free energy surface

$$F_\alpha(V, T, \{x_i^\alpha\}) \quad \rightarrow \quad F_\alpha(\boldsymbol{\varepsilon}\cdot\mathbf{A}(T), T, \{x_i^\alpha\}), \tag{8}$$

where the volume $V$ dependence has been replaced by a dependence on the strain tensor $\boldsymbol{\varepsilon}$ applied to the matrix of the lattice vectors $\mathbf{A}$. The cell geometry is assumed to take its thermodynamic equilibrium shape at each temperature, $\mathbf{A} = \mathbf{A}(T)$, where the largest contribution typically stems from the thermal expansion. Application of different strain tensors gives access to different elements of the elastic tensor, i.e., to different elastic constants or the bulk modulus (the latter requiring in fact only a volumetric strain dependence). Local lattice distortions (Section 4.2) relate to atomic positions and demand therefore an atomistic description in addition to the thermodynamic potentials. An atomistic description is naturally provided within an *ab initio* framework and thus extracting local lattice distortions, i.e., the displacements away from ideal lattice positions (fcc, bcc, hcp, …), is readily possible. The relaxation energy due to local distortions is defined as

$$E_\alpha^{\mathrm{relax}} = E_\alpha - E_\alpha^{\mathrm{lat}}, \tag{9}$$

with $E_\alpha$ from Eq. (6) and with $E_\alpha^{\mathrm{lat}}$ the energy of the same atomic structure but with atoms sitting on their ideal lattice positions. Note that, when the vibrational contribution is explicitly included in Eq. (6), atomic displacements can be defined only in a time averaged manner by using mean atomic positions.

In contrast to the statement above regarding the importance of the configurational entropy for phase decomposition, calculations related to mechanical properties such as the elastic properties discussed above and further in Section 4 do not (to a good extent) depend on the configurational entropy. The reason is that the configurational entropy typically cancels out of the corresponding calculations because the considered, e.g., strained phases [cf. Eq. (8)] have the same composition and the same chemical disorder. In this way the configurational entropy can be assumed to have a negligible impact on elastic properties, i.e., $S_\alpha^{\mathrm{conf}}$ does not depend on the strain tensor $\boldsymbol{\varepsilon}$. Note that this does not imply that the impact of chemical ordering is negligible by itself,

the ordered and disordered alloys can — and usually they do — have different mechanical properties. If, as often done, one neglects further the electronic, vibrational, and magnetic free energies, the relevant phase stabilities for mechanical properties and the elastic properties (of ordered, disordered, or partially disordered phases) can be calculated solely from $E_\alpha(V, \{x_i^\alpha\})$ [Eq. (6)] or its generalized version:

$$E_\alpha(V, \{x_i^\alpha\}) \quad \rightarrow \quad E_\alpha(\boldsymbol{\varepsilon}\cdot\mathbf{A}, \{x_i^\alpha\}). \tag{10}$$

## 3. Thermodynamic Phase Stabilities

### 3.1. The Challenge of Determining Phase Decomposition

A critical input to the design of HEAs and CCAs is the knowledge about an alloy's tendency to decompose into different phases. The thermodynamic rules governing phase decomposition are available and have been stated in Section 2, but to determine the possible equality of the chemical potentials [Eq. (2)] the Gibbs energy $G_\alpha(P, T, \{x_i^\alpha\})$ of each relevant phase $\alpha$ needs to be accurately known over the full range of concentrations $\{x_i^\alpha\}$. Typically, this knowledge is not available.

In the early days of the HEA development, empirical rules have been used to determine compositions which can form a single-phase solid solution. These rules are an extension of the Hume-Rothery rules and rely mainly on the elemental atomic radii, crystal structure of solutes, difference in valency as well as electronegativity [2,3]. The idea is to find systems made of elements that are neither too attractive nor too repulsive among each other, both of which would lead to phase separation, either into ordered compounds or into the phases of the pure elements. Given a proper set of elements, the configurational entropy, Eq. (7), is supposed to stabilize a single multicomponent phase. Although such empirical rules had originally proven rather successful in understanding binary solid solutions, their application to multicomponent alloys appears to be not straightforward as experiments, e.g., for the CoCrFeMnNi alloy, revealed [67].

Troparevsky et al. [68] proposed an extension to a semi-empirical rule by introducing *ab initio* information on binary compound phases, which can be expected to play a dominant role in the decomposition of multicomponent alloys. The quantity they used for that purpose is the energy of formation, $E_{\mathrm{AB}}^{\mathrm{form}}$, of a binary phase referenced with respect to the most stable unary phases with energies, $E_{\mathrm{A}}$ and $E_{\mathrm{B}}$,

$$E_{\mathrm{AB}}^{\mathrm{form}} = E_{\mathrm{AB}} - (x_{\mathrm{A}}E_{\mathrm{A}} + x_{\mathrm{B}}E_{\mathrm{B}}), \tag{11}$$

where $E_{\mathrm{AB}}$ is the molar energy of the considered binary compound with $x_{\mathrm{A}}$ and $x_{\mathrm{B}}$ mole fractions of the elements A and B. For each binary, Troparevsky et al. [68] investigated various compounds using information from existing DFT libraries and selected the compound with the lowest formation energy as exemplified in Fig. 2. These formation energies are assumed to compete with the $-TS_\alpha^{\mathrm{conf}}$ term of the multicomponent alloy with the ideal mixing entropy $S_\alpha^{\mathrm{conf}}$ according to Eq. (7) and with $T$ set to the annealing temperature of the alloy. The rule states in particular that a single phase HEA is obtained when none of the formation energies $E_{\mathrm{AB}}^{\mathrm{form}}$ of the sub-binaries is lower than $-TS_\alpha^{\mathrm{conf}}$. Since this condition only covers one of the above statements, i.e., that the elements should not be too attractive, it needs to be supplemented: None of the formation energies should be too high to prevent decomposition into the pure element phases. A critical value of +37 meV/atom was empirically chosen by adjusting it to reproduce experimentally observed single phase HEAs. The rule can for example rationalize the formation of the CoCrFeMnNi HEA. Taking 1000 K for the annealing temperature $-TS_\alpha^{\mathrm{conf}}$ amounts to −139 meV/atom. Fig. 2 reveals that none of the binary formation energies is below $-TS_\alpha^{\mathrm{conf}}$ (MnNi is lowest with −115 meV/atom) and none is too high (FeMn is highest with +9 meV/atom).

The virtue of this approach is its simplicity and efficiency. Note that no explicit *ab initio* calculation for the HEA is required. This simplicity implies however shortcomings. The rule does not distinguish between different lattices (fcc, bcc, hcp) for the HEA. The electronic, vibrational, and magnetic free energy contributions in Eq. (6) are neglected. Further, the rule does not explicitly consider the formation energy of the potential HEA,

$$E_\alpha^{\mathrm{form}} = E_\alpha - \left(\sum_i^N x_i^\alpha E_i\right), \tag{12}$$

where $E_\alpha$ is the total energy of the multicomponent system [Eq. (6)] and the $E_i$ are the energies of the most stable unary phases[1], since the binary formation energies are only compared to the $-TS_\alpha^{\mathrm{conf}}$ term. The formation energy can take significant values as calculations clarify. For example, $E_\alpha^{\mathrm{form}}$ of bcc NbTiV and MoNbTaVW are found to be 52 and −139 meV, respectively [69], exemplifying the possible range of values for the formation energy (cf. Table 2). It should not, however, be thought that the knowledge of the formation energies alone would be in general sufficient for a prediction of single-phase alloys. In another work, Troparevsky et al. [17] showed that single-phase alloys can have similar formation energies as closely-related multi-phase formers. The chief problem is that empirical or semi-empirical rules require some simplifying assumption about phase decomposition. To avoid such an assumption, the knowledge of $G_\alpha(P, T, \{x_i^\alpha\})$ for the different lattices and various compositions is indispensable, and a more advanced treatment is unavoidable.

*Ab initio* calculations performed directly for the multicomponent alloy provide, in principle, the possibility to calculate the required information on phase decomposition. We will discuss the required computational methodology in Sections 3.2 to 3.6, but it is useful to anticipate a result related to phase decomposition to highlight the potential and also a difficulty. Already five years ago, Tian et al. [70] studied the phase stability of $\mathrm{Al}_y(\mathrm{CoCrFeNi})_{1-y}$ alloys using *ab initio* calculations. Experiments suggest that depending on the Al-content, these alloys reveal an fcc ($y \leq 0.110$), a double fcc/bcc ($0.110 < y < 0.184$) or a bcc region ($y \geq 0.184$) [71]. To investigate the relative phase stability, Tian et al. [70] employed EMTO-CPA calculations (Section 3.2) in combination with the common tangent construction. The Gibbs energy of formation including the magnetic contribution (Section 3.3) was computed in the range of $y \in [0.0, 0.5]$, i.e., $G_\alpha^{\mathrm{form}}(y) = G_\alpha(y) - (1-2y)G_{\mathrm{fcc}}(0) - 2yG_{\mathrm{fcc}}(0.5)$ where the energies are given per atom and $\alpha$ denotes the fcc or bcc phase, respectively. In Fig. 3, the common tangent constructions are shown for different temperatures. At room temperature, a double phase fcc/bcc region is predicted for $0.13 < y < 0.24$ and single phase regions for $y \leq 0.13$ (fcc) and $y \geq 0.24$ (bcc), in good qualitative agreement with experiment. In a subsequent study employing a similar methodology, Sun et al. [72] studied the phase stability of the same alloy system and found that adding Mn widens the double phase region by shrinking the fcc stability range and delaying the occurrence of the bcc phase upon Al alloying. They could also confirm that both structures, fcc and bcc, remain elastically stable (Section 4.1) within the double phase region and thus decomposition into fcc and bcc is theoretically clearly supported.

While being informative, studies as performed by Tian et al. [70] and Sun et al. [72] reveal a general difficulty when computing phase decomposition directly from *ab initio*. To render such studies computationally feasible the high dimensional compositional space must be reduced to a lower dimension, typically a pseudobinary alloy as done in the above studies. Sometimes, the reduction can be motivated by experimental information, but even then it remains unclear whether different results would be obtained if an extended part of the compositional space was investigated. A promising route to tackle this challenge in the future may be a combination of selective *ab initio* calculations in designated parts of the compositional space with CALPHAD type

[1] The definition of the formation energy requires some caution as discussed in the last paragraph of this subsection (Section 3.1).

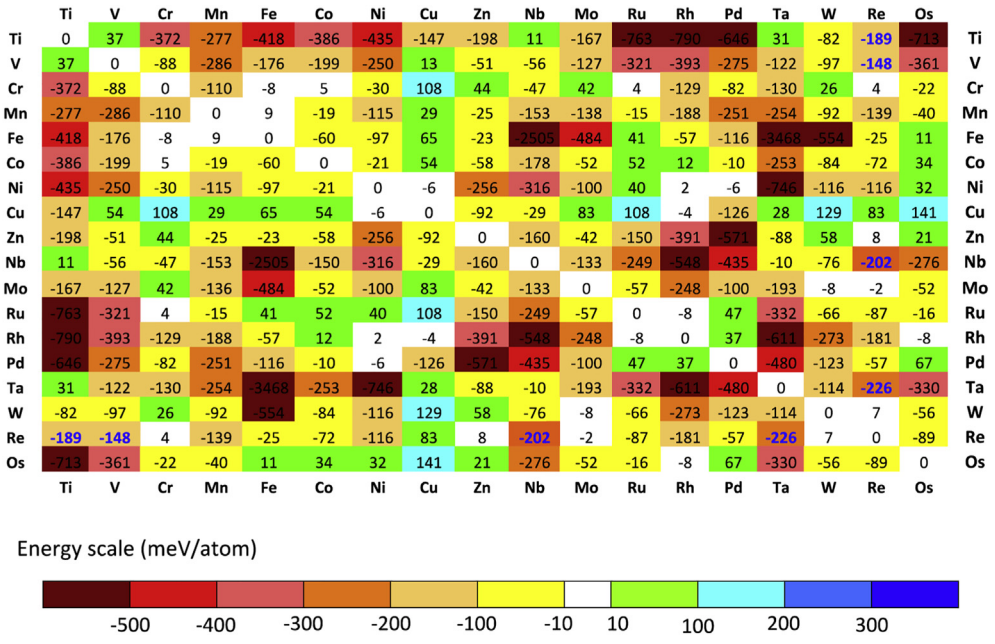


**Fig. 2.** DFT computed energies of formation for the energetically lowest structures of a wide range of binaries relative to their phase separation into pure elements. If the numbers are in bold blue, the energies were evaluated with respect to the respective solid solution. (For interpretation of the references to color in this figure legend, the reader is referred to the web version of this article.)
Source: Taken from Ref. [68].

**Table 2**
Formation energies, $E_\alpha^{\text{form}}$, of HEAs/CCAs computed employing the supercell method and VASP [69]. The corresponding relaxation energy, $E_\alpha^{\text{relax}}$, and the configurational entropy contribution to the free energy, $-TS_\alpha^{\text{conf}}$, at 1000 K are also displayed. All contributions are given in meV/atom.

| Alloys | Crystal structure $\alpha$ | $E_\alpha^{\text{relax}}$ | $E_\alpha^{\text{form}}$ | $-TS_\alpha^{\text{conf}}$ |
|---|---|---|---|---|
| HfNbZr | bcc | −80 | 25 | −95 |
| HfNbTiZr | bcc | −65 | 33 | −119 |
| HfNbTaTiZr | bcc | −43 | 28 | −139 |
| MoNbTaVW | bcc | −29 | −139 | −139 |
| NbTiV | bcc | −22 | 52 | −95 |
| AlNbTiV | bcc | −43 | −94 | −119 |
| CoFeNi | fcc | −13 | 4 | −95 |
| CoCrFeNi | fcc | −19 | −14 | −119 |
| CoCrFeMnNi | fcc | −4 | 7 | −139 |

parameterizations along the composition and temperature axes. Such combined studies have been already put forward for lower order systems (e.g., binaries in Refs. [73,74]). In any case, whether pursuing a combined *ab initio*-CALPHAD approach or brute force *ab initio* calculations, an accurate determination of $G_\alpha(P, T, \{x_i^\alpha\})$ is a critical premise. The following subsections of Section 3 will detail the required methodology and the respective studies performed so far. A special role is played by the methods introduced in Section 3.6 that treat phase transitions and decomposition on the same lattice driven by a competition of order *versus* disorder. As will be discussed, for such special cases it may be possible to find the product phases of a decomposition without prior knowledge of the exact composition ranges.

Before moving on, it seems appropriate to comment on potential inconsistencies in the definition and usage of the term *formation* energy and the related term *mixing* energy. In Eq. (12), we have used the most stable unary phases as the reference, i.e., phases that do not necessarily have the same crystal lattice as the investigated multicomponent alloy. This definition makes a direct comparison with the binary formation energies in Eq. (11) possible and also with formation energies as typically stored in DFT databases. The definition Eq. (12) is often used in the HEA/CCA literature, but sometimes the resulting formation energy is denoted as *mixing energy*. We prefer the term formation energy, because in the computation of phase diagrams (e.g., in the CALPHAD approach) the mixing energy is more commonly defined with isostructural reference energies, i.e., the $E_i$'s in Eq. (12) correspond then to the unary end-member phases on the *same* lattice as the considered multicomponent phase [3,55]. A feature of the isostructural mixing energy is that it vanishes naturally for the end-members, i.e., when only a single element is left in the alloy and thus no mixing is possible. Besides using unary phases as a reference, one may also define a formation energy with respect to the energies of the reactant phases (may they be unary, binary, or ternary) as encountered in the experimental synthesis procedure of the actual multicomponent alloy. (In such cases, the term enthalpy of formation is typically used.) Any of these definitions is equally valid and one may in fact choose an arbitrary reference, cf. Fig. 3 where $y = 0$ and $y = 0.5$ serve as the reference points. Caution is only required when comparing differently defined formation energies, and in general it is advisable to state clearly which reference is used in the definition.

### 3.2. Ab Initio Modeling of Chemical Disorder

The total energy $E_\alpha(V, \{x_i^\alpha\})$ is a critical contribution to the free energy of a phase $\alpha$ in Eq. (6) when determining phase stabilities, and in its generalized form $E_\alpha(\boldsymbol{\varepsilon}\cdot\mathbf{A}, \{x_i^\alpha\})$ dominates elastic properties (Section 4.1). For an *ordered* compound, this energy can be efficiently computed within an *ab initio* DFT framework (e.g., Fig. 2), in particular by employing periodic boundary conditions. The primitive cell is sufficient for handling an ordered compound and thus corresponding calculations are reasonably small with respect to the number of atoms. The configurational entropy vanishes and $E_\alpha$ becomes the dominant term. The situation is much more complicated if chemical disorder becomes thermodynamically favorable with increasing temperature due to the $-TS_\alpha^{\text{conf}}$ term in Eq. (6). If the configurational entropy contribution becomes strong enough to compete with the ordering tendency of the alloy, an isostructural second order transition to a disordered state occurs. At temperatures close to the critical order-disorder transition temperature the system exhibits complex geometrical features — arising from the transition from perfect long-range order to local short-range order — that cannot be easily captured by DFT accessible supercells. For multicomponent alloys, the situation is typically further complicated by the occurrence of multiple order-disorder transition temperatures as sketched in Fig. 4.

The DFT based simulation of multicomponent alloys close to the order-disorder transition temperature is thus a highly non-trivial task requiring a proper sampling over many atomic configurations [Eq. (5)]

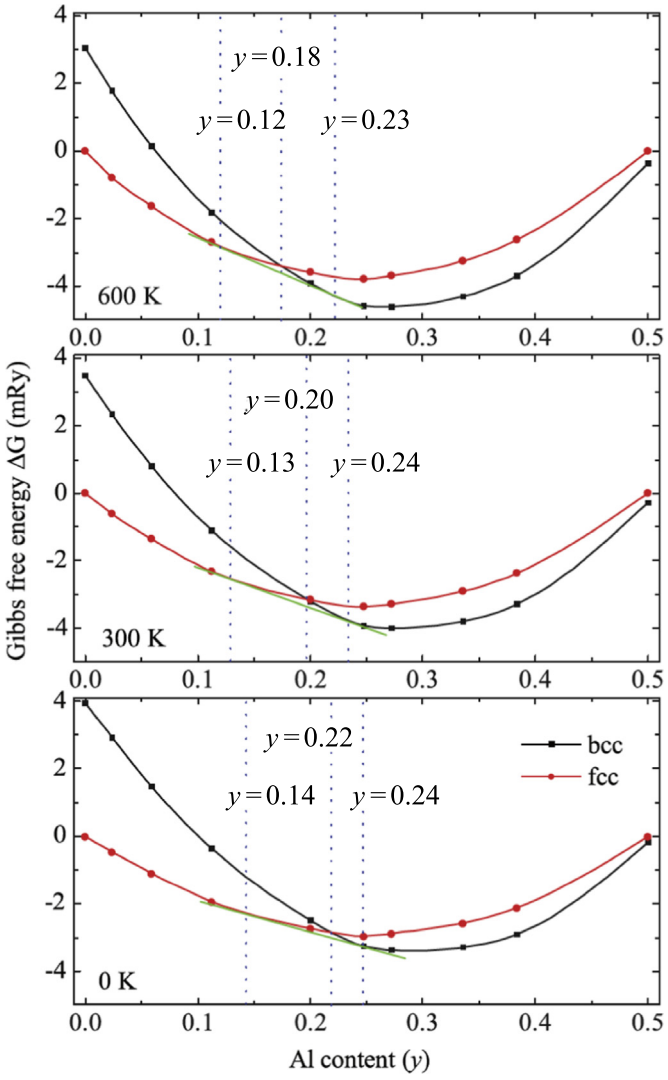


**Fig. 3.** Gibbs energies of bcc and fcc $Al_y(CoCrFeNi)_{1-y}$ as a function of the Al content from EMTO-CPA calculations at temperatures 600 K, 300 K, 0 K (from top to bottom).
Source: Adapted from Ref. [70].

using elaborate statistical approaches (Section 3.6). The complexity of such simulations is most likely the reason why the majority of DFT based HEA and CCA investigations focused on modeling a perfectly disordered state, which is much more amenable to direct DFT calculations. Nevertheless, additional concepts are required and those will be introduced in the remainder of this subsection (Section 3.2). The assumption of perfect disorder also makes the calculation of the finite temperature effects due to electrons, magnetism, and vibrations much more amenable as introduced in Sections 3.3 to 3.5.

A perfectly disordered state [cf. Fig. 4(c)], i.e., a solid solution, is a reasonable approximation when the system is sufficiently high above its highest order-disorder transition temperature. To calculate the energy $E_\alpha$ of such a fully disordered multicomponent solid solution on the lattice $\alpha$ a proper average over the chemical disorder is required, which can be achieved using the methods introduced in the following. The corresponding configurational entropy is given directly by Eq. (7). In fact, the same methods can be also used for systems that are partially disordered, for example on one or more sublattices [cf. Fig. 4(b)], but are sufficiently away from any order-disorder transition temperature. One has only to remember that the disorder is confined to a certain sublattice and that the configurational entropy needs to be properly adjusted (see, e.g., Ref. [66]). The available state-of-the-art methods within DFT for simulating disorder can be roughly categorized into two classes, those based on supercell models, usually in combination with the concept of special quasirandom structures (SQS) [75], and those based on the coherent-potential approximation (CPA) (see, e.g., Refs. [76,77]). Both classes of methods have their advantages and disadvantages, and it depends on the specific type of application which one is better suited.

In the supercell-based methods, a disordered chemical configuration is simulated based on a large yet finite supercell employing periodic boundary conditions as sketched in Fig. 5(a). In practice, supercell calculations for HEAs and CCAs are typically performed employing a plane-wave basis and the projected augmented wave (PAW) method [78] as implemented, e.g., in the VASP simulation package [79,80]. In principle, an atomic configuration derived from a uniform random distribution could be used for simulating chemical disorder within a supercell. However, corresponding supercells would require several hundreds of atoms to represent perfect chemical randomness well enough, due to the long-range order imposed by the periodic boundary conditions. A better approach is to use the SQS concept [75]. In this approach, the different species in the supercell are distributed in such a way as to minimize the atomic pair correlation functions. A good representation of chemical randomness can be often achieved with supercells of several tens of atoms already. The larger the supercell, the more shells and also higher order correlation functions (e.g., triplets) can be included in the minimization thus further increasing the quality of the chemical randomness.

A very important advantage of the supercell methods is the straightforward inclusion and analysis of the impact of local lattice

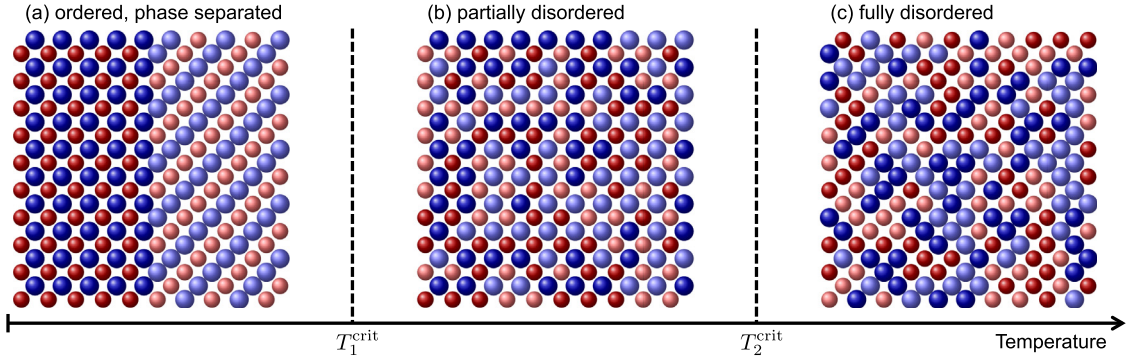


**Fig. 4.** Schematics for the transition of a four component alloy from (a) a phase-separated state consisting of two ordered binaries to (b) a partially disordered state at the critical transition temperature $T_1^{crit}$ and further to (c) a fully disordered state at a second critical transition temperature $T_2^{crit}$. Note that in (b) the blue atoms are confined to one sublattice but light and dark blue are disordered on this sublattice, and that red atoms are confined to the other sublattice again with light and dark red being disordered. (For interpretation of the references to color in this figure legend, the reader is referred to the web version of this article.)

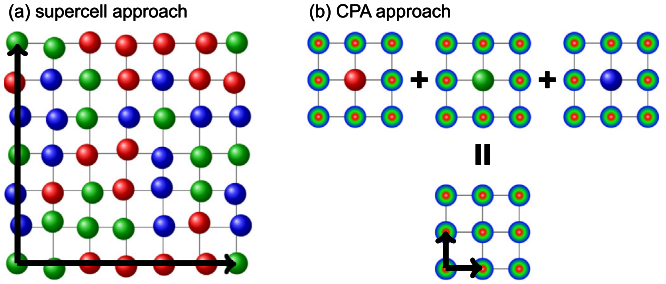


**Fig. 5.** Schematics for (a) the supercell and (b) CPA approach.

distortions. Lattice vibrations can be also accurately modeled based on, e.g., the finite-displacement method or molecular dynamics (MD) simulations (see Section 3.3). A disadvantage is the relatively high computational costs, even when combined with the SQS concept, as compared to CPA calculations which are usually orders of magnitude less expensive. Further, although it is in principle possible to mimic magnetically disordered configurations with the supercell approach, it is often difficult to stabilize such magnetic configurations during the electronic minimization. In practice, supercell calculations initialized with a well-defined magnetic configuration can converge into energetically close-by but different magnetic configurations. This makes, in particular, the simulation of paramagnetic HEAs and CCAs with the supercell approach challenging from a technical standpoint.

CPA based methods rely on a mean field approach to chemical disorder as sketched in Fig. 5(b). The CPA is typically combined with muffin-tin based Kohn-Sham methods [81] and implemented in, e.g., exact muffin-tin orbitals (EMTO) [77,81] or Korringa-Kohn-Rostoker (KKR) methods [82,83]. In CPA, each of the elements in the alloy is embedded into an effective medium that is determined self-consistently from the mutual effect of all elements together. Due to this mean field approach, CPA-based methods can mimic perfect chemical disorder within a single primitive cell and thus they have very low computational requirements. Additionally, CPA methods are not limited to specific compositions. These advantages enable a computationally very efficient exploration of large compositional spaces. Within CPA, it is also comparably straightforward to simulate magnetically disordered configurations within the disordered-local-moment (DLM) approach. The DLM approach is nowadays routinely employed to investigate the paramagnetic (PM) state of magnetic materials. Further, CPA-based techniques such as the generalized perturbation method enable an efficient extraction of chemical interaction parameters which can be combined with mean field (e.g., concentration wave analysis) or Monte Carlo (MC) methods to study chemical SRO (see Section 3.6). However, the computational amenities come along with limitations. The probably most severe one is the inability to include local lattice distortions within the standard CPA. Another related limitation of CPA is the inability of computing interatomic forces hindering an accurate modeling of vibrations (e.g., via the direct force constant method or MD simulations). Approximate models need therefore to be employed to include vibrational contributions, e.g., the Debye-Grüneisen model (Section 3.3).

Many studies of $E_\alpha(\{x_i^\alpha\})$ for disordered multicomponent systems have been performed with both supercell and CPA methods, mostly focusing on equiatomic compositions, i.e., $x_i^\alpha = x_j^\alpha$ for each $i$ and $j$. A fairly complete compilation is given in the Appendix (see "Phase stability" in Table 9). Derived elastic constants are additionally discussed in Section 4.1. Here, we focus on the study of Song et al. [69] based on the supercell approach, which allows us to gain an idea about possible values for the formation energy of multicomponent solid solutions and also about the size of the relaxation energy.

The formation energy, $E_\alpha^{\text{form}}$, can be obtained from $E_\alpha$ and the ground states of the unary phases according to Eq. (12). Using $E_\alpha^{\text{form}}$ in addition to the binary formation energies $E_{\text{AB}}^{\text{form}}$ (Fig. 2) it is, for example, possible to extend the semi-empirical rule of Troparevsky et al. [68] discussed in Section 3.1. The alloy's tendency to form a solid solution or decompose into binary compounds can be then obtained by comparing the binary formation energies $E_{\text{AB}}^{\text{form}}$ to the $(E_\alpha^{\text{form}} - TS_\alpha^{\text{conf}})$ term of the respective multicomponent alloy, instead of comparing them just to $-TS_\alpha^{\text{conf}}$. Positive $E_\alpha^{\text{form}}$'s work against the configurational entropy requiring thus higher temperatures to form a multicomponent solid solution, while negative $E_\alpha^{\text{form}}$'s favor solid solution formation even at lower temperatures. Formation energies for the two important HEA classes, bcc refractory and fcc 3*d* HEAs, from the work of Song et al. [69] are shown in Table 2. The data clarify that formation energies can be sometimes of a similar magnitude as the $-\text{TS}_\alpha^{\text{conf}}$ term and thus cannot be *a priori* neglected.

The formation energy can be formally separated into a contribution evaluated on the ideal lattice, $E_\alpha^{\text{lat}}$, and a contribution arising from local lattice relaxations, $E_\alpha^{\text{relax}}$ [cf. Eq. (9)]. Results for the relaxation energies of the systems investigated in the work of Song et al. [69] are reproduced in the $E_\alpha^{\text{relax}}$ column of Table 2. It can be seen that the impact of local lattice relaxations can be rather significant. For instance, the formation energy of bcc HfNbZr is reduced by −80 meV/atom (from 105 down to 25 meV/atom) when relaxations are included in the calculations. It is thus evident that, in general, the impact of local relaxations and respective energy contributions cannot be disregarded and can contribute to phase stability considerations.

This point needs to be carefully considered when using CPA for the calculation of formation energies. A possible approach to exploit the immense efficiency of CPA, yet to secure oneself for accurate formation energies is a coupled approach. CPA can be first used to efficiently scan wide ranges of composition space to create a reasonably approximate mapping of the desired quantity. Explicit and computationally significantly more expensive supercell computations can be then used at designated compositions to evaluate the impact of local lattice distortions.

We also note here an *ab initio* informed work on formation energies of multicomponent solid solutions that may be relevant for some specific applications. Leong et al. [84] extended the rigid-band approximation (RBA) to HEAs, in particular magnetic HEAs. The rigid band model assumes that the overall shape of the electronic density of states (DOS) is unaffected by a solvent. One can thus compute the DOS of a certain base alloy (e.g., CoCrFeNi) once with *ab initio* using for example an SQS and then use this DOS to scan efficiently but approximately for formation energies of this alloy plus additional solvents (e.g., Al, Pd, Ti, V). In this way, at least, the relaxations for the base alloy are accounted for. For the investigated elements, Leong et al. [84] found qualitative agreement with experiments.

### 3.3. Finite-temperature Excitations

So far in this section (Section 3), we have discussed the formation and stability of multicomponent phases concentrating mainly on the total electronic energy $E_\alpha(V, \{x_i^\alpha\})$ (from which the formation energy can be derived) and the configurational entropy term $-TS_\alpha^{\text{conf}}$, i.e., the first two terms of the free energy formula, Eq. (6). We have assumed a perfect random solid solution so that the configurational entropy can be approximated by Eq. (7). Originally, the $-TS_\alpha^{\text{conf}}$ term was considered as the main temperature dependent contribution to the stabilization of a solid solution over potential phase decomposition [5,6] (see also Section 3.1). More recent experiments [67] questioned the dominant role of configurational entropy and indicated the potential importance of other entropy contributions related to finite-temperature excitations of electronic, magnetic, and vibrational degrees-of-freedom. A proper consideration of finite-temperature excitations is moreover important for the alloys' thermodynamic, magnetic and mechanical properties at elevated temperatures. The challenge is thus to accurately compute the free energy contributions entering Eq. (6).

As mentioned in Section 2, the standard approach is to decompose the free energy, Eq. (6), into separate contributions due to electronic

$F_\alpha^{el}$, magnetic $F_\alpha^{mag}$, and vibrational $F_\alpha^{vib}$ excitations. Similarly as for the total energy $E_\alpha$, the calculation of each of these free energy contributions for a disordered multicomponent phase requires to properly mimic a random alloy. Available approaches will be discussed in the following. Intrinsic point defects such as vacancies also contribute to the total Gibbs energy, but this contribution is in general small, with a possible exception close to the melting point. A few recent studies in this respect will be discussed at the end of this subsection (Section 3.3).

The most easily accessible finite-temperature excitations are due to the electronic degrees-of-freedom. The basic reason for this is that there is an exact theory which extends the original Hohenberg-Kohn DFT formalism [40] to finite electronic temperatures [85]. Practically, this means that the electronic free energy $F_\alpha^{el}(V,T)$ can be computed from a usual self-consistent Kohn-Sham calculation [41] (applied either to a supercell or CPA calculation to mimic chemical disorder) by using the Fermi-Dirac distribution to populate the electronic energy levels according to the temperature of interest. In fact, there is a very good approximation available that simplifies the calculation further. In this approximation, the electronic density of states (DOS) $D_\alpha(\varepsilon)$ of a phase $\alpha$, with $\varepsilon$ denoting an energy dependence, is used to obtain the full temperature dependence of $F_\alpha^{el}(V,T)$.[2] The electronic DOS is a direct output of any DFT calculation and thus $F_\alpha^{el}(V,T)$ is readily accessible, specifically using (see, e.g., Ref. [62]):

**Fixed DOS approximation**

$$F_\alpha^{el}(V,T) = U_\alpha^{el}(V,T) - TS_\alpha^{el}(V,T), \quad (13)$$

$$U_\alpha^{el}(V,T) = \int_{-\infty}^{\infty} D_\alpha(\varepsilon) f(T) \varepsilon d\varepsilon - \int_{-\infty}^{\varepsilon_F} D_\alpha(\varepsilon)\varepsilon d\varepsilon, \quad (14)$$

$$S_\alpha^{el}(V,T) = k_B \int_{-\infty}^{\infty} D_\alpha(\varepsilon) s(\varepsilon,T) d\varepsilon, \quad (15)$$

$$s(\varepsilon,T) = -[f\ln(f) + (1-f)\ln(1-f)]. \quad (16)$$

Here, $f = f(\varepsilon,T)$ is the Fermi-Dirac function and $\varepsilon_F$ denotes the Fermi energy at 0 K. The two terms in $s(\varepsilon,T)$ above can be interpreted as a temperature-weighted, configurational entropy contribution due to the creation of electrons and holes. Note that the above formulation assumes a temperature-independent $D_\alpha(\varepsilon)$, which gives rise to the name *fixed DOS approximation*. In principle electronic excitations could impact the electronic DOS at elevated temperatures, but it was shown for a wide range of unaries [62] that this impact on $D_\alpha(\varepsilon)$ is minor and can thus be neglected. In contrast, the impact of the volume on $D_\alpha(\varepsilon)$ is in general important and needs to be considered in conjunction with the thermal expansion due to lattice vibrations. In practice, Eq. (13) is usually evaluated at several volumes and parametrized [86] to facilitate the evaluation of the total free energy, Eq. (6), and thus the inclusion of the thermal expansion. Lattice vibrations therefore have an indirect impact on $F_\alpha^{el}(T)$ via the alloys' thermal expansion. Recent *ab initio* molecular dynamics simulations revealed that there can be also a strong *explicit* impact of lattice vibrations on $D_\alpha(\varepsilon)$ and thus on $F_\alpha^{el}(T)$ [61,62]. This explicit coupling of lattice vibrations and electronic free energies for HEAs and CCAs has, however, not yet been thoroughly explored by *ab initio* simulations. Eventually, the inclusion of magnetic excitations and magnetic disorder may also impact $D_\alpha(\varepsilon)$ and thus the corresponding electronic free energy. This could be studied, e.g., by computing a spin dependent electronic DOS in different magnetic states.

Computation of the magnetic free energy,

$$F_\alpha^{mag}(V,T) = U_\alpha^{mag}(V,T) - TS_\alpha^{mag}(V,T), \quad (17)$$

is from a conceptional standpoint very challenging since no unified approach exists to bridge in a general manner from ground state spin-polarized DFT calculations to finite magnetic temperatures for alloys with different magnetic characteristics, i.e., ranging from an itinerant-type of band ferromagnetism to localized magnetic moment systems (see, e.g., Ref. [87]). In practice, different approaches are chosen depending on the considered material system and involved elements. For example, for elements which feature strongly itinerant magnetic characteristics such as, e.g., pure nickel, it is important to take longitudinal spin fluctuations into account (see, e.g., Ref. [88]). Corresponding techniques are, however, not yet advanced enough to be generally applicable to HEAs and CCAs. Instead, HEAs and CCAs are so far mainly simulated by mapping the magnetic energetics onto a localized magnetic moment picture. Even though the input parameters for such models can be computed from *ab initio*, the models are usually not straightforward to solve and require sometimes even the application of advanced quantum Monte Carlo techniques (see, e.g., Refs. [64,89-91]). For an overview on recent progress in describing magnetic contributions from *ab initio* for pure elements and selected ordered binaries, we refer to Refs. [64,92].

For HEAs and CCAs, the *ab initio* calculation of the magnetic free energy is, in the majority of studies, subject to further approximations. Within a localized magnetic moment picture one can consider the high temperature limit of fully disordered magnetic moments, i.e., temperatures well beyond the Curie temperature $T_C$ (or Néel temperature $T_N$ for antiferromagnetic systems), which also highlights the importance of determining $T_C$ (see Section 3.5 below). In the considered high-temperature limit, the internal magnetic energy of the system is assumed to be temperature independent, $U_\alpha^{mag}(V, T \gg T_C) \approx U_\alpha^{DLM}(V)$. The contribution $U_\alpha^{DLM}(V)$ is usually absorbed into the total energy $E_\alpha(V)$ resulting in a simplified magnetic free energy expression (see, e.g., Ref. [87]):

**High temperature approximation for magnetism**

$$F_\alpha^{mag}(V, T \gg T_C) \approx -TS_\alpha^{mag}(V, T \gg T_C) \equiv -TS_\alpha^{mag}(V), \quad (18)$$

$$S_\alpha^{mag}(V) = k_B \sum_i x_i^\alpha \ln(|m_i^\alpha(V)| + 1). \quad (19)$$

The magnetic entropy $S_\alpha^{mag}$ is given here in a mean field approximation [87,93,94] and $m_i^\alpha(V)$ is the magnetic moment of the $i$'th element with concentration $x_i^\alpha$ in the phase $\alpha$. Note that in general, the magnetic moments depend on volume giving rise to a volume dependent set of formulas, Eqs. (17)–(19).

The expression for the magnetic entropy $S_\alpha^{mag}(V)$ above can be interpreted as a configurational entropy of spins [91]. This can be intuited by considering the high-temperature limit of a quantum mechanical spin model with spin quantum number $S$ which can take half-integer values $S = 1/2, 3/2, \ldots$. The number of possible spin states is given by $2S + 1$ giving rise to a maximum entropy of $\ln(2S + 1)$. Relating the spin $S$ with a magnetic moment, $m$, via $m = g\mu_B S$ with the Bohr magneton $\mu_B$ and the Landé factor $g \approx 2$ one directly ends up with Eq. (19) above. Despite the general limits of mapping itinerant magnetic systems with non-integer local magnetic moments onto localized magnetic spin Hamiltonians, this interpretation reveals the close analogy between magnetic and chemical configurational entropy.

As standard *ground-state* spin-polarized DFT calculations provide direct access to the local magnetic moments $m_i^\alpha$ of any of the alloy components (defined within a sphere around each atom; see, e.g., Ref. [95]), the usage of Eqs. (18) and (19) is straightforward and therefore a common approach to take magnetic free energy contributions into account. In this way, the task of introducing chemical disorder into the magnetic contribution is reduced to modeling the chemical disorder in the ground-state energy $E_\alpha(V, \{x_i^\alpha\})$ as already

[2] Note that it is crucial to take the full energy dependence of the DOS into account. The Sommerfeld approximation, which employs only the DOS at the Fermi level and thereby corresponds to a low-temperature expansion of Eq. (14), reveals severe errors at high temperatures [62].

discussed in Section 3.2. In fact, the high-temperature, magnetically disordered state is modeled in an analogous fashion as for the chemical disorder. A magnetic element A can be represented in terms of two magnetically distinct, spin up and spin down atoms, i.e., $A_\uparrow$ and $A_\downarrow$. Thus, in a very similar way as for a chemically disordered A-B alloy, the paramagnetic state with randomized up- and down-spins can be modeled as an *effective* $A_\uparrow$-$A_\downarrow$ alloy. This is the so called disordered local moment (DLM) approach [96,97] which is nowadays commonly employed in CPA simulations to introduce magnetic disorder. Alternatively, the supercell approach (for example in conjunction with the SQS concept) can be utilized by employing a magnetic supercell in which the magnetic correlation functions of $A_\uparrow$ and $A_\downarrow$ spins are minimized. In order to establish whether a fully magnetic disordered scenario is appropriate, the knowledge of the magnetic ordering temperature (e.g., $T_C$) is crucial. Related *ab initio* works and techniques to compute $T_C$ for HEAs and CCAs will be therefore discussed in Section 3.5.

The last term in Eq. (6) corresponds to the free energy of atomic vibrations which, in absolute numbers, is typically the largest contribution and known to play an important role in forming solid solutions (see, e.g., Refs. [98,99]). In principle, atomic vibrations break the periodic symmetry of the crystal and thus require explicit supercell calculations with large enough supercells and also many separate calculations, for example different displacements in the direct force constant method. Corresponding studies for multicomponent alloys are therefore very rare. We will treat them separately in Section 3.4. Here, we focus first on a very efficient approximate treatment of the vibrational free energy as enabled by the Debye-Grüneisen approach [100] that requires *only* the total energy surface $E_\alpha(V, \{x_i^\alpha\})$ as input. Due to the immense computational efficiency and the reasonable accuracy, the Debye-Grüneisen approach has become the standard approach for computing the vibrational free energy of disordered alloys from *ab initio*, in particular for HEAs [66,101-103]. The task of introducing chemical disorder into the vibrational contribution is thus reduced to modeling the chemical disorder in $E_\alpha(V, \{x_i^\alpha\})$ as discussed in Section 3.2. Note that the Debye-Grüneisen approach makes it in particular possible to compute the vibrational free energy within the EMTO-CPA methodology (albeit without relaxations).

Within the Debye-Grüneisen model, the vibrational free energy is given as:

**Debye-Grüneisen approximation**

$$F_\alpha^{\mathrm{vib}}(V, T) = U_\alpha^{\mathrm{vib}}(V, T) - TS_\alpha^{\mathrm{vib}}(V, T), \tag{20}$$

$$U_\alpha^{\mathrm{vib}}(V, T) = \frac{9}{8}k_B\Theta_{\mathrm{D}}^\alpha(V) + 3k_BTD(y_\alpha), \tag{21}$$

$$S_\alpha^{\mathrm{vib}}(V, T) = 3k_B\left(\frac{4}{3}D(y_\alpha) - \ln(1 - \exp(-y_\alpha))\right). \tag{22}$$

The Debye function is denoted as $D(y)$ and $y = \Theta_{\mathrm{D}}(V)/T$ with the Debye temperature $\Theta_{\mathrm{D}}(V)$. In practical applications, the ground state $\Theta_{\mathrm{D}}(V_0) = \Theta_{\mathrm{D}}$ is usually obtained based on the Moruzzi approach [100], i.e.,

$$\Theta_{\mathrm{D}} = C\sqrt{\frac{r_0B_0}{M}}, \tag{23}$$

where $C$ is an empirical constant, $M$ the (averaged) atomic mass, $r_0$ the equilibrium Wigner-Seitz radius and $B_0$ the bulk modulus at zero temperature. Note that $M$, $r_0$, and $B_0$ in general depend on the composition $\{x_i^\alpha\}$ and considered phase $\alpha$. The volume dependence is included in the Debye-Grüneisen approach [100] as

$$\Theta_{\mathrm{D}}(V) = \Theta_{\mathrm{D}}(V_0)(V_0/V)^\gamma, \tag{24}$$

where the Grüneisen parameter $\gamma$ is given by

$$\gamma = -g + \frac{1}{2}(1 + B_0'), \tag{25}$$

where $B_0'$ is the bulk modulus derivative with respect to pressure. The parameter $g$ is dependent on the choice of the approximation and can take values of $g = 2/3$ proposed for high temperatures by Slater et al. [104] or $g = 1$ proposed for low temperatures by Dugdale and MacDonald [105].

Based on the above introduced methodologies for $F_\alpha^{\mathrm{el}}$, $F_\alpha^{\mathrm{mag}}$, and $F_\alpha^{\mathrm{vib}}$, Ma et al. [101] employed EMTO-CPA calculations to investigate the crystal phase stabilities and entropy contributions for the equiatomic CoCrFeMnNi HEA, specifically for $\alpha$ = bcc, fcc, and hcp (all disordered). As the composition is constant for all considered $\alpha$, the ideal mixing configurational entropy is constant as well, i.e., $S_\alpha^{\mathrm{conf}} = k_B\ln(5) \approx 1.6\,k_B$. The results for the entropy contributions arising from electronic, magnetic, and vibrational excitations according to Eqs. (13)–(25) are shown in Fig. 6. It becomes clear that the vibrational contribution can be in fact four times larger than the configurational contribution. The absolute values of the vibrational entropies should be however not directly employed for phase stability considerations, because any phase for any alloy system (also unaries and binaries) will acquire a similarly appreciable vibrational entropy. The observed spread (up to about $1\,k_B$) of the vibrational entropies among the different phases is a more representative quantity for phase stabilities. Magnetic as well as electronic contributions also show an appreciable spread (up to about $0.8\,k_B$). These findings indicate that entropic contributions beyond the configurational one can become significant, in particular when considering crystal phase stabilities. It was moreover shown in Ref. [101] that at $T = 0$ K, the hcp phase is thermodynamically the most stable phase of the CoCrFeMnNi alloy. This finding was later confirmed by explicit supercell calculations in Ref. [106]. The fcc phase, which is also observed experimentally at high temperatures [107], becomes stabilized (as compared to hcp at fixed equiatomic composition) mainly due to lattice vibrations [101].

The importance of entropy contributions beyond the configurational one was likewise pointed out in the study of Li et al. [108] who investigated the fcc-hcp phase stability of $CoCrFe_{1-x}MnNi_x$ HEAs based on a similar approach as in Refs. [101]. Li et al. [108] showed that, also for these alloys, the different finite-temperature excitations tend to stabilize the fcc over the hcp phase, similarly as for CoCrFeMnNi. Since Li et al. [108] mainly focused on the implication on mechanical properties, we discuss their work in more detail in Section 4.4. Several works on entropy contributions beyond the configurational one are compiled in Table 3.

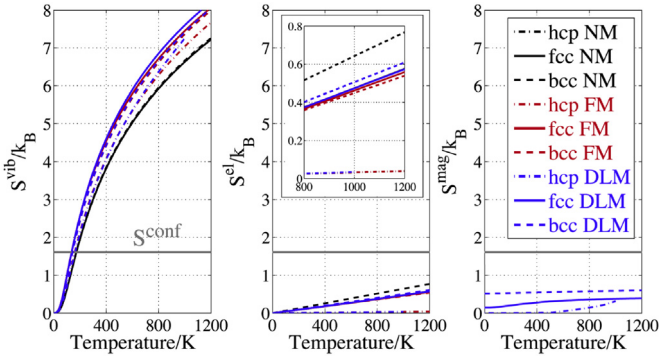


**Fig. 6.** Temperature dependence of the vibrational entropy $S^{\mathrm{vib}}$ (left), the electronic entropy $S^{\mathrm{el}}$ (middle), and the magnetic entropy $S^{\mathrm{mag}}$ (right) for CoCrFeMnNi in comparison with the configurational entropy. Dash-dotted, solid, and dashed curves are for the hcp, fcc, and bcc structures, respectively. Black, red, and blue colors are for the NM, FM, and DLM states, respectively. Gray horizontal lines indicate the configurational entropy $S^{\mathrm{conf}}$. (For interpretation of the references to color in this figure legend, the reader is referred to the web version of this article.)
Source: Taken from Ref. [101].

**Table 3**
Collection of EMTO-CPA based *ab initio* works of HEAs/CCAs including entropy contributions beyond the configurational one. $S_\alpha^{\mathrm{conf}}$: Ideal mixing configurational entropy. $S_\alpha^{\mathrm{vib}}$: Vibrational entropy based on the Debye-Grüneisen model. $S_\alpha^{\mathrm{el}}$: Electronic entropy. $S_\alpha^{\mathrm{mag}}$: Magnetic entropy obtained using the mean field approximation.

| Year | Reference | Alloys | Crystal structures $\alpha$ | Magnetic states | Entropy contributions | | | |
|---|---|---|---|---|---|---|---|---|
| | | | | | $S_\alpha^{\mathrm{conf}}$ | $S_\alpha^{\mathrm{el}}$ | $S_\alpha^{\mathrm{vib}}$ | $S_\alpha^{\mathrm{mag}}$ |
| 2013 | Tian et al. [70] | $Al_xCoCrFeNi$ | fcc, bcc | DLM | ✓ | | | ✓ |
| 2015 | Ma et al. [101] | CoCrFeMnNi | fcc, bcc, hcp | NM, FM, DLM | ✓ | ✓ | ✓ | ✓ |
| 2017 | Li et al. [108] | $CoCrFe_{1-x}MnNi_x$ | fcc, hcp | DLM | ✓ | | ✓ | ✓ |
| | Sun et al. [72] | $Al_xCoCrFeMnNi$ | fcc, bcc | FM, DLM | ✓ | | | ✓ |

For completeness we note that intrinsic point defects such as vacancies can also contribute to the total Gibbs energy in Eq. (4). Explicit investigations for unary materials [63,86] including all relevant excitation mechanisms revealed, however, that the contribution of vacancies to the bulk Gibbs energy is usually negligible. Note that this does not in general apply to derived quantities such as, e.g., the specific heat capacity or thermal expansion coefficient, in particular close to the melting point [63]. Similar studies for HEAs and CCAs have not been performed so far, but one can expect that the contribution of vacancies to the bulk Gibbs energy is likewise negligible for most temperatures. An exception may be temperatures close to the melting point because of the exponentially increasing vacancy concentration. To explicitly compute the vacancy induced Gibbs energy contribution to bulk properties, one needs the Gibbs energy of vacancy formation which in general depends on temperature in a non-Arrhenius fashion [65,109-111]. Due to the additional challenge of a proper statistical sampling over the locally different chemical environments, the few available *ab initio* works for HEAs [112-115] have concentrated on the temperature independent vacancy formation energy at $T = 0$ K. It was shown that the vacancy formation energy strongly depends on the local chemical environment with variations of up to 1 eV and even qualitative differences (e.g., with negative and positive formation energies for Cr).

Note that, while vacancies may not significantly contribute to phase stabilities from a thermodynamic perspective, their migration energetics is of importance for diffusion properties and thus for the kinetics of diffusive phase transformations. A few *ab initio* works have been reported on the migration energies of vacancies [112,114], but we do not go into detail in the present review.

### 3.4. Beyond the Debye-Grüneisen Approximation

As discussed in the previous subsection (Section 3.3), the free energy contribution due to atomic vibrations can be large and can strongly impact phase stabilities. It is therefore important to evaluate the accuracy of the widely used Debye-Grüneisen approximation by explicitly considering lattice vibrations.

For HEAs and CCAs, the impact of atomic vibrations beyond the Debye-Grüneisen model has been investigated only in a few works so far, likely due to the high computational costs. These works employed the quasiharmonic approximation which — for unaries and ordered compounds — has become a common computational technique to obtain an accurate description of the vibrational free energy. In this approximation, the vibrational free energy reads:

**Quasiharmonic approximation**

$$F_\alpha^{\mathrm{vib}}(V,T) = \frac{1}{N}\sum_j^{3N}\left\{\frac{1}{2}\hbar\omega_j(V) + k_B T \ln\left[1 - \exp\left(-\frac{\hbar\omega_j(V)}{k_B T}\right)\right]\right\}. \quad (26)$$

Here, $\hbar$ is the reduced Planck constant and the $\omega_j$ are phonon frequencies (i.e., the energies of the atomic vibrations) which typically have a significant volume dependence and which also implicitly depend on the concentration $\{x_i^\alpha\}$ and the phase $\alpha$. The sum runs over the $3N$ (exact) frequencies for a supercell with $N$ atoms. In general, two well established approaches exist to compute the $\omega_j$, linear response theory [116] and the finite-displacement supercell method (aka direct force constant method) [117-119]. For unaries and ordered compounds with small primitive cells, linear response theory is computationally advantageous as the full phonon spectrum can be obtained from primitive cell calculations. This advantage does not apply anymore to disordered multicomponent systems for which the supercell (with many atoms) equals the primitive cell due to the chemical disorder.

The finite-displacement method works directly with a supercell. Specifically, interatomic force constants are computed by slightly (i.e., within the harmonic regime) displacing atoms in the supercell from their $T = 0$ K equilibrium positions. The force constants determine the key quantity within the harmonic framework, i.e., the dynamical matrix $\underline{D}$, with matrix elements given by:

$$D_{k\chi,l\zeta} = \frac{1}{\sqrt{M_k M_l}}\left[\frac{\partial^2 E_\alpha(\{\mathbf{R}_I\})}{\partial R_{k\chi}\partial R_{l\zeta}}\right]_{\{\mathbf{R}_I^0\}}. \quad (27)$$

Here, $E_\alpha(\{\mathbf{R}_I\})$ is the total electronic energy at $T = 0$ K as used so far, but now extended to depend on the full set of atomic coordinates $\{\mathbf{R}_I\}$ of all atoms in the supercell. The second derivative in Eq. (27) is performed with respect to the atomic coordinate $R_{k\chi}$ ($R_{l\zeta}$) of atom $k$ ($l$) with mass $M_k$ ($M_l$) in spatial direction $\chi$ ($\zeta$) at the equilibrium atomic positions $\{\mathbf{R}_I^0\}$. The phonon frequencies are obtained by diagonalizing the dynamical matrix, i.e.,

$$\underline{D}\mathbf{w}_j = \omega_j^2 \mathbf{w}_j, \quad (28)$$

where $\mathbf{w}_j$ are the corresponding eigenvectors. A number of established tools exist which implement these equations typically as an add-on to existing DFT codes. A collection is given in Ref. [120] (see Table 2 in this reference).

The finite-displacement method requires in general $3N$ calculations. For systems with a high number of symmetries, such as, e.g., unary materials, the actual number of calculations can be drastically reduced. For example, for pure fcc Al in a $3 \times 3 \times 3$ cubic supercell containing 108 atoms, only a single calculation is required to determine the inequivalent force constants and hence the complete set of $\omega_j$'s inherent to the supercell (for a fixed volume). Unfortunately for HEAs and CCAs crystal symmetries cannot be in general employed due to the chemical disorder. For example, a similarly sized supercell for a four-component fcc CoCrFeNi alloy would require $3 \times 108 = 324$ calculations for each considered volume $V$. This example reveals that the quasiharmonic approximation, Eq. (26), is in its standard implementation typically two orders of magnitude computationally more expensive as compared to ordered alloys or unaries. It is therefore not surprising that most of the previous works on the vibrational free energy for HEAs and CCAs relied on the Debye-Grüneisen approximation rather than on the quasiharmonic approximation.

Recently, Wang et al. [121] investigated phase separation of bcc

MoNbTaVW and its subsystems using supercell calculations in conjunction with the quasiharmonic approximation. They computed the free energies of in total 178 single phases for each of the 5 pure elements, 130 ordered binaries, 2 ordered quaternaries, 10 disordered binaries, 10 disordered ternaries, 5 disordered quaternaries, 1 quinary disordered MoNbTaVW, and 15 partially disordered B2 phases. The fully and partially disordered phases were modeled using the SQS technique. One result from these calculations is that the high-temperature quaternary bcc MoNbTaW HEA undergoes a phase transition at temperatures below 594 K into a partially-ordered B2 (NbTa)(MoW). Körmann and Sluiter [102] studied the same transition employing similar techniques (VASP + supercell) except for using the Debye-Grüneisen approach, Eq. (20). The resulting transition temperature from the work of Körmann and Sluiter [102], considering only vibrations for consistency, is 508 K and thus reasonably close to the one found by Wang et al. [121]. Although one has to be careful in transferring this finding to HEAs and CCAs in general, it indicates that the Debye-Grüneisen model is a reasonable starting point for the exploration of phase stabilities in multicomponent systems.

The wave-vector dependence $\omega_j(\mathbf{q})$ of the phonon frequencies, i.e., the phonon spectrum in reciprocal space, provides an important analysis of atomic vibrations. The challenge in computing phonon spectra of disordered alloys is related to the missing crystal symmetries. An approach which can overcome this issue is the band unfolding method [123,124] which has been recently employed to study binary solid solutions [125,126]. Körmann et al. [122] applied the band unfolding method to investigate a wide range of bcc refractory alloys, from random binaries up to five-component HEAs. As an example, we display in Fig. 7 the computed phonon spectra of the disordered bcc NbTaTiVW HEA and several of its subsystems (first column on the left). These multicomponent phonon spectra show a significantly different appearance than (quasiharmonic) phonon spectra of unary materials or ordered compounds, which are made of well-defined phonon bands. Körmann et al. [122] showed that spectra of disordered alloys show a strong broadening in their spectral function (spread of colors in Fig. 7) above a frequency of about 4 THz. The main origin of the broadening originates from the atomic mass fluctuations. The importance of the atomic masses can be intuited by the decomposition of the total phonon spectra (left column) into the contribution from each of the involved elements (all other plots in Fig. 7). For example, for the VW alloy (first row) it is well visible that the light V [Fig. 7(b)] is mostly responsible for the high frequency spectrum whereas the heavier W [Fig. 7(c)] determines the low frequency spectrum. While mass fluctuations are the dominant factor for the phonon broadening, Körmann et al. [122] further showed that force fluctuations are likewise important to obtain accurate spectra.

Körmann et al. [122] used the computed phonon spectra, specifically the phonon density of states, to derive the harmonic vibrational entropy. Their results for several of the investigated alloys at a temperature of 1500 K are reproduced in Fig. 8 (black dots). It can be seen that taking only mass fluctuations into account (red lines) is a very good approximation for the vibrational entropy. Taking only force constant fluctuations into account (blue lines) and the harmonic Debye results that we have additionally included (gray crosses) show slightly larger deviations with the full phonon based calculations (of up to 5% for the VW alloy). Note that this does not necessarily imply a similar error for phase stability considerations as there might be effective error cancellation.

More recently, Jin et al. [127] studied the lattice expansion and specific heat capacity of several magnetic fcc Co–Cr–Fe–Ni alloys employing the quasiharmonic approximation based on ferromagnetic calculations. The comparison with experimental data revealed significant magnetostriction effects in particular for FeNi which could not be captured when neglecting the impact of spin-phonon contributions. Indeed, the importance of magnetic excitations on the vibrational contribution has been also shown in other studies [50,128-130]. To account for such coupling effects, the so-called spin-space averaging method was originally developed for magnetically disordered systems [128,129,131] and later extended to ordered compounds [50]. In this approach, the magnetic degree of freedom is adiabatically decoupled from the atomic motion and a statistical average is performed over many magnetic configurations to compute effective force constants. If coupled to the magnetic energy contribution, Eq. (17), the approach enables the computation of vibrations over the whole range of temperatures across the magnetic transition temperature [131]. Recently, Ikeda et al. [126] combined this approach with the band unfolding method to investigate magnetic random solid solutions. The application to binary Fe–Pd and Fe–Pt random alloys revealed the predictive power of this method for the computation of vibrations in magnetic random alloys exposing this method as a promising route for computing lattice vibrations of magnetic HEAs.

At high temperatures in particular close to the melting temperature, the quasiharmonic approximation, Eq. (26), becomes less accurate in describing the vibrational free energy. The reason is the contribution originating from *explicit* anharmonic vibrations, i.e., phonon-phonon interactions, which are not contained in the second derivative of Eq. (27) but rather require the inclusion of higher order derivatives. It is in principle possible to capture the anharmonic vibrations by employing *ab initio* MD simulations. However, computing the corresponding anharmonic free energy brute-force by MD is computationally prohibitive due to the entropic contribution, and efficient schemes to coarse grain the configuration space are indispensable [65]. One recent development in this respect is the TU-TILD approach (*two-stage upsampled thermodynamic integration using Langevin dynamics*) [132] that has strongly improved the efficiency of calculating anharmonic free energies even for systems with strong anharmonicity. So far the explicitly anharmonic free energy was investigated mostly for unary materials and ordered compounds [63,74,86,91,132-134]. To the best of our knowledge, such studies are lacking for HEAs/CCAs, although a number of *ab initio* MD simulations has been performed mainly in combination with MC sampling [135-138] (cf. Table 7 and Section 3.6).

We finally note that *ab initio* MD simulations give also access to liquid properties such as, e.g., the pair-distribution function [139,140]. The determination of the Gibbs energy of the liquid phase [i.e., $\alpha$ = liquid in Eqs. (3) and (4)] is in principle also possible but very challenging. Very recent developments (TOR-TILD method by Zhu et al. [51]) made an efficient calculation for unary materials possible. We also note recent advances in computing the entropy of liquids by taking *ab initio* MD computed pair correlation functions into account [141]. Future extensions towards multicomponent systems may provide helpful information for the design of HEAs/CCAs via the casting route.

### 3.5. Calculation of the Critical Magnetic Temperature

For magnetic HEAs and CCAs, finite-temperature magnetic fluctuations as well as the degree of magnetic ordering play an important role for the thermodynamic stability and for mechanical properties. As discussed in Section 3.3, a complete inclusion of finite-temperature magnetic effects and the computation of the magnetic free energy from *ab initio* constitutes a formidable task. A common approximation to include magnetic effects is to resort to magnetically fully disordered, paramagnetic simulations corresponding to the high temperature limit. Efficient schemes exist to mimic a random magnetic alloy, e.g., the DLM method, and analytic magnetic free energy expressions are readily available as discussed in Section 3.3 [Eqs. (18)–(19)]. However, this high temperature approximation may not be the best one for the considered system and a low temperature approximation considering magnetically ordered (e.g., ferromagnetic) configurations may be more suitable. Magnetically ordered configurations are well accessible by ground-state spin-polarized DFT calculations and the magnetic entropy for this low temperature limit becomes zero.

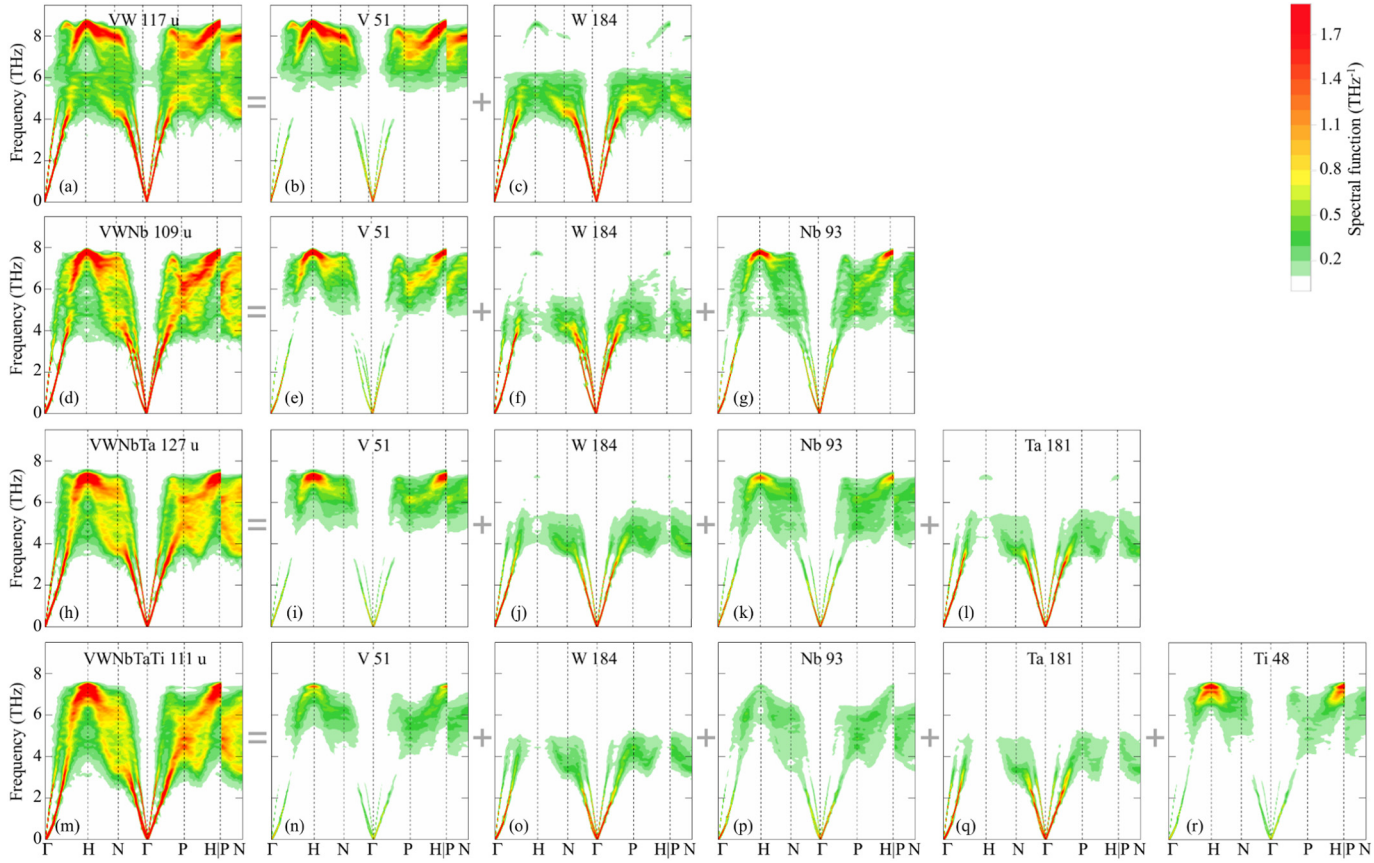


**Fig. 7.** Phonon spectra of disordered bcc refractory alloys (binary to quinary from top to bottom) decomposed into contributions of the individual chemical elements (numbers indicate the atomic mass) using the projection scheme as introduced in Ref. [122]. The seemingly weaker contribution of each element when going from top to bottom is a consequence of the reduced concentration of each element in the given alloy, i.e., from 50 at.% for the binary (first row) to 20 at.% in the bottom row (quinary). (For interpretation of the references to color in this figure, the reader is referred to the web version of this article.)
Source: Taken from Ref. [122].

The key quantity which ultimately determines whether a magnetically ordered or disordered configuration is — at a given temperature — the more realistic magnetic scenario, and hence whether the high-temperature magnetic free energy approximation [Eqs. (18)–(19)] is applicable, is the critical magnetic temperature. The knowledge of the critical temperature thus plays an important role in any *ab initio* calculation of magnetic alloys providing the inherent justification of the underlying magnetic treatment and determining in the first place whether calculations shall be carried out including magnetic disorder (e.g., via the DLM approach) or whether calculations shall be performed based on magnetically ordered, e.g., ferromagnetic configurations. For ferro- or ferrimagnetic alloys, the critical magnetic temperature is known as the Curie temperature $T_C$ and for antiferromagnetic alloys as the Néel temperature $T_N$. Several calculations suggest ferrimagnetic-like ordering for some HEAs, e.g., an antiferromagnetic alignment of Cr and Mn in CoCrFeMnNi [101]. Since most magnetic HEAs and CCAs are prone to ferro- or ferrimagnetic ordering, we refer in the following to the Curie temperature $T_C$ but note that the discussed methodologies are generic and also applicable to antiferromagnetic alloys.

The computation of $T_C$ of HEAs and CCAs has been the subject of several studies. Most works in this respect employed the EMTO-CPA framework and are summarized in Table 4. The most common approach to derive the magnetic ordering temperature from *ab initio* calculations relies on a mapping of the *ab initio* energetics onto the classical Heisenberg Hamiltonian,

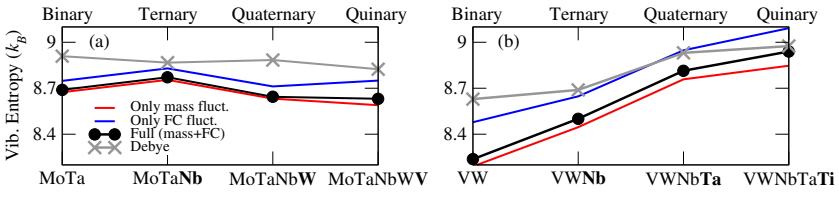


**Fig. 8.** Vibrational entropy for several disordered bcc refractory alloys at 1500 K derived from the phonon density of states (harmonic approximation). The black solid circles include both mass and force constant fluctuations. The red and blue lines represent the vibrational entropy derived from the approximate spectra including either mass or force constant fluctuations. These data is based on the work of Körmann et al. [122]. Additionally, the vibrational entropy based on the harmonic Debye approximation has been added (gray crosses). The harmonic Debye approximation neglects the volume dependence of the Debye-Grüneisen approach and considers only the Debye temperature at the equilibrium volume calculated according to Eq. (23). (For interpretation of the references to color in this figure legend, the reader is referred to the web version of this article.)

**Table 4**
*Ab initio* works focusing on the Curie temperature and magnetic ordering of HEAs/CCAs.

| Year | Reference | Alloys | Crystal structures | Magnetic states | $T_C$ calculation |
|---|---|---|---|---|---|
| 2015 | Körmann et al. [142] | Various CoFeNi base HEAs | fcc | FM, DLM | Mean field |
| | Ma et al. [101] | CoCrFeMnNi | fcc, bcc, hcp | FM, DLM | Mean field |
| 2016 | Huang et al. [143] | $Al_x$CoCrFeNi | fcc, bcc | FM | Monte Carlo |
| 2017 | Song et al. [69] | CoFeNi, CoCrFeNi, CoCrFeMnNi | fcc | FM, DLM | Mean field + distortions |
| | Sun et al. [72] | $Al_x$CoCrFeNiMn | fcc, bcc | FM, DLM | Mean field |
| | Huang et al. [144] | CoCuFeNi, CoCuFeNiX (X = V, Cr, Mn) | fcc, bcc, hcp | FM, DLM | Mean field |
| 2018 | Huang et al. [145] | $Al_x$CoCrFeMn | fcc, bcc, hcp | FM, DLM | Mean field |
| | Huang et al. [146] | 42 alloys | fcc, bcc | FM, DLM | Mean field |
| | Huang et al. [146] | CoCrFeMnNi | fcc | FM | Monte Carlo |

$$\mathscr{H}^{\mathrm{mag}} = -\sum_{ij} J_{ij}\,\overrightarrow{m_i}\,\overrightarrow{m_j}, \tag{29}$$

where $J_{ij}$ denotes the magnetic interaction (exchange parameter) between local magnetic moments $\overrightarrow{m_i}$ and $\overrightarrow{m_j}$ located at lattice sites $i$ and $j$. In practice, the $J_{ij}$ parameters are typically computed using perturbation theory [147] which, if combined with CPA, allows one to evaluate additionally the impact of magnetic disorder on these parameters (see, e.g., Ref. [148]). Alternatively, the energies of supercell calculations with different (typically collinear) magnetic configurations can be fitted to Eq. (29) (see, e.g., Refs. [149,150]). Note that the model above captures mainly the magnetic energetics due to the transverse magnetic moment degree of freedom. For unaries and selected binaries several extensions of the model exist to account for higher order coupling terms or longitudinal spin fluctuations, i.e., variations in the magnitude of the local moments (see, e.g., Refs. [88,151]). However, these methods have not yet been extended to multicomponent alloys.

Besides the different ways of deriving the magnetic exchange parameters, there are also distinct strategies to solve Eq. (29). The methods range from approximate analytic solutions for $T_C$ based on mean field or Green's function based techniques (e.g., random phase approximation) to numerical approaches such as classical and quantum Monte Carlo simulations (see, e.g., Refs. [130,152], and references therein). In Monte Carlo simulations, $T_C$ is usually computed by identifying the singularity in the magnetic susceptibility [cf. Fig. 10 (b) below] or the peak in the specific heat contribution (see, e.g., Refs. [87,130,152]). For HEAs, two different approaches have been so far employed to compute $T_C$, classical Monte Carlo simulations as well as the mean field approach. The latter is computationally significantly more efficient and has been thus employed more often (see Table 4). Note however that mean field approximations are known to usually overestimate $T_C$.

The mean field approach was originally proposed for diluted semiconductors and a single magnetic species by Sato et al. [153] and later extended to multi-magnetic element alloys in Körmann et al. [142]. The alloy is considered to be an effective medium mixture of a magnetic and a non-magnetic species. Under this assumption, the mean field Curie temperature is obtained as [142,153]:

**Mean field approximation for the Curie temperature**

$$k_B T_C = \frac{2}{3x}(E_{\mathrm{FM}} - E_{\mathrm{DLM}}). \tag{30}$$

Here, $x$ denotes the fraction of magnetic elements and $E_{\mathrm{FM}}$ and $E_{\mathrm{DLM}}$ denote the total energies of the considered alloy in the ferromagnetic and disordered local moment (paramagnetic) state. The approach is computationally very efficient because only the two total energies, $E_{\mathrm{FM}}$ and $E_{\mathrm{DLM}}$, are required instead of an explicit determination of the $J_{ij}$ parameters and additional Monte Carlo simulations.

Körmann et al. [142] employed the mean field approach, Eq. (30), to explore the Curie temperatures for a large range of different HEAs and highlighted the tuneability of $T_C$ upon alloying. The energies entering Eq. (30) were determined based on EMTO-CPA calculations. As an example, we show in Fig. 9 the predicted "Treasure Maps" for CoCrFeNiM (M = Ag, Au, Pd, Cu) alloys. The concentrations marked with filled circles and stars were compared with experimental data and revealed an excellent agreement [142]. Such maps are in particular useful to explore and design alloys with well-defined magnetic properties for, e.g., potential applications in magnetic refrigeration technology.

Huang et al. [143] went beyond the mean field approximation and employed Monte Carlo simulations to investigate the $T_C$ of $Al_x$CoCrFeNi alloys as a function of the Al concentration and crystal structure. The $J_{ij}$ parameters were determined from perturbation theory [147] based on EMTO-CPA calculations in the FM state.[3] It was found that the bcc structure, which can be stabilized under certain Al concentrations (see Section 3.1) reveals a larger $T_C$ (355 K) as the fcc structure (205 K). Their computed magnetizations and susceptibilities are shown in Fig. 10(a) and (b), respectively.

The impact of crystal structure on $T_C$ for HEAs was also explored for the CoCrFeMnNi alloy by Ma et al. [101] and for $Al_x$CoCrFeMnNi alloys by Sun et al. [72]. More recently Huang et al. [146] extended these calculations to more than 42 alloys. In all cases, it was found that the computed $T_C$'s for the bcc crystal structures are significantly larger than the ones for the corresponding fcc crystal structures [72,101,146].

All calculations of $T_C$ mentioned so far were based on the EMTO-CPA approach, i.e., local lattice distortions were ignored. Recently, Song et al. [69] investigated the impact of local lattice distortions on $T_C$ for several multicomponent alloys employing Eq. (30) in combination with the supercell approach for the computation of the total energies $E_{\mathrm{FM}}$ and $E_{\mathrm{DLM}}$. Since at present no unrelaxed calculations based on the supercell model have been reported for $T_C$,[4] the results in Ref. [69] including local relaxations can at present only be compared with previous EMTO-CPA calculations. Here, it is found that apart from the CoCrFeMnNi alloy, for which a slight increase in $T_C$ is observed ($< 10$ K), the distortions somewhat decrease $T_C$ for fcc CoFeNi and CoCrFeNi as compared to the EMTO-CPA predictions by $\approx$ 150 and 70 K, respectively [69].

For fcc CoCrFeNi, Niu et al. [154] investigated the energetic and

[3] We note that the $J_{ij}$ parameters can depend on the global magnetic state. This can have consequences for $T_C$ predictions, e.g., if $J_{ij}$ are computed from the DLM state see, e.g., Table IV in Ref. [148].

[4] Song et al. [69] mentioned computational difficulties in converging the paramagnetic calculations for the considered alloys on an unrelaxed lattice.

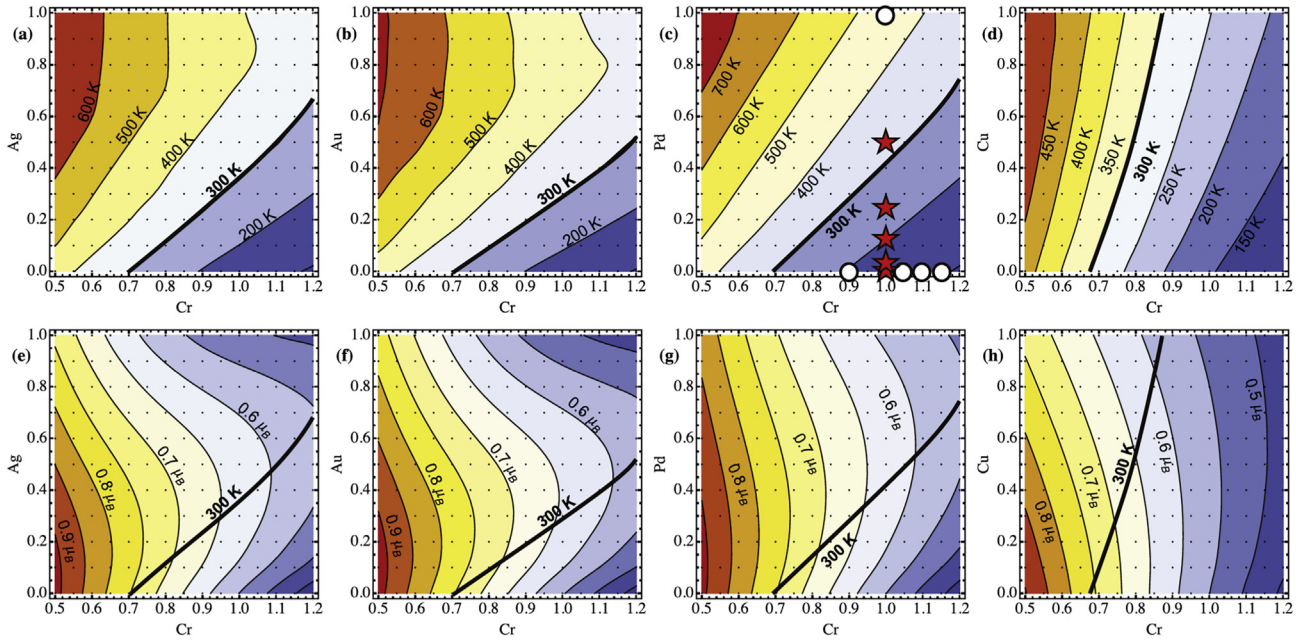


**Fig. 9.** "Treasure Maps" of (a)–(d) $T_C$ and (e)–(h) magnetization for CoCrFeNiM alloys. The *x*- and *y*-axis define the Cr- and M (= Ag, Au, Pd, Cu)-content. Thick lines indicate room temperature values. The symbols (stars and circles) indicate experimentally explored compositions.
Source: Reproduced from Ref. [142] with the permission of AIP Publishing.

magnetic properties using the supercell approach. It was found that the local atomic magnetic moments strongly depend on their surrounding moments as shown in Fig. 11. Particularly, Cr tends to have negative magnetic moments resulting in magnetic frustration of Cr moments when surrounded by other Cr atoms. Including the configurational entropy, Eq. (7), a Cr-ordered $L1_2$ phase has been predicted with larger saturation magnetization. Indeed, the accompanying experiments revealed an alloy with twice larger saturation magnetization and significantly enhanced $T_C$ [154]. This example exposes the possibility to explore the impact of $T_C$ due to chemical ordering.

### 3.6. Chemical Long- and Short-range Order

The methodology discussed until this point has mostly relied on the decomposition of the free energy as given in Eq. (6). The underlying assumption of this decomposition is that the system can be reasonably well represented by a single atomic configuration (possibly with a high degeneracy captured by the configurational entropy) which applies to ordered, disordered, and partially disordered phases. As already mentioned in Section 3.2 with reference to Fig. 4, the situation is much more complex close to the transition temperatures where the alloys are prone to chemical short-range order (SRO). The calculation of the free energy requires then the sampling over many locally distinct chemical configurations as indicated in Eq. (5). In principle, for each configuration the free energy including electronic, magnetic, and vibrational excitations could be calculated utilizing the free energy Born-Oppenheimer approximation and also the methods discussed in Sections 3.3 and 3.4. Due to the computational requirements, typically only the $T = 0$ K ground state energy is calculated for each configuration. Some exceptions employing, e.g., combined MC-MD methods will be discussed below.

A direct and complete *ab initio* determination of the free energy according to Eq. (5) is not possible even when only the $T = 0$ K energy for each configuration is considered. However, approaches exist and will be discussed to address the problem to some extent. Of primary importance is the computation of the order-disorder transition temperatures, i.e., the critical temperatures at which a specific long-range chemical ordering occurs or vanishes. The knowledge of these critical temperatures is crucial as it ultimately determines the alloy's chemical phase stability and at which temperatures a HEA is prone to long-range ordering. Similarly as remarked for the critical *magnetic* temperature in Section 3.5, the critical order-disorder transition temperatures determine the appropriate chemical state and simulation cell for the *ab initio* simulations at a given temperature. Under certain circumstances (detailed below), a critical temperature can be obtained with the previously introduced methods, i.e., under the ideal mixing assumption. A more advanced treatment is necessary if one is interested in the explicit inclusion of chemical SRO which becomes important at temperatures near the order-disorder transitions. The corresponding approaches typically utilize a mapping of the *ab initio* energetics onto a simpler Hamiltonian which is solved using for example MC simulations, in close analogy to the treatment discussed for the transverse magnetic degree-of-freedom. These approaches can be used to obtain a more accurate transition temperature and give also access to thermodynamic properties (see Fig. 15) as will be discussed in the present subsection.

An order-disorder transition can be approximately obtained based on, e.g., the mean field approximation or the Bragg-Williams approach [55], if the set of phases $\alpha$ and their mole fractions $\{x_i^\alpha\}$ that compete in the transition are known *a priori*. Then for each of the phases the respective Gibbs energy is calculated for the *whole* temperature range according to Eqs. (4) and (6) and using the set of techniques introduced in Sections 3.3 and 3.4 within the ideal mixing assumption. As already mentioned, if disorder is present on a certain sublattice only then the configurational entropy needs to be appropriately adjusted. Crossing points of the Gibbs energies are the estimates for the transition temperatures. Note that the assumption of ideal mixing renders transitions to be of first order whereas many order-disorder transitions are of second order. This highlights the importance of taking chemical short-range order into account discussed below.

Körmann and Sluiter [102] utilized such a mean field approach to investigate the bcc MoNbTaW HEA. From previous simulations, it had been reported that the high temperature disordered bcc A2 solid solution of MoNbTaW transforms into a partially ordered B2 phase at lower temperatures, with Mo and W randomly mixed on one sublattice (cf. Fig. 4; light and dark blue balls) and Nb and Ta on another (light and dark red balls). Körmann and Sluiter [102] computed the Gibbs

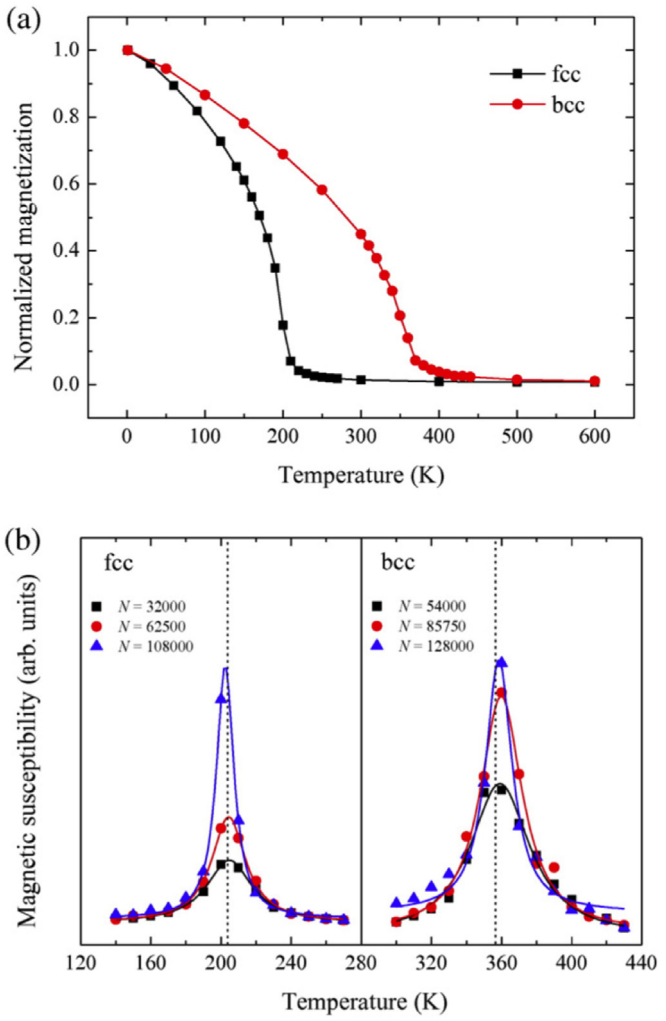


**Fig. 10.** Monte Carlo simulations showing the (a) normalized magnetization and (b) susceptibility for AlCoCrFeNi in the fcc and bcc phase. The magnetic susceptibilities are shown for different simulation cell sizes revealing the impact of finite-size effects. The Curie temperature in the bcc phase is often found to be larger for magnetic HEAs (see text for details).
Source: Taken from Ref. [143].

energies for both these phases using the ideal mixing approximation and derived the transition temperature investigating various effects. Employing unrelaxed calculations without finite-temperature excitations, they found a transition temperature of 717 K. Finite-temperature excitations turned out to be negligible, but lattice distortions had a significant impact reducing the transition temperature down to 508 K.

The key challenge usually lies in finding for a given alloy system the relevant phases competing with the single-phase solid solution. A possible but computationally expensive approach is to choose a large pool of candidate phases, compute all Gibbs energies, choose at each temperature the phase with the lowest Gibbs energy (or a combination of phases at different compositions), and determine the respective crossing points. The work of Wang et al. [121] on the bcc Mo–Nb–Ta–V–W system including in total 178 phases (introduced already in Section 3.3) can be classified as such an approach. By computing the individual $G_\alpha(P, T, \{x_i^\alpha\})$ of each phase including vibrational and configurational (ideal mixing) entropy contributions, they determined the phase separation and ordering tendencies of the quinary and quaternary bcc Mo–Nb–Ta–V–W HEAs.

To reduce computational requirements, a selection of potential phases can be attempted, e.g., by resorting to empirical rules and selecting the most stable binary combinations as discussed in Section 3.1. However, as suggested by Fig. 4 (b), a HEA does not necessarily decompose into unaries and/or binaries only, so that additional phases need to be considered as well (e.g., for bcc MoNbTaW the B2 ordered phase as just discussed). An alternative is to employ prior to the actual *ab initio* calculations thermodynamic modeling techniques such as, e.g., the CALPHAD approach to select potential candidate phases. One possible route was utilized by Rogal et al. [66] who studied partial sublattice ordering in $Al_{15}Hf_{25}Sc_{10}Ti_{25}Zr_{25}$. Inspecting the binary phase diagrams of the involved elements, a partially ordered $D0_{19}$ structure where Al is constrained to a specific sublattice was selected as a potential candidate phase. Indeed, a $D0_{19}$ to hcp A3 transition was found at 1230 K (see Fig. 12) in good agreement with corresponding experimental measurements. We note that partial sublattice ordering was also investigated for CoCrCuFeNi with a similar *ab initio* approach, resulting in the prediction of an $L1_2$ phase [155].

It should be stressed that, besides forcing the order-disorder transition to be of first order type, the assumption of ideal mixing also introduces an error in the predicted transition temperature [102,163]. To go beyond and improve the description, chemical SRO needs to be taken into account. In order to quantify chemical SRO it is convenient to introduce the Warren–Cowley SRO parameters [172,173],

$$\alpha_{ij}^m \equiv 1 - \frac{c_{ij}^m}{c_i c_j}, \tag{31}$$

where $c_i$ is the concentration of the $i$'th element, and $c_{ij}^m$ is the probability to find the combination of the $i$'th and the $j$'th elements in the $m$'th pair cluster. If there is no SRO, the probability $c_{ij}^m$ equals the product $c_i c_j$ and the corresponding $\alpha_{ij}^m$ vanishes. Temperature dependent Fourier transformed Warren–Cowley SRO parameters can be extracted from diffuse-scattering experiments providing an elegant link between experimentally accessible quantities and DFT simulations. One possibility to include SRO is to explicitly set up *a priori* known configurations mimicking a specific chemical SRO [167], i.e., constructing a supercell which matches specific SRO parameters $\alpha_{ij}^m$. However, usually the degree of SRO and hence the $\alpha_{ij}^m$ and thus the relevant configurations are unknown.

A natural way to study SRO, requiring no *a priori* knowledge about specific configurations, is to perform *ab initio* Monte Carlo (MC) simulations, where at each MC step the energies are directly computed by DFT calculations. Due to the computational cost of this technique only a few works have been reported so far for HEAs [157,161,174]. Tamm et al. [157] investigated the chemical SRO in CoCrNi and CoCrFeNi, and found a strong Cr–Cr repulsion at low temperatures for the first neighboring shells in both alloys. Such approaches suffer, however, if secondary phases form which may introduce large strains at the interphase boundaries. In this case, large and computationally even more expensive supercells are required to ensure that the strain energy does not dominate the total energy which ultimately determines the predicted ordering and phase formation tendencies. To overcome this issue, Niu et al. [174] proposed a multi-cell Monte Carlo scheme in which two parallel supercells are employed allowing for atoms to swap between the cells as well as within both cells. The approach thus circumvents the issue of an interface energy between both phases (supercells) and might be therefore useful for studying ordering or phase decomposition where large mismatch between different phases is anticipated. Niu et al. [174] applied the method to study phase decomposition of bcc HfNbTaZr.

*Ab initio* molecular dynamics (MD) simulations were also combined with MC simulations in order to include the impact of atomic vibrations at finite temperatures [135-137]. These hybrid MD/MC simulations were performed for bcc MoNbTaW [135,137], where the elements were exchanged on the lattice sites according to the MC formalism after every 10 MD steps. Fig. 13 shows the obtained partial radial distribution functions at $T = 300$ K and $T = 1800$ K (inset). It was found that at $T = 300$ K, the Mo–Ta pairs have the largest probability in the first shell indicating their strong tendency for SRO. The different peak positions of

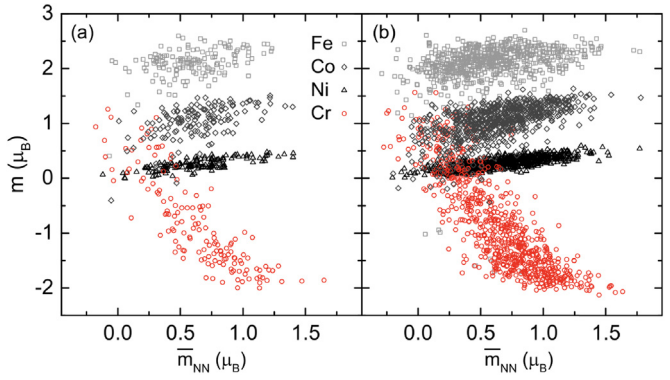


**Fig. 11.** Atomic magnetic moment, $m$, as a function of the average magnetic moment, $\overline{m}_{NN}$, over the 12 first nearest-neighbor atoms from (a) a 24-atom SQS and (b) a 120-atom SQS for fcc CoCrFeNi.
Source: Reproduced from Ref. [154] with the permission of AIP Publishing.

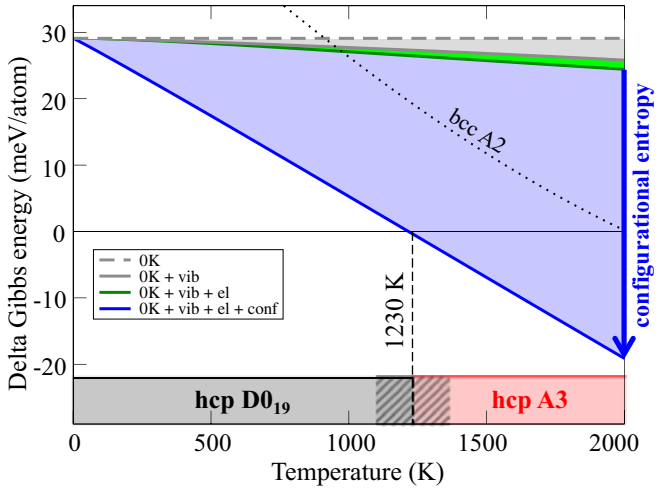


**Fig. 12.** Difference in the Gibbs energies of $D0_{19}$ and A3 hcp for the $Al_{15}Hf_{25}Sc_{10}Ti_{25}Zr_{25}$ at% HEA as a function of temperature ($D0_{19}$ corresponds to the zero line). The Gibbs energy difference is decomposed into the $T = 0$ K energy (0 K), the vibrational (vib), electronic (el), and configurational (conf) contribution. The final curve corresponds to the blue solid line, resulting in a transition temperature of 1230 K as indicated by the vertical dashed line. The dotted line shows the difference between the Gibbs energy of $D0_{19}$ and bcc A2 containing all contributions. (For interpretation of the references to color in this figure legend, the reader is referred to the web version of this article.)
Source: Taken from Ref. [66].

the partial radial distributions for different chemical pairs further indicate rather different bond lengths depending on the considered chemical pairs. In general, such MC simulations do not directly provide the configurational entropy which requires additional statistical treatments discussed below. Also, the computational costs of direct *ab initio* MC approaches are very high, because each MC and MD step requires a full DFT calculation.

Several alternative DFT-based methods exist in literature to account for SRO that are computationally more efficient than full DFT-based MC simulations. An overview over the works employed so far for HEAs and CCAs is given in Table 5. After briefly introducing the methods, we focus on their previous applications to HEAs and CCAs. The methods can be broadly categorized into two classes. One class is based on perturbation theory combined with the CPA approach and includes the concentration wave method [96,175,176] and the generalized perturbation method (GPM) [148,177]. The other class can be broadly defined as comprising cluster expansion approaches (see, e.g., Refs. [178,179]).

Both, the concentration wave and generalized perturbation method, are based on the CPA formalism (Section 3.2) which makes them particularly suitable for HEAs. The concentration wave formalism is based on the idea that an alloy can be described as a variation of chemical components from site to site which can be formally defined as a wave [96,156,160,169,175,176]. Infinitesimally small concentration variations of these waves are sampled allowing one to determine the alloy's chemical stability matrix in reciprocal space. The concentration wave method was recently applied to study various HEAs and CCAs [156,160,169,170]. As an example, we show in Fig. 14 the results [156] for the chemical stability matrix, $S^{(2)}_{\nu\mu}(\mathbf{k})$, of fcc AlCoCrFeNi, where $\nu$ and $\mu$ represent the atomic pairs. From the analysis of $S^{(2)}_{\nu\mu}(\mathbf{k})$, the A2 ordering tendency of the alloy can be determined by inspecting the **X**-point. In this example, the Cr–Al pairs provide the strongest contribution, i.e., largest peak for this wave vector. The concentration wave method can be also combined, e.g., with a mean field approach to derive the Warren–Cowley parameters at finite temperatures (see, e.g., Ref. [156]).

Within the GPM approach, the alloy is mapped onto an Ising-type Hamiltonian with effective cluster interactions which are determined by a perturbative approach [148,163,177]. To arrive at finite temperatures, the GPM derived real-space interactions are usually combined with MC simulations to determine SRO parameters and order-disorder transitions [163]. Following this route, the GPM was recently applied to study phase transitions and SRO in MoNbTaW [163]. Specifically, Körmann et al. [163] employed the so-called screened generalized perturbation method (SGPM) [148] which additionally includes a screening correction to the conventional GPM formalism. Based on the computed pair interactions, MC simulations were carried out with a focus on long-ranged interactions. Fig. 15 exemplifies the impact of taking long-ranged effective pair interactions on (a)–(d) the specific heat capacity and (e)–(h) on the lattice site occupation at (0,0,0) and (1/2,1/2,1/2) (in reduced coordinates) into account. It can be seen that the B2-A2 order-disorder phase-transition temperature [peak at higher temperatures in Fig. 15(a)] decreases by almost a factor of two to a value of ~ 750 K if long-ranged interactions are taken into account, i.e., by going from Fig. 15(a) to (d). If only nearest-neighbor pair interactions are taken into account, Fig. 15(a), a transition temperature of ~ 1250 K is found in good agreement with results based on a cluster expansion (also restricted to nearest-neighbor pair interactions), see below. At low temperatures, the alloy separates into a B32 NbW and a B2 MoTa alloy consistent with previous calculations [168]. We note that a more recent study corroborated the finding of long-ranged interactions in bcc NbMoTaW and traced them back to Fermi-surface nesting effects [169]. The concentration wave method and GPM are computationally very efficient but are restricted to the lattice on which the CPA calculations are carried out. A main limitation of both methods is the neglect of lattice relaxation effects. The supercell counterpart of these methods is given by the cluster expansion (CE) technique.

Within CE, the alloy is also mapped onto an Ising-type Hamiltonian as in GPM. The effective cluster interactions can be obtained, e.g., by the Connolly-Williams method (aka structure inversion method) [180], in which the energies of a sufficiently large pool of DFT supercell calculations are used to fit the cluster interactions. Since the energies are obtained from supercell calculations the inclusion of local lattice relaxations is straightforward, which is a key advantage of the CE. The cluster expanded Hamiltonian can then be solved, e.g., by MC techniques.

The CE was utilized in combination with MC simulations to compute the Warren–Cowley SRO parameters of bcc MoNbTaVW by Toda-Caraballo and Rivera-Díaz-del Castillo [181] and Toda-Caraballo et al. [32]. Toda-Caraballo et al. [32] employed a 2000-atom supercell model where chemical point, pair, and three-body interactions were included. The dominant contributions were found to arise from the first and second pair interactions [158]. Fig. 16 shows their computed

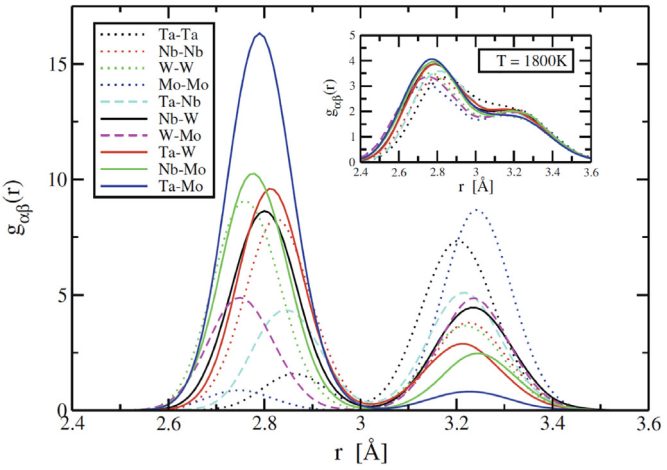


**Fig. 13.** Partial radial distribution functions [denoted as $g_{\alpha\beta}(r)$] of bcc MoNbTaW at $T = 300$ K obtained using hybrid MC/MD simulations. Inset: $T = 1800$ K.
Source: Taken from Ref. [137].

Warren–Cowley SRO parameters for the first and second neighboring shell as a function of temperature for this alloy. A strong tendency of Mo–Ta pairs in the first shell (most negative $\alpha$ parameter) can be seen indicating the strong role of Mo–Ta SRO in this alloy. MC simulations were also used to analyze the order-disorder phase transition in bcc MoNbTaW by Huhn and Widom [135] and Huhn [136]. In these works, the dependence of chemical SRO on temperature was examined using nearest-neighbor pair interactions derived from a CE. A transition from disordered A2 to partially ordered B2 at 1280 K was found similarly as in Ref. [163] when nearest-neighbor interactions were included, see also the comparison for the site occupations reported in Refs. [136,163] shown in Fig. 15(e).

Progress has been also made in adding the magnetic degree of freedom into the CE [159,182,183]. For example, Wróbel et al. [159] and Lavrentiev et al. [183] investigated the ordering in Cr–Fe–Ni and its binary subsystems employing a magnetic CE as well as the conventional CE in combination with MC simulations. As an example, we show in Fig. 17 the results of Wróbel et al. [159] for the computed order-disorder temperatures of bcc and fcc Cr–Fe–Ni alloys.

Another CE for a HEA was performed by Nguyen et al. [165] who investigated the chemical interactions in bcc Al–Co–Fe–Ni–Ti. They computed the order-disorder phase transition in this system and reported a new partially-ordered $D0_3$ phase below 973 K consisting mainly of Ni and Al.

An alternative to MC simulations is the cluster variation method (see, e.g., Ref. [178]) in which an approximate expression for the configurational entropy is provided by taking into account correlations up to a certain cluster size. The CVM was recently applied by Schön et al. [168] to study the phase stability of bcc Mo–Nb–Ta–V–W. They found that the configurational entropy has only a small effect on the phase transitions and that the competition between interactions in the solid solution is the relevant factor behind the observed stabilization of the disordered states in the investigated HEA. A similar finding was previously made by Körmann et al. [163] for bcc MoNbTaW, where the long-ranged interactions resulted into frustrated configurations thus stabilizing the solid solution. An advantage of the CVM is that it provides analytic expressions linking the correlation functions to the configurational entropy. It is therewith possible to link the CVM expressions to correlation functions obtained via MC simulations. In this way, Widom [184] extracted the configurational entropy from MC simulations for bcc CrMoNbV and NbTiVZr alloys.

A more approximate approach, but technically far simpler and thus easier to implement compared to the CVM, is the so-called quasichemical approximation (see, e.g., Ref. [185]). This approximation allows one to investigate in a straightforward manner a large amount of phases, e.g., by resorting to *ab initio* databases. Based on this approach, Lederer et al. [164] performed a high-throughput study using the data in AFLOW [186] and evaluated the order-disorder phase-transition temperatures employing the quasichemical approximation. They evaluated the cross-validation (CV) score for each chemical combination. For those showing a CV score of less than 50 meV, they evaluated the phase stability. In total, their approach covered 1110 quaternary and 130 quinary combinations, out of which 571 alloys were identified as solid solution formers. Among these alloys, 17 were verified as single-phase solutions by experiment.

## 4. Implications on Mechanical Properties

### 4.1. Impact of Alloy Composition and Phase Stability on Elastic Properties

Elastic properties of HEAs and CCAs have been the subject of about thirty *ab initio* works so far, see Table 6. The majority of works employed EMTO-CPA calculations due to its computational efficiency as we have discussed in Section 3.2 [70,101,103,144,145,187-201]. More recently, an increasing number of works has employed explicit supercell calculations thus enabling the investigation of local lattice relaxations and ordering effects [66,69,102,121,161,188,194,199,202-205].

Overall, a wide range of alloys has been investigated, mostly fcc Co–Cr–Fe–Mn–Ni base alloys [69,70,101,103,144,145,187,188,194,197,201,204] as well as bcc refractory alloys such as Hf–Nb–Ti–V–Zr base ones [69,102,121,189-193,195,196,199,200,202,203,205]. Few studies dealt with the more rare hcp HEAs, namely HfScTiZr [206] and an Al–Hf–Sc–Ti–Zr alloy [66].

The above-mentioned works mainly focused on the bulk modulus $B$ and elastic constants $C_{ij}$ extracted from $T = 0$ K total energies at different volumes or volume-conserving deformations [81,207,208]. The key quantity needed for that purpose is the total electronic energy of the static lattice at $T = 0$ K, i.e., $E_\alpha(\boldsymbol{\varepsilon}\cdot\mathbf{A}, \{x_i^\alpha\})$ as a function of the strain tensor $\boldsymbol{\varepsilon}$ applied to the matrix of lattice vectors $\mathbf{A}$ (Section 2). For example, the tetragonal shear modulus $C' = (C_{11} - C_{12})/2$ of cubic-lattice systems can be obtained by fitting the energy-deformation data $E_\alpha(\boldsymbol{\varepsilon}\cdot\mathbf{A}, \{x_i^\alpha\}) \equiv E(\delta) = E_0 + 2VC'\delta^2$ resulting from the volume-conserving orthorhombic deformation

$$\boldsymbol{\varepsilon} = \begin{pmatrix} 1+\delta & 0 & 0 \\ 0 & 1-\delta & 0 \\ 0 & 0 & 1/(1-\delta^2) \end{pmatrix}, \tag{32}$$

where $\delta$ is the deformation parameter, which is varied, e.g., between 0 and 0.05 [187,188,194].

Elastic properties computed from such strain deformations correspond to perfect, single crystal quantities. Elastic properties of isotropic polycrystalline systems can be approximated by averages over the single-crystal elastic quantities. For cubic-lattice systems, for example, the polycrystalline bulk modulus $B$ can be simply set equal to that of the single crystal. The polycrystalline shear modulus $G$ may be computed, e.g., via the Hill average $G = (G_V + G_R)/2$, which is the arithmetic average of the Voigt and Reuss bounds [81,209] given as

$$G_V = \frac{C_{11} - C_{12} + 3C_{44}}{5} \tag{33}$$

and

$$G_R = \frac{5(C_{11} - C_{12})C_{44}}{4C_{44} + 3(C_{11} - C_{12})}, \tag{34}$$

respectively. The Young's modulus

$$E = \frac{9BG}{3B + G} \tag{35}$$

and the Poisson's ratio

**Table 5**
Collection of *ab initio* works on chemical long- and short-range order in HEAs/CCAs.

| Year | References | Alloys | Methods |
|---|---|---|---|
| 2013 | Huhn and Widom [135] | MoNbTaW | CE + MC, hybrid MC/MD |
| 2014 | Huhn [136] | MoNbTaW | CE + MC, hybrid MC/MD |
| | Widom et al. [137] | MoNbTaW | Hybrid MC/MD |
| 2015 | Niu et al. [154] | CoCrFeNi | Selected configurations, Cr sublattice ordering |
| | Singh et al. [156] | CuNiZn, AlNbTi, AlCoCrFeNi | Concentration wave |
| | Tamm et al. [157] | CoCrNi, CoCrFeNi | MC |
| | Toda-Caraballo et al. [158] | Mo–Nb–Ta–V–W | CE + MC |
| | Wróbel et al. [159] | Co–Fe–Ni and its binaries | CE + MC, magnetic CE |
| 2016 | Khan et al. [160] | AgAuCu, NiPdPt, AgPdRh, CoCuNi | Concentration wave |
| | Körmann and Sluiter [102] | MoNbTaW | Selected configurations, Debye-Grüneisen model |
| 2017 | Feng et al. [138] | Cr–Mo–Nb–V | Hybrid MC/MD, harmonic phonons |
| | Feng et al. [161] | $(AlSi)_xCoFeNi$ | MC |
| | Fernández-Caballero et al. [162] | MoNbTaVW | CE + MC |
| | Körmann et al. [163] | MoNbTaW | SGPM + MC |
| | Lederer et al. [164] | > 1200 alloys | CE + quasichemical approximation |
| | Nguyen et al. [165] | Al–Co–Fe–Ni–Ti | CE + MC |
| | Ogura et al. [166] | $Al_xCoCrFeNi$ | Selected configurations |
| | Rogal et al. [66] | AlHfScTiZr | Selected configurations, Debye-Grüneisen model |
| | Toda-Caraballo et al. [32] | MoNbTaVW | CE + MC |
| 2018 | Ma et al. [167] | Al–Co–Cr–Fe–Ni | Selected configurations |
| | Schön et al. [168] | Mo–Nb–Ta–V–W | CVM |
| | Singh et al. [169] | Mo–Nb–Ta–W | Concentration wave |
| | Singh et al. [170] | Mo–Ta–Ti–W–Zr | Concentration wave |
| | Singh et al. [171] | $Al_xCoCrFeMn$ | Concentration wave |
| | Wang et al. [121] | Mo–Nb–Ta–V–W | Selected configurations, quasiharmonic phonons |
| | Wu et al. [155] | CoCrCuFeNi | Selected configurations |

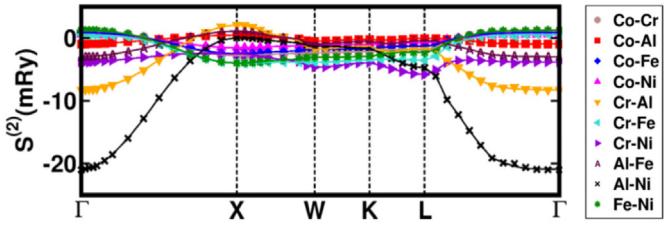


**Fig. 14.** Elements of the chemical stability matrix, $S^{(2)}_{\nu\mu}(\mathbf{k})$, as a function of the wavevector $\mathbf{k}$ for atomic pairs $\nu$ and $\mu$ in disordered fcc AlCoCrFeNi. The peaks in $S^{(2)}_{\nu\mu}(\mathbf{k})$ are related to chemical instabilities. For example, the strongest pair in driving A2 ordering is Cr-Al (maximum at the X point).
Source: Adapted from Ref. [156].

$$\nu = \frac{3B - 2G}{2(3B + G)} \tag{36}$$

can be computed from $B$ and $G$. The ratio of bulk and shear modulus, the $B/G$ or Pugh's ratio [210,211], is often employed to estimate the brittle-ductile transition. A value of $B/G > 1.75$ indicates ductility otherwise the alloy is supposed to be brittle.

Elastic anisotropy of cubic-lattice HEAs and CCAs can be likewise investigated utilizing elastic constants. Several criteria are available such as the Zener ratio $A_Z \equiv C_{44}/C'$, where $A_Z = 1$ indicates an isotropic system [212]. An alternative introduced by Every [213] is to inspect $A_E \equiv (C_{11} - C_{12} - 2_{44})/(C_{11} - C_{44})$, where an isotropic system would have a value of $A_E = 0$. The polycrystalline shear moduli can be also used to measure the elastic anisotropy via $A_{VR} \equiv (G_V - G_R)/(G_V + G_R)$, where the isotropic system exhibits $A_{VR} = 0$.

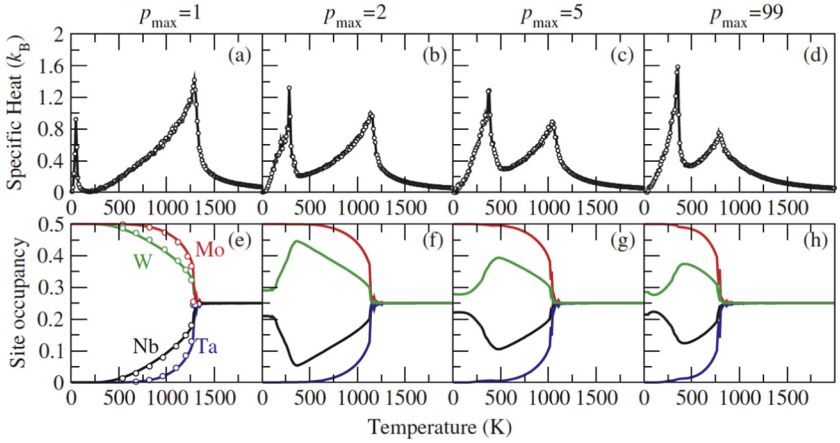


**Fig. 15.** Specific heat capacity (a)–(d) and site occupation (e)–(h) of bcc MoNbTaW when including different numbers of pair interactions ($p_{max}$). White circles in the panel (e) denote the result of the MC simulations obtained in Ref. [136].
Source: Adapted from Ref. [163].

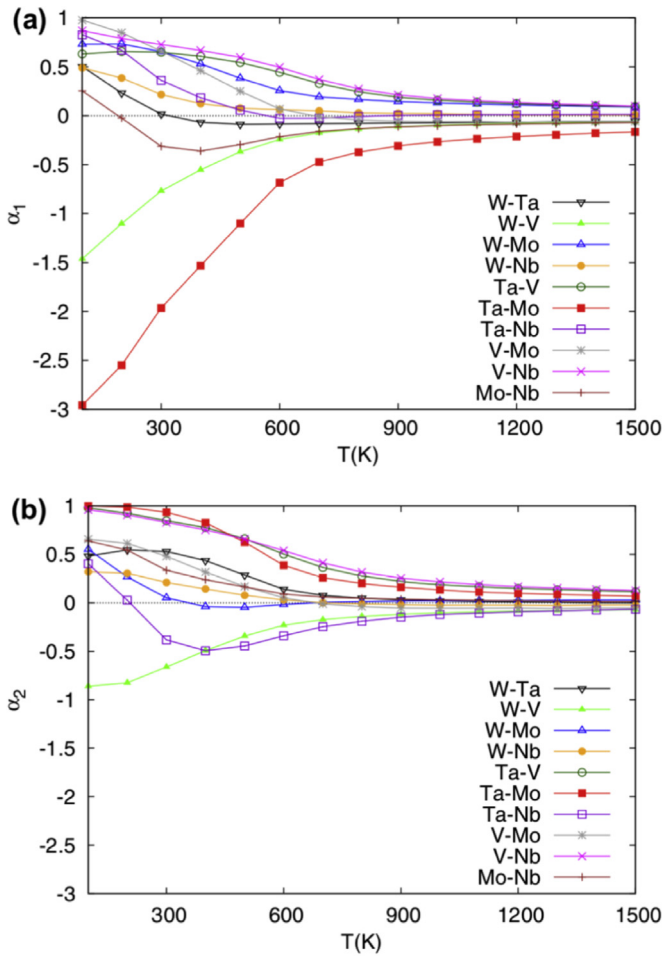


**Fig. 16.** Computed (a) 1NN and (b) 2NN Warren–Cowley SRO parameters for bcc quinary equiatomic MoNbTaVW as a function of temperature.
Source: Taken from Ref. [32].

Zaddach et al. [188] computed elastic constants for fcc CoCrFeNi and CoCrFeMnNi using EMTO-CPA as well as the supercell method employing VASP. The results shown in Fig. 18 indicate deviations between the two methods. The authors reasoned that the observed differences are a consequence of the magnetic treatment. For the EMTO-CPA calculations, the DLM approach was employed to mimic the magnetic disorder whereas the VASP calculations were done employing a ferrimagnetic solution. Later work confirmed that a ferrimagnetic configuration with Cr and Mn spin moments antiferromagnetically aligned to Fe, Co, and Ni spin moments is lower in energy as compared to the fully magnetically disordered solution [101]. It is therefore indeed likely that the discrepancies observed in Fig. 18 are mainly due to the differences in the magnetic treatment. This statement is further supported by a recent comparison [121]. For non-magnetic refractory HEAs, Wang et al. [121] revealed a close agreement between EMTO-CPA and supercell based approaches, indicating that elastic properties are less sensitive to, e.g., local lattice distortions and hence the actual computational treatment.

The explicit impact of local lattice distortions on elastic properties has been investigated recently by Körmann and Sluiter [102], Tian et al. [199], and Zheng et al. [205] for different refractory alloys using supercell calculations. Körmann and Sluiter [102] investigated the impact of lattice distortions on the bulk modulus of bcc NbMoTaW and found negligible changes. Tian et al. [199] found likewise a negligible influence of lattice distortions on the elastic constants of bcc NbTiVZr, MoNbTiZr, and MoNbTiVZr, despite their noticeable impact on the mixing energies (cf. Section 3.2). Similarly, Song et al. [69] reported minor variations in the computed bulk moduli for a set of six bcc HEAs and three fcc HEAs including bcc HfNbTaTiZr. For the latter alloy, Zheng et al. [205] also studied the impact of lattice distortions on elastic constants and found a strong effect. For instance, Zheng et al. [205] reported a decrease of the shear modulus $G$ of about 25% for HfNbTaTiZr if distortions are taken into account.[5] A possible explanation for this decrease is a tendency to dynamical instability that can be expected for this bcc alloy due to a joint effect of Ti, Zr, and Hf all of which are dynamically unstable in the bcc phase [214]. Thus, the impact of local distortions on elastic properties cannot be in general *a priori* neglected but appears to be minor for most of the investigated HEAs and CCAs.

The computational efficiency of EMTO-CPA has given rise to a series of works on elastic properties with a focus on compositional trends [70,101,103,144,145,187-200]. For example, Tian et al. [70] investigated the impact of Al alloying on elastic properties of $Al_xCoCrFeNi$ as shown in Fig. 19. The results reveal different compositional dependences of the elastic constants in the fcc and bcc phase (see also the corresponding phase-stability discussion in Section 3.1). Both dependences are nearly linear (Vegard's-law type dependence), increasing with Al concentration for fcc and decreasing for bcc. More recent high-throughput calculations for elastic properties based on EMTO-CPA were reported in Niu et al. [194]. Fig. 20 shows their computed $B/G$ ratio for 2736 different fcc Co–Cr–Fe–Ni alloys, where the blue regions indicate brittle alloys. Their results demonstrate the computational efficiency of EMTO-CPA and further show that linear compositional trends cannot be always expected. The computed maps can be employed to tune the ductile-brittle transition.

Very recently third-order elastic constants, which provide, e.g., an insight into crystal anharmonicity, were computed based on EMTO-CPA for four bcc refractory HEAs [200]. Fig. 21 shows the reported relation between valence electron concentration and elastic constants. It has been found that the $C_{111}$ elastic constant is largest in magnitude and that it shows the largest dependence on electron concentration, revealing the potential of compositional tuning of anharmonic properties of HEAs and CCAs.

Ideal materials strength can be also computed by applying an elastic strain to the lattice vectors, albeit a strain larger than for elastic constant calculations. The ideal strength is defined as the maximum stress before an alloy in a *perfect* crystal structure becomes dynamically unstable against the applied strain. Dynamical stability is often evaluated utilizing elastic constants via the Born criteria [215]. There are several reports on *ab initio* computed ideal strength for HEAs/CCAs [145,193,195,201]. For example, Li et al. [193] computed the ideal tensile strength under an [001] strain for four refractory HEAs. Fig. 22 shows the results for HfNbZr, HfNbTiZr, NbTiVZr, and HfNbTiVZr. All alloys maintained the ideal BCT structure [Fig. 22(b)] in their simulations except for NbTiVZr, for which a branching towards a symmetrically reduced orthorhombic structure was observed [denoted as NbTiVZr (ort) in Fig. 22(c)]. The authors traced back the origin of the observed trends to the structural energy difference between fcc and bcc. The latter was shown to correlate with the *d*-band filling [193], highlighting that the *d*-band filling is a good descriptor for ideal materials strength.

In order to investigate explicitly the relation between local electronic structure and mechanical properties, Wang et al. [216] employed the cluster + glue-atom model which had been originally proposed to study quasicrystals and bulk metallic glasses [217]. In this approach, the alloy structure is split into a cluster and a glue atom part as sketched

[5] We note slightly different bulk modulus predictions in Song et al. [69] and Zheng et al. [205] which might be caused by different computational settings, in particular the choice of the basis set. Song et al. [69] employed VASP calculations based on the PAW formalism, whereas Zheng et al. [205] employed CP2K calculations based on Gaussian basis set.

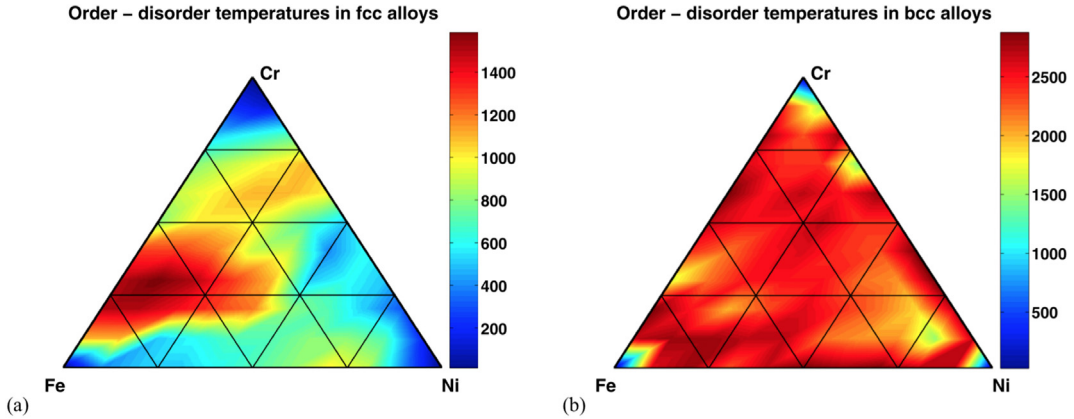


**Fig. 17.** Order-disorder temperatures of fcc (a) and bcc (b) Cr–Fe–Ni alloys computed using Monte Carlo simulations in combination with a magnetic cluster expansion.
Source: Taken from Ref. [159].

in Fig. 23(a). For the bcc structure, the cluster consists of the first and second neighboring shell (6 and 8 atoms), i.e., in total 14 atoms surrounding the glue atoms located at the center and vertex positions. Fig. 23(b) shows the electronic charge density analysis for a number of different clusters and glue atoms. Based on this local bond analysis, Wang et al. [216] revealed the important role of relatively strong electronic bonds between elements from different transition metal groups of the periodic table and relatively weak bonding between elements from the same group for the mechanical performance of refractory HEAs.

Most of the studies on elastic properties have relied on the $T = 0$ K energy surface $E_\alpha(\boldsymbol{\varepsilon}\cdot\mathbf{A}, \{x_i^\alpha\})$ neglecting free energy contributions [Eq. (6)]. A more complete approach is to consider the generalized free energy surface $F^\alpha(T, \boldsymbol{\varepsilon}\cdot\mathbf{A}, \{x_i^\alpha\})$ [cf. Eq. (8)], but corresponding studies are rare. Finite-temperature effects on elastic properties have so far been mainly considered based on the quasiharmonic Debye model (cf. Section 3.3) and have been studied for fcc CoCrFeMnNi [101], bcc refractory alloys [102,103,121] as well as for an hcp Al-base HEA [66]. Most of the works focused on the bulk moduli and in all considered examples, the elastic properties show the typical softening behavior due

**Table 6**
Collection of *ab initio* works on elastic properties for HEAs/CCAs. The symbol $C_{ij}$ in the column "Remarks" indicates that the second-order elastic constant tensor was computed. Note that polycrystalline moduli like bulk modulus, shear modulus, and Poisson ratio can be computed from $C_{ij}$ as described in the main text.

| Year | Reference | Alloys | Method | Remarks |
|---|---|---|---|---|
| 2013 | Tian et al. [70] | $Al_x$CoCrFeNi | EMTO-CPA | $C_{ij}$, shear modulus, impact of crystal structure. |
| | Tian et al. [187] | CoCrFeNi, CoCrCuFeNi$Ti_x$ | EMTO-CPA, EMTO-SC | $C_{ij}$, shear modulus, CPA vs. 4-atom SC w/o relaxations. |
| | Zaddach et al. [188] | CoCrFeNi, CoCrFeMnNi, variations | EMTO-CPA, VASP-SQS | $C_{ij}$, SQS vs. CPA, discussion on magnetism. |
| 2014 | Fazakas et al. [189] | HfNbTiVZr, CrHfNbTiZr | EMTO-CPA | $C_{ij}$, shear modulus. |
| | Tian et al. [190] | NbTiVZr, MoNbTiVZr | EMTO-CPA | $C_{ij}$, shear modulus. |
| 2015 | Cao et al. [191] | $Al_x$MoNbTiV | EMTO-CPA | $C_{ij}$, shear modulus. |
| | Li et al. [192] | $Al_xHf_{1-x}$NbTaTiZr | EMTO-CPA | $C_{ij}$, shear modulus. |
| | Li et al. [193] | NbTiVZr, HfNbTiZr, HfNbTiVZr | EMTO-CPA | $C_{ij}$, shear modulus, ideal tensile strength, CPA vs. VCA. |
| | Ma et al. [101] | CoCrFeMnNi | EMTO-CPA | Bulk modulus, Impact of $T$ (Debye-Gr). |
| 2016 | Körmann and Sluiter [102] | MoNbTaW | VASP-SQS | Bulk modulus, impact of $T$ (Debye-Gr), lattice distortions and ordering. |
| | Niu et al. [194] | CoCrFeNi-base alloys | EMTO-CPA, VASP-SQS | $C_{ij}$, shear modulus, SQS vs. CPA, over 2700 alloys. |
| | Rogal et al. [206] | HfScTiZr | VASP-SC | $C_{ij}$. |
| | Tian et al. [195] | MoNbTiV | EMTO-CPA, CASTEP-VCA | $C_{ij}$, shear modulus, ideal tensile and shear strength. |
| 2017 | Feng et al. [161] | $(AlSi)_x$CoFeNi | VASP-SC + MC | $C_{ij}$, shear modulus, impact of chemical SRO. |
| | Ge et al. [196] | AlMoTiV, CrMoTiV, MoNbTiV | EMTO-CPA | $C_{ij}$, shear modulus. |
| | Huang et al. [197] | CoCrFeGaNi | EMTO-CPA | $C_{ij}$, shear modulus. |
| | Huang et al. [144] | CoCuFeNi, CoCuFeNiX(X = V, Cr, Mn) | EMTO-CPA | $C_{ij}$, shear modulus. |
| | Rogal et al. [66] | $Al_{15}Hf_{25}Sc_{10}Ti_{25}Zr_{25}$ | VASP-SQS | Bulk modulus, impact of $T$ (Debye-Gr) and ordering. |
| | Song et al. [69] | Al–Hf–Nb–Ta–Ti–Zr, Co–Cr–Fe–Mn–Ni | VASP-SQS | Bulk modulus, lattice distortions. |
| | Tian et al. [198] | CrMoWX (X = Mn, Co, Ni) | EMTO-CPA | $C_{ij}$, shear modulus. |
| | Tian et al. [199] | NbTiVZr, MoNbTiZr, MoNbTiVZr | EMTO-CPA VASP-SQS | $C_{ij}$, shear modulus, SQS vs. CPA, lattice distortions. |
| | Yao et al. [203] | MoNbTaTiV | VASP-SQS | $C_{ij}$, shear modulus. |
| 2018 | Feng and Widom [202] | NbTiVZr, CrMoNbV, HfNbTaZr, MoNbTaW | VASP-MC/MD | $C_{ij}$, shear modulus, lattice distortions. |
| | Ge et al. [103] | CoCrFeMnNi | EMTO-CPA | $T$-dependent $C_{ij}$ (Debye-Gr), shear modulus. |
| | Huang et al. [145] | $Al_x$CoCrFeMn | EMTO-CPA | $C_{ij}$, shear modulus, ideal tensile strength. |
| | Li [200] | MoNbTiV, MoNbTaW, NbTiVZr, HfNbTiVZr | EMTO-CPA | Third-order elastic constants. |
| | Li et al. [201] | CoCrFeMnNi & subsystems | EMTO-CPA | $C_{ij}$, shear modulus, ideal shear strength. |
| | Wang et al. [121] | Nb–Mo–Ta–V–W | VASP-SQS | Bulk modulus, impact of ordering, Debye temperature. |
| | Ye et al. [204] | Co–Cr–Fe–Mn–Ni | VASP-SQS | $C_{ij}$. |
| | Zheng et al. [205] | 5- and 6-equi-comp. Al–Hf–Mo–Nb–Ta–Ti–V–Zr | CP2K-SC | $C_{ij}$, shear modulus, lattice distortions. |

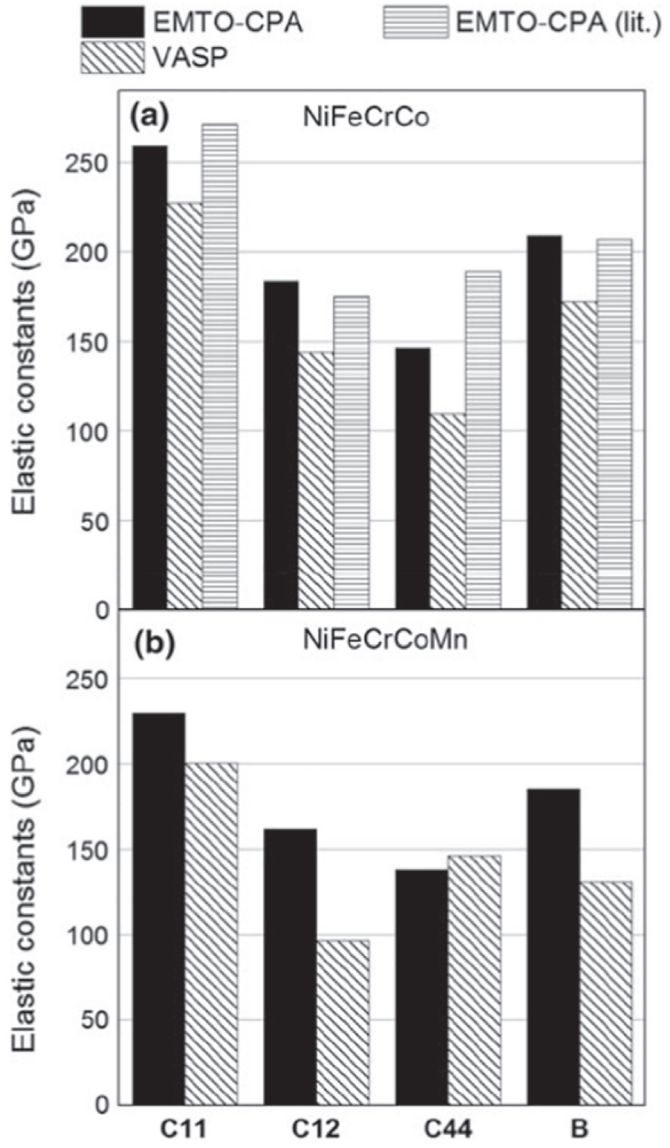


**Fig. 18.** Elastic constants for fcc (a) CoCrFeNi and (b) CoCrFeMnNi based on EMTO-CPA calculations as well as VASP simulations employing the supercell approach. The results for fcc CoCrFeNi indicated by "lit." are from Ref. [187]. Source: Taken from Ref. [188].

to the thermal expansion [66,101-103,121].

Another implicit approximation in the majority of the performed studies has been the assumption of full chemical disorder. Studies on the impact of partial chemical ordering or short-range order on elastic properties are so far rare. The impact of B2-ordering in bcc MoNbTaW was investigated by Körmann and Sluiter [102], and the bulk modulus was found to be almost unaffected by the ordering in this alloy. The impact of SRO on elastic properties in $(AlSi)_x$CoFeNi HEAs was investigated by Feng et al. [161]. For this purpose, they employed a combined *ab initio* Monte Carlo approach to equilibrate the atomic positions at ambient temperature. They equilibrated the atomic positions at 300 K by swapping atomic positions in the *ab initio* calculations following a Metropolis algorithm. The deduced SRO containing supercells revealed a slight increase of the elastic moduli for all considered compositions.

### 4.2. Solid Solution Strengthening — Local Lattice Distortions

Solid solution strengthening (SSS) is one of the key strengthening mechanisms in solid solutions and thus crucial for HEAs and CCAs. The basic underlying mechanism of SSS is resistance to dislocation mobility resulting from local disturbances of the crystal lattice making plastic deformation more difficult. In the picture of dilute solutes embedded in a solvent lattice, the dislocation mobility depends on the energetics of the elastic interaction of a dislocation with single, separated solute atoms. For binaries, traditional models have been developed based on a dominant principal element and dislocations moving through a solvent lattice (see, e.g., Section 4.1 in Ref. [33] and references therein). This picture is limited in HEAs and CCAs where no clear distinction between solvent and solute atoms can be made [33,158,218,219]. Recently generalized SSS models have been proposed for random solid solutions [158,218,219]. Key input parameters for these models are the averaged misfit volume, $\Delta\overline{V}_n$, of a solute $n$ and its standard deviation, $\sigma_{\Delta V_n}$, when different local chemical environments are considered [218,219]. From the viewpoint of *ab initio* investigations, the local lattice distortions — one of the originally proposed core effects of HEAs — are readily accessible with supercell calculations by, e.g., evaluating the atomic displacements from the ideal sites or the distribution of bond lengths. A comprehensive list of previous *ab initio* based investigations of local distortions is given in Table 7.

Oh et al. [223] studied local lattice distortions for fcc CoCrFeMnNi with a focus on the element-resolved dependence of bond lengths on the local chemical environment. For this purpose, Oh et al. [223] employed the supercell (SQS) approach [see sketch in Fig. 24(a)] with fully relaxed internal atomic positions $\{\mathbf{R}_I\}$. The bond lengths

$$b_{IJ} \equiv |\mathbf{R}_I - \mathbf{R}_J| \tag{37}$$

were defined between each site $I$ and each of its nearest-neighbors located at site $J$, and the set $\{b^{\mathrm{A}}\} \equiv \{b_{IJ} | I \in S^{\mathrm{A}}\}$ was referred to as the bond distribution for an element A, where $S^{\mathrm{A}}$ is the set of the indices for the sites occupied by A. The average element-resolved bond lengths $\overline{b}^{\mathrm{A}}$ were then obtained based on several supercell calculations and were found to be in good agreement with experimental data from extended X-ray absorption fine structure (EXAFS) measurements conducted in the same study [223]. An important finding in Ref. [223] was that the atomic element-resolved bond lengths do not only deviate from the overall mean value of the alloy, but that the bond fluctuations (standard deviation) $\sigma_{b^{\mathrm{A}}}$ due to different local chemical environments can be significant. This is exemplified in Fig. 24(b) for the local bond distortions of Mn in the CoCrFeMnNi HEA. The results thus suggest that a part of the strength of the materials may be due to local lattice distortions as a consequence of the different local chemical environments.

Song et al. [69] investigated local lattice distortions based on the supercell approach for a more extensive set of in total nine alloys, including a set of bcc refractory HEAs. Their results revealed that local distortions are much more significant for the refractory bcc alloys as compared to the considered fcc ones. This is likely due to the fact that the considered bcc alloys in Song et al. [69] reveal mostly larger atomic size mismatch as the fcc ones.

An alternative to quantify local lattice distortions is to inspect the deviation of the relaxed atomic positions $\{\mathbf{R}_I\}$ from the ideal atomic sites $\{\mathbf{R}_I^{\mathrm{ideal}}\}$ of the underlying crystal structure. Based on this, Okamoto et al. [224] analyzed the mean squared atomic displacements (MSAD) for each constituent element A,

$$\mathrm{MSAD}_{\mathrm{A}} = \frac{1}{|S^{\mathrm{A}}|} \sum_{I \in S^{\mathrm{A}}} (\mathbf{R}_I - \mathbf{R}_I^{\mathrm{ideal}})^2, \tag{38}$$

for different fcc HEAs based on the supercell approach. Fig. 25(a) shows their computed MSAD values for the principal elements in fcc CoCrFeMnNi revealing a clear dependence of the MSAD values on the individual chemical elements. Okamoto et al. [224] further suggested a relation between the *ab initio* computed MSAD values and experimentally derived yield strengths $\sigma_{\mathrm{YS}}$ (extrapolated to 0 K). For this relation, a number of fcc Co–Cr–Fe–Mn–Ni suballoys was considered. Okamoto et al. [224] empirically found that $\sigma_{\mathrm{YS}}$ normalized by the shear modulus

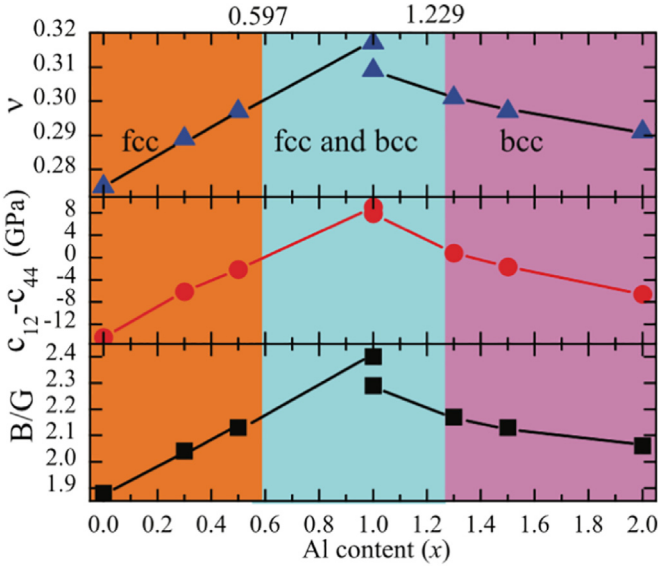


**Fig. 19.** Impact of crystal structures on the computed Poisson's ratio (upper panel), Cauchy pressure (middle panel), and Pugh's ratio (lower panel) for $Al_xCoCrFeNi$ alloys as a function of Al fraction. The theoretically predicted fcc, bcc and dual-phase bcc-fcc regions are highlighted in different colors. (For interpretation of the references to color in this figure legend, the reader is referred to the web version of this article.)
Source: Taken from Ref. [70].

scales linearly with the square root of the MSAD values averaged over the constituent elements as

$$\sigma_{YS}/G = k\cdot(\text{Averaged MSAD})^{1/2}, \quad (39)$$

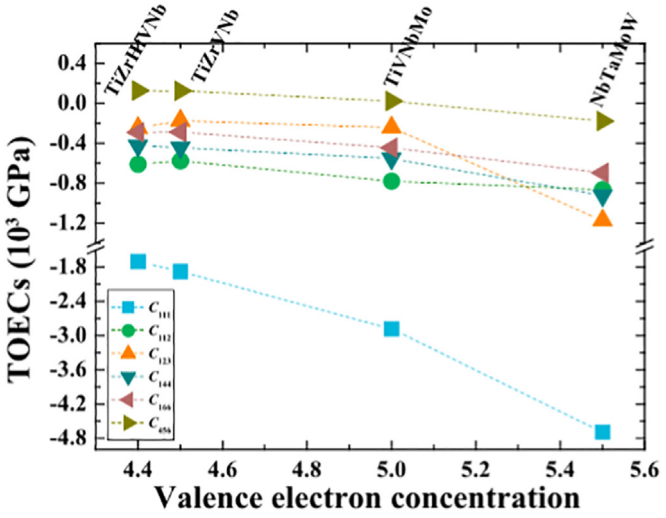


**Fig. 21.** Computed third-order elastic constants (TOECs) for four bcc refractory HEAs and their relation to the valence electron concentration.
Source: Taken from Ref. [200].

where $G$ denotes the shear modulus and $k$ a fitting parameter. Fig. 25(b) shows the application of Eq. (39) revealing an almost linear dependence. Note that the experimental shear modulus $G$ employed in Eq. (39) could be alternatively derived from *ab initio* calculations of elastic constants [cf. Eqs. (33) and (34)] as described in Section 4.1.

At elevated temperatures, the atoms are subject to thermal excitations which further broadens the distribution of atomic bond lengths $b_{IJ}$ from Eq. (37). Assuming a local harmonic potential for each atom, the atoms vibrate around their mean positions and hence the bond length

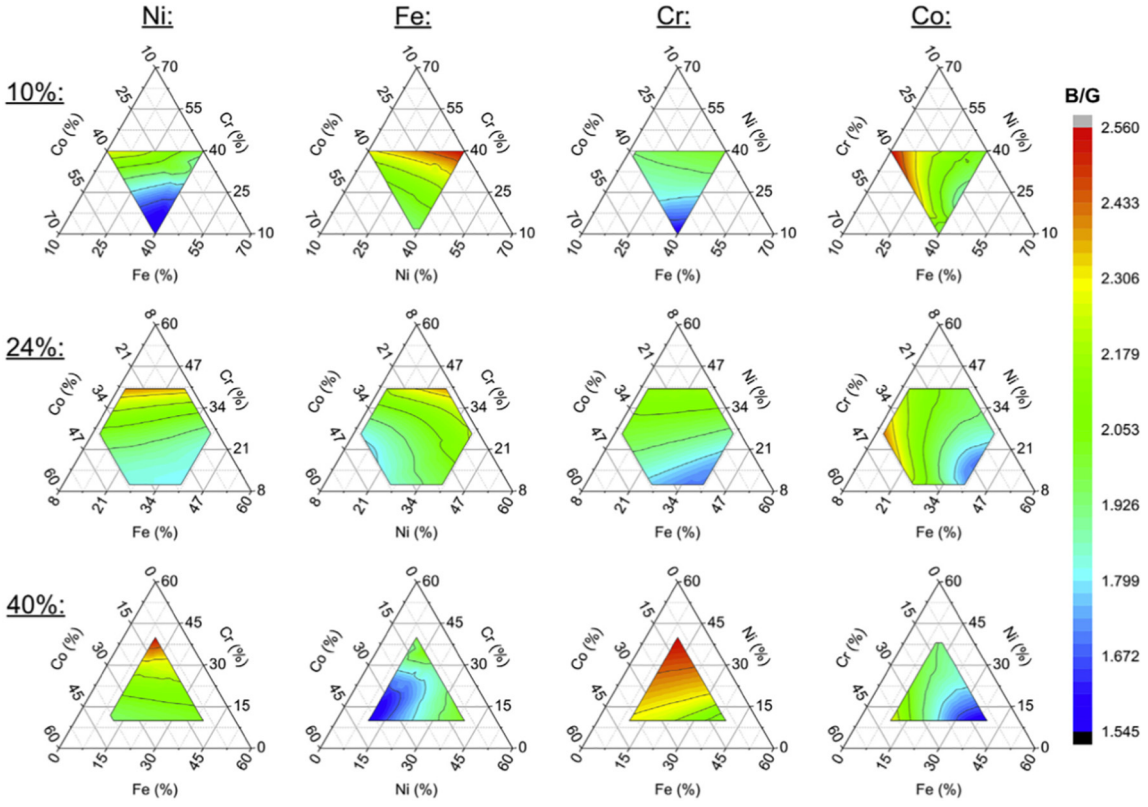


**Fig. 20.** Ratio of bulk modulus and shear modulus, $B/G$ ratio, for fcc Co–Cr–Fe–Ni alloys based on EMTO-CPA calculations. (For interpretation of the references to color in this figure, the reader is referred to the web version of this article.)
Source: Taken from Ref. [194].

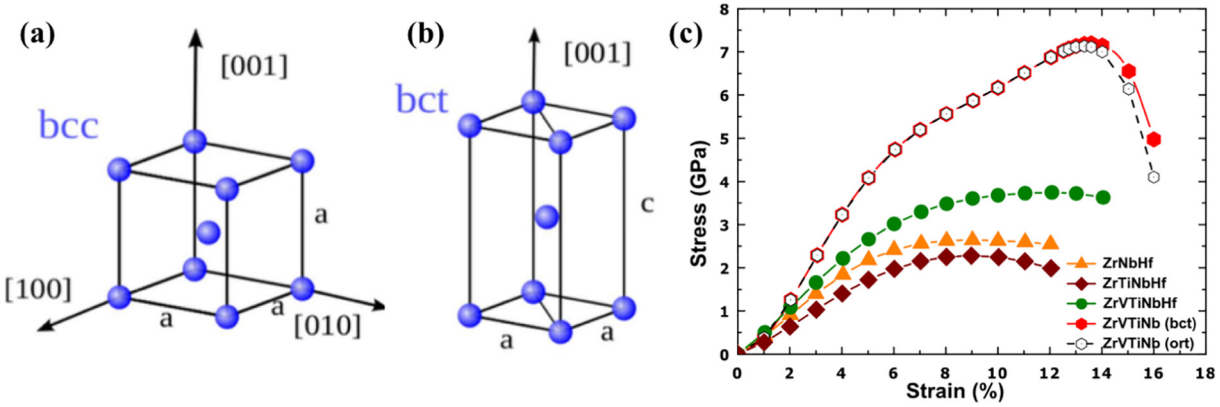


**Fig. 22.** Structures (a) without and (b) with tensile strain along the [001] direction. (c) Computed relation between the tensile stress and the applied tensile strain for four refractory bcc HEAs/CCAs. A branching is observed for bcc NbTiVZr from the tetragonal to the orthorhombic deformation path at ~ 12.7% strain.
Source: Adapted from Ref. [193].

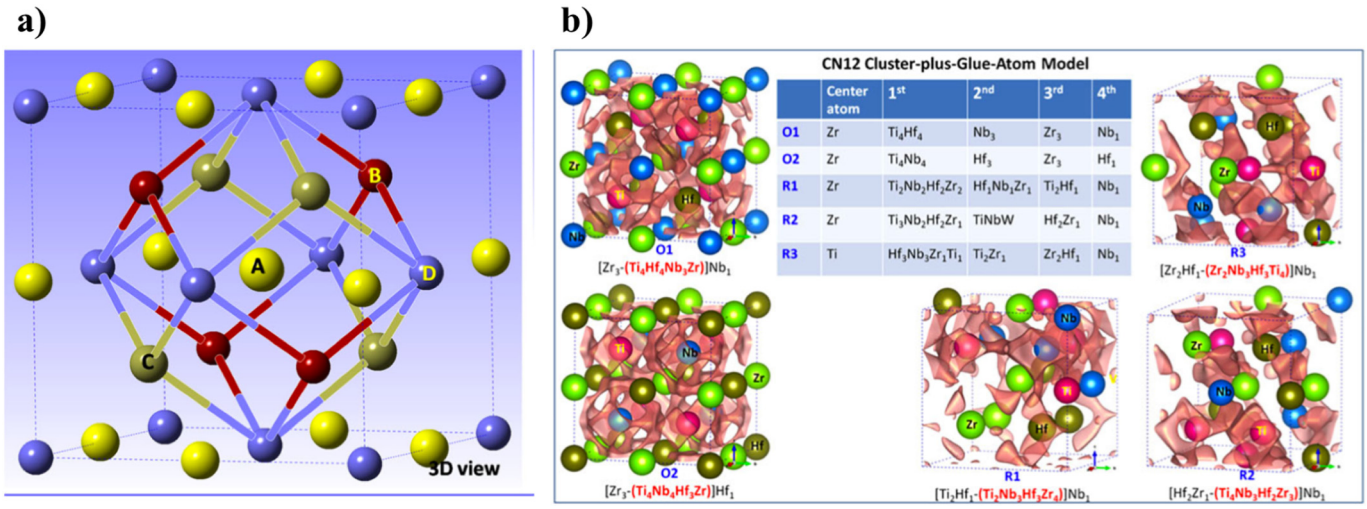


**Fig. 23.** Wang et al. [216] investigated the correlation between strength and local electronic arrangement for refractory bcc HEAs. The figure exemplifies the application of the cluster + glue-atom model to bcc HfNbTiZr. (a) Supercell view of the 14-coordinated cluster with its glue atoms (golden atoms at edge centers and blue atoms in the vertex positions). (b) Bonding-charge-density isosurface ($\delta\rho$ = 0.008 $e^{-1}$Å) of configurational transformations of different configurations for the cluster + glue-atom model. The inserted table presents the first four nearest neighbors of the center atom and the atoms in the cluster are written in red letters. (For interpretation of the references to color in this figure legend, the reader is referred to the web version of this article.)
Source: Adapted from Ref. [216].

broadening $\sigma_{b^A}$ is modified by an additional thermal broadening $\sigma_{\text{thermal}^A}$. If we assume that both contributions, i.e., the static local distortions as well as the temperature and time-dependent fluctuations due to thermal vibrations are independent from each other and random, the standard deviation for the total bond fluctuations, $\sigma_{\text{tot}^A}$, can be written as

$$\sigma^2_{\text{tot}^A} = \sigma^2_{\text{thermal}^A} + \sigma^2_{b^A}, \tag{40}$$

where $\sigma_{\text{thermal}^A}$ denotes the standard deviation (broadening) due to lattice vibrations for the element A. Note that experiments are typically carried out at ambient temperatures and hence sample the total broadening $\sigma_{\text{tot}^A}$.

An elegant way to include both static distortions as well as lattice vibrations is to employ *ab initio* molecular dynamics (AIMD) simulations and to evaluate the pair distribution function (PDF) (see Fig. 13) which is sometimes also called partial radial distribution function [135,137,139,140,184,202,216,220,222]. The PDF describes how the element density varies as a function of distance from a given reference particle. Employing AIMD calculations at finite $T$ takes thermal excitations into account and thus includes thermally induced variations of the bond lengths. A separation of the chemical environment induced intrinsic contributions, $\sigma_b$, and thermal excitation induced contributions, $\sigma_{\text{thermal}}$, to the overall lattice distortions requires, however, additional static zero temperature calculations.

We finally note current developments enabling more efficient computations of interatomic distances as compared to the supercell approach. For example, Toda-Caraballo et al. [158] derived a model to predict interatomic distances in HEAs/CCAs based on lattice constants and bulk moduli of the constituent elements, i.e., parameters which are accessible via routine *ab initio* calculations. The proposed model revealed a reasonable predictability when compared to explicit supercell calculations [158] exemplifying a promising route for further reducing the required amount of computationally costly explicit supercell *ab initio* calculations.

### 4.3. *Twinning and Transformation-induced Plasticity — The Stacking Fault Energy*

One of the most important quantities linking macroscopic mechanical properties and quantities accessible via *ab initio* calculations is the stacking fault energy (SFE). The SFE is the energy carried by the interruption of the normal atomic stacking sequence as exemplified for

**Table 7**
Collection of *ab initio* works focusing on local lattice distortions and the related impact on materials properties in HEAs. Note that works focusing on chemical ordering and elastic properties are also collected in Tables 5 and 6, respectively.

| Year | Reference | Alloys | Methods | Remarks |
|---|---|---|---|---|
| 2013 | Gao and Alman [220] | $Al_{1.3}$CoCrCuFeNi, HfNbTaTiZr, CuNiPPdPt | VASP-MD | PDF at finite *T*. |
| | Huhn and Widom [135] | MoNbTaW | VASP-MC/MD | PDF at finite *T*. |
| | Zaddach et al. [188] | Co–Cr–Fe–Mn–Ni | VASP-SQS | Impact on elastic constants. |
| 2014 | Widom et al. [137] | MoNbTaW | VASP-MC/MD | PDF at finite *T*. |
| 2015 | Egami et al. [221] | CoCrNi, CoCrFeNi | Supercell | Local atomic volume, atomic-level stresses. |
| | Santodonato et al. [139] | $Al_{1.3}$CoCrCuFeNi (liquid) | VASP-MD | PDF at finite *T*. |
| 2016 | Gao et al. [222] | HfNbTaTiVZr | VASP-MD | PDF at finite *T*. |
| | Körmann and Sluiter [102] | MoNbTaW | VASP-SQS | Impact on stability and bulk modulus. |
| | Niu et al. [194] | Co–Cr–Fe–Ni | VASP-SQS | Impact on elastic constants. |
| | Oh et al. [223] | CoCrFeMnNi | VASP-SQS | Element resolved displacements, relation to SSS. |
| | Okamoto et al. [224] | CoCrFeMnNi and equiatomic subsystems | VASP-SQS | Mean displacements, relation to SSS. |
| | Widom [184] | CrMoNbV, NbTiVZr | VASP-MC/MD | PDF at finite *T*. |
| 2017 | Song et al. [69] | HfNbTaTiZr, MoNbTaVW, AlNbTiV, CoCrFeMnNi, and variations | VASP-SQS | Element resolved displacements, impact on stability and bulk modulus. |
| | Tian et al. [199] | NbTiVZr, MoNbTiZr, MoNbTiVZr | VASP-SQS | Impact on elastic constants. |
| | Wang et al. [216] | MoNbTaW, MoNbVW, MoTaVW, HfNbTiZr, and others | VASP-SC/MD | Quantification and relation to SRO. |
| 2018 | Feng et al. [140] | $Al_{1.5}$CrFeMnTi (liquid) | VASP-MD | PDF at finite *T*. |
| | Feng and Widom [202] | NbTiVZr, CrMoNbV, HfNbTaZr, MoNbTaW | VASP-MC/MD | PDF at finite *T*, mean displacements. |
| | Ye et al. [204] | Co–Cr–Fe–Mn–Ni | VASP-SQS | Relation to local strain and SSS. |
| | Zheng et al. [205] | 5- and 6-equi-comp. Al–Hf–Mo–Nb–Ta–Ti–V–Zr | CP2K-SC | Impact on elastic constants. |

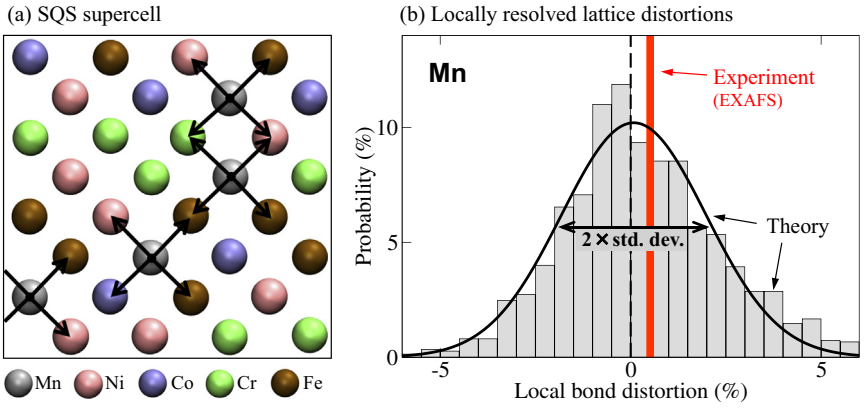


**Fig. 24.** (a) Projection of a SQS supercell model of fcc CoCrFeMnNi onto the (100) plane. The black arrows indicate the nearest-neighbor bonds for Mn atoms that are used to extract the distribution of the local bond distortions as shown in (b). In (b), the first-principles computed lattice distortion histogram of Mn-bonds in CoCrFeMnNi is based on 1500 evaluated Mn-bonds. The experimentally-measured averaged distortion is indicated by the red solid line. Although the mean distortion is rather small (< 0.5%), the range of local distortions — indicated by the standard deviation — is significant (≈ 2%), as indicated in (b). (For interpretation of the references to color in this figure legend, the reader is referred to the web version of this article.)
Source: Taken from Ref. [223].

the fcc structure in Fig. 26. It is known that the SFE determines whether a material reveals transformation induced plasticity (TRIP) or twinning induced plasticity (TWIP) [225,226]. Furthermore, a low SFE is known to suppress dislocation climb and cross-slip [227], thereby modifying dislocation gliding and possibly decreasing dislocation mobility. Table 8 summarizes previous *ab initio* studies on the SFE for HEAs/CCAs [106,188,228-235].

The (intrinsic) SFE, $\gamma_{SF}$, for the fcc structure is defined as

$$\gamma_{SF} = \frac{E_{SF} - E_{fcc}}{A_{int}}, \tag{41}$$

where $E_{SF}$ and $E_{fcc}$ represent the energies of the fcc structure with (Fig. 26 right panel) and without (left panel) a stacking fault, respectively, and $A^{int}$ denotes the interface area over which the stacking fault extends in the (111) plane. An *ab initio* SFE can be thus computed using explicit supercell calculations with and without a stacking fault. It is also possible to approximate $\gamma_{SF}$ by using perfect bulk calculations only. The schematic in Fig. 26 indicates that the stacking fault can be interpreted as a local hcp stacking sequence embedded in an fcc bulk structure. This suggests that the SFE is related to an fcc-hcp energy difference. Formally, the relevant equations can be derived based on the axial interaction model [236]. Specifically, the SFE can be approximated by considering the interactions of the (111) layers up to the nearest neighbor layers as

$$\gamma_{SF} \approx \frac{2(E_{hcp} - E_{fcc})}{A_{int}} \tag{42}$$

or up to the next-nearest neighbor layers as

$$\gamma_{SF} \approx \frac{E_{hcp} + 2E_{dhcp} - 3E_{fcc}}{A_{int}}, \tag{43}$$

where $E_{hcp}$ and $E_{dhcp}$ denote the energies of the hcp and dhcp structures, respectively. The approach based on Eq. (42) is sometimes called the axial-nearest-neighbor-Ising (ANNI) model and the one based on Eq. (43) the axial-next-nearest-neighbor-Ising (ANNNI) model. The notation of "first order ANNNI" for Eq. (42) and "second order ANNNI" for Eq. (43) appears to us to be somewhat more frequent. In any case, note that a full treatment considering finite-temperature excitations requires to replace the energies in Eqs. (41)–(43) by the respective free energies including the relevant contributions.

Both CPA and supercell based approaches can be applied to represent chemical disorder and to compute the explicit SFE according to Eq. (41) as well as the approximate SFEs according to Eqs. (42) and (43). The main challenges in calculating SFEs are: (i) small changes on

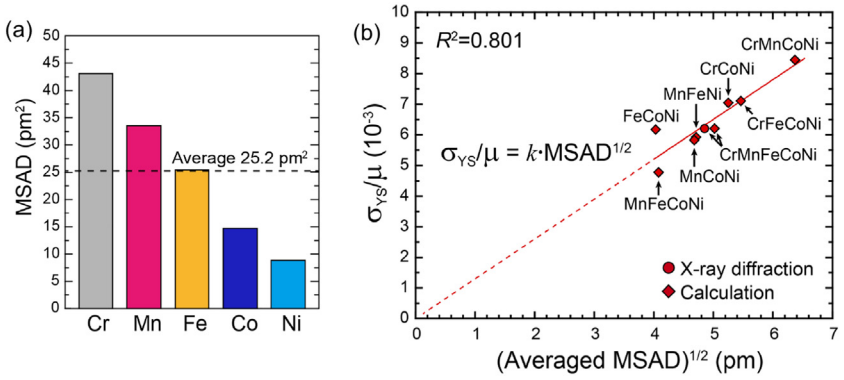


**Fig. 25.** (a) Computed MSAD values for the chemical elements in the CoCrFeMnNi alloy. (b) Correlation between 0 K yield strength (normalized by the shear modulus) and local lattice distortions quantified by the average MSAD values over the chemical elements for various 3*d* fcc HEAs, revealing a linear relation.
Source: Reproduced from Ref. [224] with the permission of AIP Publishing.

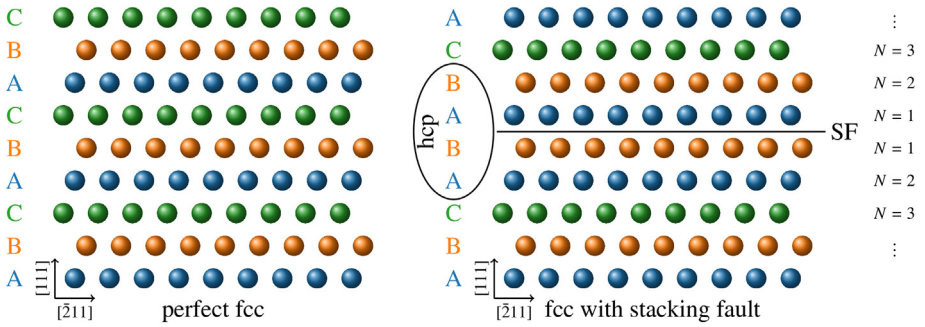


**Fig. 26.** Sketch of a perfect fcc crystal structure (left) and one with a stacking fault (SF; right). Different stacking sequences are represented by different colors. The highlighted ABAB order around the stacking fault corresponds to a local hcp sequence. This suggests that the SFE can be approximated by an fcc–hcp energy difference [Eq. (41)]. Formally, the axial Ising model can be used to derive the approximate relation. (For interpretation of the references to color in this figure legend, the reader is referred to the web version of this article.)

the order of a few ~mJ/m$^2$ (which typically translate into a few meV/atom) can be decisive for the dominant deformation mechanism (TRIP vs. TWIP) [225,226] and (ii) SFEs can be sensitive to thermal excitations, i.e., the free energy versions of Eqs. (41)– (43) can become important [106,228]. A particular challenge for HEAs and CCAs that can be addressed only with explicit SFE calculations is: (iii) the stacking fault can locally induce chemical SRO or element-specific segregation modifying thereby the SFE [237,238]. Local lattice relaxations induced by the stacking fault can likewise only be studied with explicit SFE calculations.

Zaddach et al. [188] conducted one of the first *ab initio* based SFE studies for HEAs, focusing on CoCrFeMnNi and its subsystems with the aim of designing low-SFE alloys. They did not actually apply any of the Eqs. (41)–(43) but rather examined the SFE of these alloys based on an empirical relation using experimental stacking fault probabilities and *ab initio* derived elastic constants, which were determined using the EMTO-CPA or the VASP-SQS approach at $T = 0$ K (cf. Section 4.1). They showed how the SFE can be tuned by varying composition [reproduced in Fig. 27(a)] and found that $Co_{20}Cr_{26}Fe_{20}Mn_{20}Ni_{14}$ [denoted as the "Best HEA" in Fig. 27(b)] shows an even lower SFE than the equiatomic CoCrFeMnNi alloy and other known low-SFE alloys [Fig. 27(b)]. The work of Zaddach et al. [188] highlights the material-design potential inherent to *ab initio* calculations and the alloy design possibilities inherent to the compositional degree of freedom of HEAs. However, in their study, besides using a semi-empirical approach to obtain the SFEs, also thermal excitations (i.e., lattice vibrations, magnetic as well as electronic excitations) were not taken into account.

An explicit SFE [Eq. (41)] including the impact of finite-temperature magnetic excitations was first evaluated by Huang et al. [228] for the CoCrFeMnNi alloy. They used the EMTO-CPA approach to model the chemical disorder. To separate the periodic stacking faults from each other they extended the respective dimension of their simulation cell. The thermal expansion was taken into account by employing the experimental lattice constant at a given temperature. We note that the SFE of fcc CoCrFeMnNi is negative at the theoretical $T = 0$ K lattice constant as discussed below on Fig. 29 and in Section 4.4 on Fig. 30 (see also Refs. [106,108]). As visible by comparing Fig. 28(b) and (c), the change in the difference of the magnetic moments with temperature clearly correlates with the temperature dependence of the SFE. Huang et al. [228] also found that the local magnetic moments around the stacking fault substantially depend on the distance from the stacking fault [see Fig. 28(a)]. It should be emphasized that such properties originating from the local electronic environment around a stacking fault are not accessible via the first or second order ANNNI model, and the results of Huang et al. [228] clearly highlight the advantage of employing an explicit stacking fault supercell model for the *ab initio* simulations.

The unstable SFE, i.e., the energy barrier between the structures with and without a stacking fault, also provides important insights on the deformation mechanisms of HEAs and CCAs and was computed by Patriarca et al. [229][6], Beyramali Kivy and Asle Zaeem [230], Zhang et al. [232], Zhao et al. [106], Alkan et al. [233], Huang et al. [234], and Niu et al. [235] using explicit supercell calculations with and without a stacking fault. For example, Beyramali Kivy and Asle Zaeem [230] investigated the intrinsic and the unstable SFE of CoCrFeNi-based HEAs/CCAs using supercell models in which chemical elements were randomly distributed on the fcc atomic sites. They employed a 108-atom supercell consisting of nine fcc (111) layers and performed non-spin-polarized calculations. One result was that the addition of Mn and Cu reduces both the intrinsic and the unstable SFEs of CoCrFeNi. We stress, however, that spin polarization and thermal excitations, which were not included in that study, substantially affect the energies of HEAs/CCAs, as described in Section 3 [101], and hence also affect the SFEs.

The impact of lattice vibrations on SFEs was analyzed by Zhao et al. [106]. They utilized the harmonic approximation in combination with the finite-displacement method and inspected ten systems ranging from pure Ni up to five-component HEAs including the CoCrFeMnNi alloy. All calculations were performed with VASP and employing the

[6] Detailed computational conditions such as the number of atoms in the supercell models were not given in Ref. [229].

**Table 8**
Collection of *ab initio* works on stacking fault energies (SFEs) for HEAs/CCAs. SF stands for "stacking fault". NM indicates that the SFE calculations are done under the non-magnetic condition. Unless remarked, the calculations are done without including any thermal excitations.

| Year | Reference | Alloys | Method | SFE method | Remarks |
|---|---|---|---|---|---|
| 2013 | Zaddach et al. [188] | FeNi, CrFeNi, CoCrFeNi, CoCrFeMnNi, and variations | EMTO-CPA VASP-SQS | *Ab initio* elastic constants + experimental SF probabilities | |
| 2015 | Huang et al. [228] | CoCrFeMnNi | EMTO-CPA | Explicit SF | Magnetic excitations included, lattice excitations indirectly via experimental lattice constant. |
| 2016 | Patriarca et al. [229] | CoCrFeMnNi | VASP-SQS | Explicit SF | Unstable SFE, Computational details not provided. |
| 2017 | Beyramali Kivy and Asle Zaeem [230] | CoCrFeNi + additions of Cu,Mn,Al,Ti,Mo | VASP + random supercell | Explicit SF | Unstable SFE, NM |
| | Zhang et al. [231] | CoCrNi, CoCrFeNi | VASP-SQS | Explicit SF | NM |
| | Zhang et al. [232] | CoCrNi | VASP + random supercell | Explicit SF, ANNNI | Unstable SFE, NM |
| | Zhao et al. [106] | CoCrFeMnNi, CoCrFeNiPd, and equiatomic subsystems | VASP-SQS | Explicit SF, ANNNI | Unstable SFE, Phonon calculations. |
| 2018 | Alkan et al. [233] | CoCrFeMnNi | VASP-SQS | Explicit SF | Unstable SFE, Relation to strain hardening. |
| | Huang et al. [234] | CoCrNi, CoCrMnNi, CoCrFeNi, CoCrFeMnNi | EMTO-CPA | Explicit SF | Unstable SFE, Relation to critical resolves shear stress. |
| | Niu et al. [235] | CoCrNi, CoCrFeMnNi | VASP-SQS | Explicit SF | Unstable SFE, Impact of magnetism, thermal excitations. |

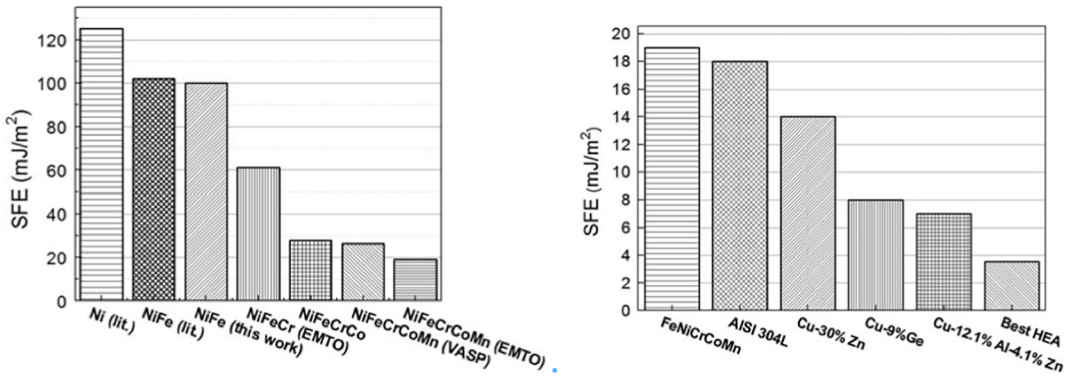


**Fig. 27.** (a) Variation of the SFE when going from pure Ni towards the 5-component CoCrFeMnNi alloy. (b) Comparison of the SFE for the CoCrFeMnNi alloy, conventional alloys, and $Co_{20}Cr_{26}Fe_{20}Mn_{20}Ni_{14}$ denoted as "Best HEA".
Source: Taken from Ref. [188].

explicit stacking fault approach as well as the first and second order ANNNI model. Fig. 29(a) shows the variation of the SFE for the ten investigated alloys and indicates again the large compositional freedom to tune SFEs. Zhao et al. [106] further verified the performance of the first and second order ANNNI models in comparison with the supercell approach [Fig. 29(a)]. Fig. 29(b)–(g) further reveal the temperature dependent free energy contributions to the hcp-fcc phase stability and SFE [within the first order ANNNI model, Eq. (42)] for two alloys, CoCrNi and CoFeNi. The two examples demonstrate that the vibrational contribution to the SFE can be significant and can even induce a sign-change in the phase stability (for CoCrNi at around ambient temperatures). For this example, the change of SFE due to thermal excitations can amount up to 60 $mJ/m^2$. However, if Cr is replaced with Fe, the situation for the CoFeNi alloy is now completely reversed compared to CoCrNi; the SFE now decreases with temperature and moreover the variation is much smaller and amounts to less than 10 $mJ/m^2$. The examples highlight that the neglect of lattice excitations can result in quantitatively and qualitatively wrong SFE predictions.

Despite the recent progress, SFE simulations for many HEAs as well as a complete consideration of all thermal excitations (i.e., electronic, magnetic, lattice vibrations) are still lacking. The inclusion of higher-order coupling terms into finite-temperature SFE predictions such as, e.g., the coupling between lattice vibrations and electronic free energies by performing explicit *ab initio* molecular dynamics simulations, has only recently become possible for pure elements. The extension towards a complete finite-temperature description of SFEs of magnetic alloys is one of the current challenges in *ab initio* modeling.

### 4.4. Multi-phase High Entropy and Compositionally Complex Alloys

Until recently, most of the works on HEAs/CCAs aimed at single phase solid solutions. Li et al. [239] proposed an alternative design strategy of HEAs/CCAs based on their experimental finding of a dual-phase (DP) HEA[7] consisting of the fcc and the hcp phases, namely the $Co_{10}Cr_{10}Fe_{50}Mn_{30}$ alloy. This alloy revealed the TRIP effect as well as enhanced mechanical properties.

In close analogy to the discussion for SFEs in Section 4.3, the hcp-fcc energy difference can be interpreted as an indicator whether a dual-phase alloy is likely to form or not. In Ref. [108], a combined *ab initio* and experimental work was proposed to reveal DP-HEAs. First, EMTO-

[7] According to the present definition of HEAs as single-phase materials it would be more appropriate to use the notation of a CCA for the "dual-phase HEA" of Li et al. [239].

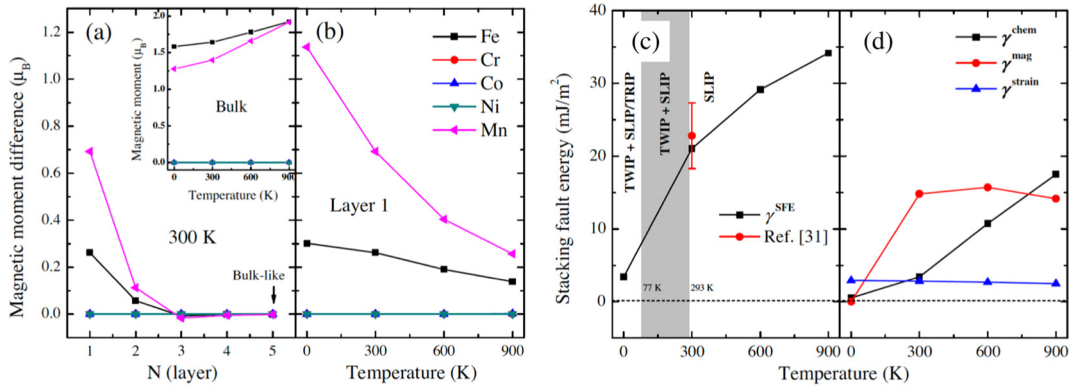


**Fig. 28.** (a) Dependence of local magnetic moments on the distance from the stacking fault in the CoCrFeMnNi alloy where *N* denotes the *N*-th nearest-neighbor layer from the stacking fault (see also sketch in Fig. 26). The differences of magnetic moments to the bulk values are shown. (b) Temperature dependence of the local magnetic moments in the layer close to the SF, where the temperature effect originates from the lattice expansion taken from experiment. (c) Temperature dependence of the computed SFEs. (d) Separation of the SFE into magnetic, chemical, and strain contributions. Note that the chemical contribution, $\gamma^{chem}$, indicates the *ab initio* derived hcp–fcc energy differences at the given experimental lattice constant.
Source: Adapted from Ref. [228].

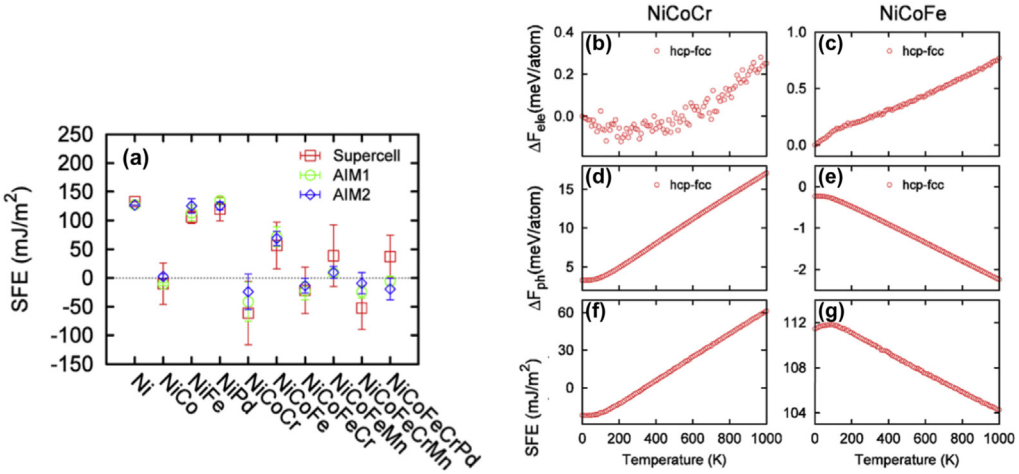


**Fig. 29.** (a) SFE at 0 K for a set of ten alloys. Calculations were based on supercell models with explicit stacking faults (denoted as "Supercell"), as well as the first and the second order ANNNI model denoted in the figure as "AIM1" and "AIM2". (b)–(e) Electronic and vibrational free energy difference (denoted as $\Delta F_{ele}$ and $\Delta F_{ph}$) between the hcp and fcc phase. (f) and (g) show the computed SFEs for NiCoCr and NiCoFe alloys.
Source: Adapted from Ref. [106].

CPA calculations were performed to determine the phase stabilities of $Co_{20}Cr_{20}Fe_{40-x}Mn_{20}Ni_x$ ($x$ = 0–20 at.%) HEAs and to explore promising compositions. The calculations included thermal excitations of lattice vibrations and magnetic fluctuations via the Debye model and the mean field approach, respectively, as discussed in Section 3.3 and in Ref. [101]. Fig. 30 (a) reveals the hcp-fcc Gibbs energy difference for $Co_{20}Cr_{20}Fe_{40-x}Mn_{20}Ni_x$ alloys. The impact of thermal magnetic and vibration excitations is highlighted by the shaded green and blue areas, respectively. The simulations performed at the theoretical and experimental lattice constant highlight the sensitivity of the hcp-fcc energy difference with respect to the chosen lattice parameter. It can be also seen that the finite-temperature contributions of lattice vibrations and magnetic fluctuations substantially affect the phase stability of the $Co_{20}Cr_{20}Fe_{40-x}Mn_{20}Ni_x$ alloys. In order to select promising DP HEAs, the hcp-fcc Gibbs energy difference of the previously reported $Co_{10}Cr_{10}Fe_{50}Mn_{30}$ served as a reference energy. According to the simulations, three alloys, namely the CoCrFeMnNi alloy, $Co_{20}Cr_{20}Fe_{34}Mn_{20}Ni_6$, as well as $Co_{20}Cr_{20}Fe_{40}Mn_{20}$, were selected and synthesized, and their mechanical properties experimentally evaluated. Fig. 30 shows the XRD patterns for the three alloys including the non-equiatomic $Co_{20}Cr_{20}Fe_{34}Mn_{20}Ni_6$ (middle row). The latter alloy indeed exhibits both phases, hcp and fcc, reveals the TRIP effect and much higher ultimate tensile strength as well as strain-hardening ability compared to the corresponding equiatomic CoCrFeMnNi alloy [108].

This combined experimental–*ab initio* work highlights the design potential for mechanical properties by introducing the TRIP-DP effect into HEAs and once more the predictive power of *ab initio* simulations in exploring the compositional space for alloy design purposes.

## 5. Summary and Outlook

We have provided a comprehensive review of the exponentially growing *ab initio* efforts in simulating multicomponent alloys with multiple principal elements, specifically focusing on high entropy alloys (HEAs) and compositionally complex alloys (CCAs). Even though investigations of these materials classes are generally dominated by experiments, a considerable number of material properties and atomistic quantities have also been explored by *ab initio* simulations utilizing in particular density functional theory (DFT). This is impressively summarized in Table 9 in the Appendix where all HEAs and CCAs (and

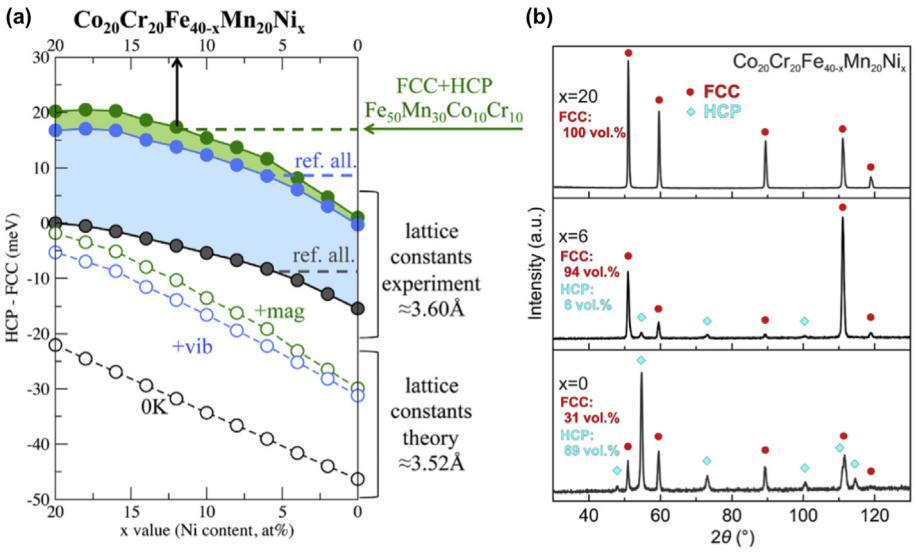


**Fig. 30.** (a) *Ab initio* computed hcp-fcc Gibbs energy difference for $Co_{20}Cr_{20}Fe_{40-x}Mn_{20}Ni_x$ alloys [108]. Calculations were performed at the theoretical (~3.52 Å) and experimental lattice constant (~3.60 Å). The hcp-fcc energy difference of the reference $Cr_{10}Co_{10}Fe_{50}Mn_{30}$ alloy is indicated by a green dashed line. (b) Complementary experiments in Ref. [108] confirmed that $Co_{20}Cr_{20}Fe_{34}Mn_{20}Ni_6$ is a hcp-fcc dual-phase alloy consistently with the theoretical predictions. (For interpretation of the references to color in this figure legend, the reader is referred to the web version of this article.)
Source: Adapted from Ref. [108]

related lower order systems) are listed that have been investigated so far with DFT. In this review we have not only summarized the previous research on these alloys, but we have also explained the state-of-the-art DFT methodologies used to explore thermodynamic and mechanical properties. We stress that these computational tools and concepts are not limited to HEAs and CCAs but are likewise applicable to ordered alloys, conventional random solid solutions, and to multicomponent alloys in general.

The main approximation within DFT relates to the treatment of the exchange-correlation functional. Out of the two standard approximations, LDA and GGA, the vast majority of previous works on HEAs and CCAs have employed GGA. For magnetic materials, this is a reasonable choice because of the well-known failure of LDA to predict the ground state of pure iron. However, at least for non-magnetic alloys, it would be desirable to evaluate both functionals in order to clarify whether a similar *ab initio* confidence interval for experimental data exists for HEAs and CCAs as it does for unary elements and ordered compounds.

One of the most important concepts for practical DFT calculations of random solid solutions is the assumption of ideal mixing, which can be treated using established methodologies based on either a supercell approach or the coherent potential approximation (CPA). The CPA is a very computationally efficient framework as it enables the simulation of disordered alloys using only the primitive cell. It lacks, however, the inclusion of local lattice distortions — one of the originally proposed core effects of HEAs — and thus cannot be applied to include relaxation effects or to extract interatomic forces for the computation of lattice vibrations. In contrast, lattice distortions can be straightforwardly included in the computationally more expensive supercell-based approaches (SQS, Monte Carlo, molecular dynamics, phonon calculations). For some alloys, the impact of distortions can be significant for various properties (e.g., formation energies), whereas other alloys are largely unaffected. Some properties, such as elastic constants, tend not to be significantly impacted in any alloy. For wide-range studies, CPA is the preferable choice in terms of computational efficiency, but for quantitative predictions the impact of lattice distortions may require subsequent supercell calculations.

The main advantage of the ideal mixing assumption is that many quantities such as, e.g., elastic or finite-temperature properties, can be derived directly from the ground state energy surface; of course this is limited by the approximation of the chosen thermodynamic concept. Finite-temperature excitations can result in important entropy contributions and can be decisive for determining phase stabilities. Excitations related to electrons (number of electron-hole pairs) and magnetic excitations (number of quantum spin states) can be understood in a nice analogy to chemical disorder (number of degenerated configurations). For lattice vibrations the approximate Debye-Grüneisen model is highly efficient and provides reasonable accuracy. Only recent advances in modeling vibrations in random alloys have resulted in explicit phonon calculations showing, for example, a strong broadening of the phonon dispersion at higher frequencies. The inclusion of anharmonic contributions for HEAs and CCAs, in particular anharmonic free energies, is still in its infancy. Recent advances for unaries and selected ordered compounds using sophisticated molecular-dynamics based methods reveal, however, promising routes in this direction.

There is a large class of HEAs and CCAs with magnetism, which thus requires the spin-polarized version of DFT. We stress in particular that realistically modeling alloys in their paramagnetic state, i.e., above the Curie temperature, is not generally possible by resorting to non-spin-polarized DFT calculations. In most cases, local magnetic moments are preserved, even in the paramagnetic regime, and are disordered. The concepts within DFT to model magnetic disorder are analogous to those for chemical disorder and thus commonly based on the supercell or CPA formalism. In order to establish the most realistic magnetic state for practical DFT simulations the knowledge about the magnetic order-disorder temperature (i.e., the Curie or Néel temperature) is crucial. Different concepts to determine these values from DFT and their applications to HEAs and CCAs in previous works have been discussed. The modeling of magnetic excitations for magnetic free energy contributions for HEAs and CCAs is so far mainly based on rather approximative mean field theories suggesting a large potential for further method development.

It is challenging to determine the phase stability regions of HEAs and CCAs from DFT. The reason is the possibility of decomposition into phases at different, generally unknown compositions. *If* the competing phases and their compositions are known, e.g., from phase diagram calculations or experiments, or can be deduced from semi-empirical selection rules, then the described DFT based techniques can be used to compute the Gibbs energy for each of the relevant phases and the most stable phase(s) can be determined. In such a case, approximate order-disorder transition temperatures can also be straightforwardly derived utilizing the ideal mixing approximation. The main challenge, however, is to select the competing phases. A brute-force approach is to consider a large pool of subsystems, e.g., to take for a given HEA a large number of binary and ternary ordered and disordered phases into consideration. This approach is computationally costly and system dependent. One of the most promising alternatives is the combination of DFT with thermodynamic approaches such as CALPHAD. Such a coupling is of mutual

benefit — many currently available thermodynamic databases are not yet optimized for HEAs and CCAs and lack information, e.g., on many ternary alloys required for a reliable extrapolation to multi-principal element alloys. DFT computations can provide the required information and thus pave the way for the next-generation of HEA/CCA thermodynamic databases.

For order-disorder transitions that are not accompanied by a structural transition, DFT based techniques are available that enable the prediction of phase decomposition without an *a priori* knowledge of the relevant phases. These techniques go beyond the ideal mixing approximation by taking chemical short-range order into account. This renders them conceptionally and computationally challenging. Different schemes have been reviewed with a focus on CPA-based (GPM method, S2-formalism) and supercell-based approaches (e.g., cluster expansion). Similar advantages and disadvantages apply as discussed for the representation of chemical disorder, mainly: high computational efficiency for CPA calculations and the possibility to include local lattice distortions in the supercell calculations. The techniques can be used to compute ordering tendencies, chemical short-range order, accurate order-disorder transition temperatures, and phase decomposition of the solid solution. The strength of these techniques is demonstrated by the various applications to different alloy systems discussed and we expect further developments in these directions.

We have shown how various mechanical properties, which can be linked to the alloys' strength and plasticity, are accessible via DFT simulations. Elastic constants for example are readily accessible from DFT (if finite-temperature excitations are neglected) and consequently a large portion of the previous DFT studies on HEAs and CCAs has been devoted to these materials properties. Theories for solid solution strengthening provide a further link to DFT calculations, e.g., via the local misfit volume. Recent works that suggest a correlation between local lattice distortions and the solid solution strengthening contribution to the yield strength have been discussed, further corroborating the potential of DFT computations for accessing mechanical properties. The present research in this direction appears promising and encourages the development of a stronger connection between *ab initio* calculations and models for solid solutions strengthening. The SFE, a central quantity linking DFT calculations to macroscopic mechanical behavior, is also calculable by DFT simulations. We have discussed how temperature effects can be included in such calculations and how the SFE can vary under finite-temperature excitations. Based on this, more recent design strategies of dual-phase alloys by tuning the fcc-hcp phase stability have been reviewed. This opens a path to new classes of multiple-phase CCAs.

State-of-the-art thermodynamic concepts and computational techniques have impressively paved the way to address various materials properties of multi-principal element alloys by *ab initio* calculations. The success of DFT to simulate key properties for these alloys is demonstrated by the present exponential increase in the number of DFT-based research papers for HEAs and CCAs. A number of encouraging directions to improve and strengthen previous thermodynamic and simulation concepts have been pointed out above. In the following, we summarize some more research topics which can be addressed by means of DFT, but will require new method developments.

Kinetic aspects of multicomponent alloys such as the often raised *sluggish diffusion* effect in HEAs — one of the originally proposed core effects — could significantly influence creep properties in practical (long-timescale) applications, but are still poorly understood. This is mainly due to the fact that the required DFT methods to address kinetics in these alloys are still in their infancy. Progress has been made for random binaries, e.g., by applying cluster expansion techniques to capture the kinetic parameters in combination with kinetic Monte Carlo techniques. Such methods — although not yet advanced enough to be applicable to multi-principal element alloys — could in the future provide access to many so-far unexplored and unknown kinetic properties of HEAs and CCAs.

Oxidation and corrosion resistance is another important factor determining the practical applicability of HEAs and CCAs under realistic conditions. DFT-based investigations in this direction would require a number of methodological developments such as the extension of bulk stabilities (discussed in the present review) to surface stabilities and the computation of oxide formation under corrosive environments including, e.g., electric fields. Related methodological advances — although very challenging — would certainly fall on fertile ground in the field of HEAs and CCAs.

In general, it is our view that for specific materials properties, e.g., strength or corrosion resistance, highly-tuned established alloys exist (e.g., high-strength steels) which are likely superior for a given specific property than any HEA or CCA. We therefore see the strongest potential of multi-principal element alloys in general not in overcoming the performance for *one* particular materials property against established alloys, but in the tuning and optimization of *multiple* materials properties by exploring the immense compositional space. To this end, we envision a multiple optimization of HEAs and CCAs to design alloys with a well-defined set of appreciative properties by means of *ab initio* simulation techniques which can quantitatively predict various materials properties.

## Acknowledgment

We gratefully acknowledge K. Albe, B. Alling, M. Gao, L. Huber, D. Irving, D. Raabe, M. Selleby, S.L. Shang, P. Singh, M.H.F. Sluiter, F. Tian, W.Y. Wang, M. Widom, and X. Zhang for fruitful discussions.

Y.I. acknowledges the Grant-in-Aid for Scientific Research on Innovative Areas “Nano Informatics” (Grant No. 25106005) from the Japan Society for the Promotion of Science (JSPS), the Funding by the Ministry of Education, Culture, Sports, Science and Technology (MEXT), Japan, through Elements Strategy Initiative for Structural Materials (ESISM) of Kyoto University, and the Grant-in-Aid for Young Scientist (B) of JSPS (Grant No.16K18228). Funding from the Deutsche Forschungsgemeinschaft (SPP 1568, SPP 2006), from the Netherlands Organisation for Scientific Research (NWO) under VIDI grant 15707 and the European Research Council (ERC) under the European Union's Horizon 2020 research and innovation programme (Grant agreement No. 639211) is gratefully acknowledged.

## Appendix A

In Table 9, we provide a comprehensive overview over all HEAs and CCAs investigated in the literature until the present (mid-2018). We have also included binaries and ternaries when they were investigated within any of the HEA or CCA studies. Note that this does not imply a complete overview over *all* binaries and ternaries studied by means of DFT in the literature so far. Additionally, we provide a set of *properties* to facilitate the

search through the database. The complete materials-property list in Table 9 contains more than 200 alloys and more than 500 materials-property entries.

**Table 9**
Summary of alloys and properties that have been investigated with *ab initio* until mid-2018. Note that only those binary and ternary alloys have been taken into account that were part of HEA/CCA studies. We also refer to the study of Lederer et al. [164] where the phase stability of approximately 1800 equiatomic HEAs/CCAs from binaries up to quinaries was calculated based on the AFLOW database [186].

| Alloy | Property | References |
|---|---|---|
| AgAuCu | Chemical SRO | Khan et al. [160] |
| | Magnetic properties | Khan et al. [160] |
| $Ag_xCoCr_yFeNi$ | Magnetic properties | Körmann et al. [142] |
| AgCoCuFeNi | Magnetic properties | Huang et al. [146] |
| AgPdRh | Chemical SRO | Khan et al. [160] |
| | Magnetic properties | Khan et al. [160] |
| AlCoCrCuFeNi | Magnetic properties | Huang et al. [146] |
| $Al_{1.3}$CoCrCuFeNi | Chemical SRO | Santodonato et al. [139], Gao and Alman [220] |
| | Diffusion | Gao and Alman [220] |
| | Local lattice distortions | Santodonato et al. [139], Gao and Alman [220] |
| $Al_x$CoCrCuFeNi | SFE | Beyramali Kivy and Asle Zaeem [230] |
| AlCoCrCuFeNiSi | Magnetic properties | Huang et al. [146] |
| AlCoCrCuNi | Magnetic properties | Huang et al. [146] |
| AlCoCrFeMn | Magnetic properties | Huang et al. [146] |
| $Al_x$CoCrFeMn | Chemical SRO | Singh et al. [171] |
| | Elastic properties | Huang et al. [145] |
| | Magnetic properties | Huang et al. [145], Singh et al. [171] |
| | Phase stability | Huang et al. [145], Singh et al. [171] |
| $Al_x$CoCrFeMnNi | Finite-*T* excitations | Sun et al. [72] |
| | Magnetic properties | Sun et al. [72] |
| | Phase stability | Sun et al. [72] |
| $Al_{0.3}CoCrFeMo_{0.1}Ni$ | SFE | Beyramali Kivy and Asle Zaeem [230] |
| AlCoCrFeNi | Chemical LRO | Singh et al. [156] |
| | Chemical SRO | Singh et al. [156] |
| | Magnetic properties | Huang et al. [146] |
| | Phase stability | Singh et al. [156] |
| $AlCoCrFeNi_x$ | Magnetic properties | Jasiewicz et al. [240] |
| | Phase stability | Jasiewicz et al. [240] |
| $AlCoCrFe_xNi$ | Magnetic properties | Jasiewicz et al. [240] |
| | Phase stability | Jasiewicz et al. [240] |
| $AlCoCr_xFeNi$ | Magnetic properties | Jasiewicz et al. [240] |
| | Phase stability | Jasiewicz et al. [240] |
| $AlCo_xCrFeNi$ | Magnetic properties | Jasiewicz et al. [240] |
| | Phase stability | Jasiewicz et al. [240] |
| $Al_{0.25}$CoCrFeNi | Magnetic properties | Körmann et al. [142] |
| $Al_x$CoCrFeNi | Chemical LRO | Singh et al. [156], Ogura et al. [166] |
| | Chemical SRO | Singh et al. [156] |
| | Elastic properties | Tian et al. [70] |
| | Finite-*T* excitations | Tian et al. [70] |
| | Magnetic properties | Huang et al. [143], Ogura et al. [166], Jasiewicz et al. [240] |

(*continued on next page*)

**Table 9** (*continued*)

| Alloy | Property | References |
|---|---|---|
| | Phase stability | Tian et al. [70], Leong et al. [84], Singh et al. [156], Ogura et al. [166], Jasiewicz et al. [240] |
| | SFE | Beyramali Kivy and Asle Zaeem [230] |
| Al–Co–Cr–Fe–Ni | Chemical SRO | Ma et al. [167] |
| | Local lattice distortions | Ma et al. [167] |
| AlCoCrFeNiTi | Magnetic properties | Huang et al. [146] |
| $Al_{0.3}CoCrFeNiTi_{0.1}$ | SFE | Beyramali Kivy and Asle Zaeem [230] |
| AlCoCuFeNi | Magnetic properties | Huang et al. [146] |
| AlCoCuFeNiSi | Magnetic properties | Huang et al. [146] |
| AlCoCuFeNiTi | Magnetic properties | Huang et al. [146] |
| AlCoCuNi | Magnetic properties | Huang et al. [146] |
| AlCoFeNi | Magnetic properties | Huang et al. [146] |
| $Al_xCoFeNiSi_x$ | Chemical SRO | Feng et al. [161] |
| | Elastic properties | Feng et al. [161] |
| | Local lattice distortions | Feng et al. [161] |
| | Phase stability | Feng et al. [161] |
| Al–Co–Fe–Ni–Ti | Magnetic properties | Nguyen et al. [165] |
| | Phase stability | Nguyen et al. [165] |
| AlCrCuFeNi | Magnetic properties | Huang et al. [146] |
| AlCrFe | Magnetic properties | Huang et al. [146] |
| AlCrFeMn | Magnetic properties | Huang et al. [146] |
| $Al_{1.5}CrFeMnTi$ | Chemical LRO | Feng et al. [140] |
| | Chemical SRO | Feng et al. [140] |
| | Diffusion | Feng et al. [140] |
| | Local lattice distortions | Feng et al. [140] |
| | Phase stability | Feng et al. [140] |
| AlCrFeMnV | Magnetic properties | Huang et al. [146] |
| AlCrFeV | Magnetic properties | Huang et al. [146] |
| AlCrMn | Magnetic properties | Huang et al. [146] |
| AlCrMnTi | Magnetic properties | Huang et al. [146] |
| AlCrMnTiV | Magnetic properties | Huang et al. [146] |
| AlCrMnV | Magnetic properties | Huang et al. [146] |
| AlCrMoNbVW | Magnetic properties | Huang et al. [146] |
| AlCrNbVW | Magnetic properties | Huang et al. [146] |
| AlCrV | Magnetic properties | Huang et al. [146] |
| AlCuFeNiTi | Magnetic properties | Huang et al. [146] |
| AlCuNi | Magnetic properties | Huang et al. [146] |
| AlFeMnV | Magnetic properties | Huang et al. [146] |
| Al–Fe–Ni | Magnetic properties | Nguyen et al. [165] |

(*continued on next page*)

**Table 9** (*continued*)

| Alloy | Property | References |
|---|---|---|
| | Phase stability | Nguyen et al. [165] |
| AlFeTiV | Magnetic properties | Huang et al. [146] |
| AlFeV | Magnetic properties | Huang et al. [146] |
| $Al_{0.05}Hf_{0.25}Sc_{0.20}Ti_{0.25}Zr_{0.25}$ | Chemical LRO<br>Finite-*T* excitations<br>Phase stability | Rogal et al. [66]<br>Rogal et al. [66]<br>Rogal et al. [66] |
| $Al_{0.15}Hf_{0.25}Sc_{0.10}Ti_{0.25}Zr_{0.25}$ | Chemical LRO<br>Elastic properties<br>Finite-*T* excitations<br>Phase stability | Rogal et al. [66]<br>Rogal et al. [66]<br>Rogal et al. [66]<br>Rogal et al. [66] |
| $Al_xHf_{1-x}NbTaTiZr$ | Elastic properties | Li et al. [192] |
| AlMnTiV | Magnetic properties | Huang et al. [146] |
| AlMnV | Magnetic properties | Huang et al. [146] |
| AlMoNbTiV | Elastic properties<br>Local lattice distortions | Zheng et al. [205]<br>Zheng et al. [205] |
| $Al_xMoNbTiV$ | Elastic properties<br>Phase stability | Cao et al. [191]<br>Cao et al. [191] |
| AlMoNbV | Elastic properties<br>Finite-*T* excitations<br>Magnetic properties | Ge et al. [196]<br>Ge et al. [196]<br>Huang et al. [146] |
| $Al_{0.05}Mo_{0.40}Ta_{0.05}Ti_{0.05}W_{0.40}Zr_{0.05}$ | Chemical SRO | Singh et al. [170] |
| AlNbTaTiZr | Elastic properties | Li et al. [192] |
| Al–Nb–Ti | Chemical LRO<br>Chemical SRO<br>Phase stability | Singh et al. [156]<br>Singh et al. [156]<br>Singh et al. [156] |
| AlNbTiV | Elastic properties<br>Local lattice distortions | Song et al. [69]<br>Song et al. [69] |
| AlNbVW | Magnetic properties | Huang et al. [146] |
| $Au_xCoCr_yFeNi$ | Magnetic properties | Körmann et al. [142] |
| AuPt | Chemical LRO<br>Phase stability | Niu et al. [174]<br>Niu et al. [174] |
| $Be_{0.225}Cu_{0.125}Ni_{0.10}Ti_{0.14}Zr_{0.41}$ | Chemical SRO | Wang et al. [216] |
| CoCr | Elastic properties<br>Local lattice distortions<br>Phase stability<br>Point defects | Ye et al. [204]<br>Chen et al. [113], Ye et al. [204]<br>Chen et al. [113]<br>Chen et al. [113] |
| CoCrCuFeMn | Magnetic properties<br>Phase stability | Huang et al. [146]<br>Wu et al. [33] |
| CoCrCuFeMnNi | Magnetic properties<br>SFE | Huang et al. [146]<br>Beyramali Kivy and Asle Zaeem [230] |
| CoCrCuFeNi | Chemical LRO<br>Chemical SRO<br>Elastic properties | Wu et al. [155]<br>Wu et al. [155]<br>Huang et al. [144] |

(*continued on next page*)

**Table 9** (*continued*)

| Alloy | Property | References |
|---|---|---|
| | Finite-*T* excitations | Huang et al. [144], Wu et al. [155] |
| | Magnetic properties | Huang et al. [144, 146] |
| | Phase stability | Huang et al. [144], Wu et al. [155] |
| | SFE | Beyramali Kivy and Asle Zaeem [230] |
| $CoCrCu_{0.5}FeNi$ | SFE | Beyramali Kivy and Asle Zaeem [230] |
| $CoCr_xCu_yFeNi$ | Magnetic properties | Körmann et al. [142] |
| CoCrCuFeNiTi | Elastic properties | Tian et al. [187] |
| | Magnetic properties | Tian et al. [187] |
| $CoCrCuFeNiTi_{0.5}$ | SFE | Beyramali Kivy and Asle Zaeem [230] |
| $CoCrCuFeNiTi_x$ | Elastic properties | Tian et al. [187] |
| | Magnetic properties | Tian et al. [187] |
| CoCrFe | Elastic properties | Ye et al. [204] |
| | Local lattice distortions | Ye et al. [204] |
| CoCrFeGaNi | Elastic properties | Huang et al. [197] |
| | Finite-*T* excitations | Huang et al. [197] |
| | Magnetic properties | Huang et al. [143,197] |
| | Phase stability | Huang et al. [197] |
| CoCrFeGeMnNi | Magnetic properties | Huang et al. [146] |
| CoCrFeMn | Chemical SRO | Singh et al. [171] |
| $Co_{0.1}Cr_{0.1}Fe_{0.4}Mn_{0.4}$ | Elastic properties | Li et al. [201] |
| CoCrFeMnNi | Elastic properties | Song et al. [69], Ma et al. [101], Ge et al. [103], Zaddach et al. [188], Li et al. [201], Ye et al. [204], Patriarca et al. [229] |
| | Finite-*T* excitations | Sun et al. [72], Ma et al. [101], Ge et al. [103], Zhao et al. [106], Huang et al. [228], Niu et al. [235] |
| | Local lattice distortions | Wu et al. [33], Song et al. [69], Zaddach et al. [188], Ye et al. [204], Oh et al. [223], Okamoto et al. [224] |
| | Magnetic properties | Wu et al. [33], Song et al. [69], Sun et al. [72], Ma et al. [101], Ge et al. [103], Körmann et al. [142], Huang et al. [146, 228], Niu et al. [235], Jin et al. [241], Schneeweiss et al. [242] |
| | Phase stability | Troparevsky et al. [17], Wu et al. [33], Sun et al. [72], Ma et al. [101], Niu et al. [235], Huang et al. [243] |
| | SFE | Zhao et al. [106], Zaddach et al. [188], Huang et al. [228], Patriarca et al. [229], Beyramali Kivy and Asle Zaeem [230], Alkan et al. [233], Huang et al. [234], Niu et al. [235], Huang et al. [243] |
| $Co_{0.20}Cr_{0.14}Fe_{0.20}Mn_{0.20}Ni_{0.26}$ | Elastic properties | Zaddach et al. [188] |
| | SFE | Zaddach et al. [188] |
| $Co_{0.20}Cr_{0.17}Fe_{0.20}Mn_{0.20}Ni_{0.23}$ | Elastic properties | Zaddach et al. [188] |
| | SFE | Zaddach et al. [188] |
| $Co_{0.20}Cr_{0.26}Fe_{0.20}Mn_{0.20}Ni_{0.14}$ | Elastic properties | Zaddach et al. [188] |
| | SFE | Zaddach et al. [188] |
| $Co_{0.215}Cr_{0.215}Fe_{0.215}Mn_{0.215}Ni_{0.14}$ | Elastic properties | Zaddach et al. [188] |
| | SFE | Zaddach et al. [188] |
| CoCrFeMnNiTi | Magnetic properties | Huang et al. [146] |
| CoCrFeMnNiV | Magnetic properties | Huang et al. [146] |
| CoCrFeNi | Chemical LRO | Niu et al. [154], Singh et al. [156] |
| | Chemical SRO | Singh et al. [156], Tamm et al. [157] |

(*continued on next page*)

**Table 9** (*continued*)

| Alloy | Property | References |
|---|---|---|
| | Diffusion | Middleburgh et al. [112], Zhao et al. [114] |
| | Elastic properties | Song et al. [69], Ge et al. [103], Tian et al. [187], Zaddach et al. [188], Li et al. [201], Ye et al. [204] |
| | Finite-*T* excitations | Gao et al. [24, 25], Ge et al. [103], Zhao et al. [106], Jin et al. [127] |
| | Local lattice distortions | Wu et al. [33], Song et al. [69], Chen et al. [113], Zaddach et al. [188], Ye et al. [204], Egami et al. [221], Okamoto et al. [224] |
| | Magnetic properties | Troparevsky et al. [17], Wu et al. [33], Song et al. [69], Ge et al. [103], Chen et al. [113], Körmann et al. [142], Huang et al. [143, 146], Niu et al. [154], Tamm et al. [157], Tian et al. [187], Jin et al. [241] |
| | Phase stability | Troparevsky et al. [17], Gao et al. [24, 25], Wu et al. [33], Leong et al. [84], Chen et al. [113], Niu et al. [154], Singh et al. [156], Tamm et al. [157], Zhang et al. [231, 244] |
| | Point defects | Middleburgh et al. [112], Chen et al. [113], Zhao et al. [114] |
| | SFE | Zhao et al. [106], Zaddach et al. [188], Beyramali Kivy and Asle Zaeem [230], Zhang et al. [231], Huang et al. [234] |
| $CoCr_xFeNi$ | Magnetic properties | Körmann et al. [142] |
| Co–Cr–Fe–Ni | Elastic properties | Niu et al. [194] |
| | Magnetic properties | Niu et al. [194] |
| | Phase stability | Niu et al. [194] |
| CoCrFeNiPd | Finite-*T* excitations | Zhao et al. [106] |
| | Local lattice distortions | Wu et al. [33] |
| | Magnetic properties | Wu et al. [33], Huang et al. [146], Jin et al. [241] |
| | Phase stability | Wu et al. [33] |
| | SFE | Zhao et al. [106] |
| $CoCrFeNiPd_x$ | Phase stability | Leong et al. [84] |
| $CoCr_xFeNiPd_y$ | Magnetic properties | Körmann et al. [142] |
| CoCrFeNiTi | Elastic properties | Tian et al. [187] |
| | Magnetic properties | Huang et al. [146], Tian et al. [187] |
| $CoCrFeNiTi_x$ | Phase stability | Leong et al. [84] |
| $CoCrFeNiV_x$ | Phase stability | Leong et al. [84] |
| $Co_{0.1}Cr_{0.1}Fe_{0.8-x}Mn_x$ | Phase stability | Huang et al. [243] |
| | SFE | Huang et al. [243] |
| $CoCrFe_{1-x}MnNi_x$ | Finite-*T* excitations | Li et al. [108] |
| | Phase stability | Li et al. [108] |
| CoCrMnNi | Elastic properties | Ge et al. [103] |
| | Finite-*T* excitations | Ge et al. [103] |
| | Local lattice distortions | Okamoto et al. [224] |
| | Magnetic properties | Ge et al. [103] |
| | SFE | Huang et al. [234] |
| CoCrMnNiV | Phase stability | Troparevsky et al. [17], Wu et al. [33] |
| CoCrMoW | Elastic properties | Tian et al. [198] |
| | Magnetic properties | Tian et al. [198] |
| | Phase stability | Tian et al. [198] |
| CoCrNi | Chemical SRO | Tamm et al. [157], Ding et al. [245] |
| | Diffusion | Zhao et al. [114] |
| | Elastic properties | Ge et al. [103], Li et al. [201], Ye et al. [204] |

(*continued on next page*)

**Table 9** (*continued*)

| Alloy | Property | References |
|---|---|---|
| | Finite-*T* excitations | Ge et al. [103], Zhao et al. [106], Zhang et al. [232], Niu et al. [235] |
| | Local lattice distortions | Ye et al. [204], Okamoto et al. [224], Zhang et al. [232] |
| | Magnetic properties | Wu et al. [33], Ge et al. [103], Huang et al. [146], Tamm et al. [157], Zhang et al. [232], Niu et al. [235], Jin et al. [241] |
| | Phase stability | Tamm et al. [157], Zhang et al. [231, 232], Niu et al. [235], Huang et al. [243], Ding et al. [245] |
| | Point defects | Zhao et al. [114] |
| | SFE | Zhao et al. [106], Zhang et al. [231, 232], Huang et al. [234], Niu et al. [235], Huang et al. [243], Ding et al. [245] |
| CoCuFeMnNi | Elastic properties | Huang et al. [144] |
| | Finite-*T* excitations | Huang et al. [144] |
| | Magnetic properties | Huang et al. [144,146] |
| | Phase stability | Huang et al. [144] |
| CoCuFeMoNi | Magnetic properties | Huang et al. [146] |
| CoCuFeNi | Elastic properties | Huang et al. [144] |
| | Finite-*T* excitations | Huang et al. [144] |
| | Magnetic properties | Huang et al. [144, 146] |
| | Phase stability | Huang et al. [144] |
| CoCuFeNiPt | Magnetic properties | Huang et al. [146] |
| CoCuFeNiV | Elastic properties | Huang et al. [144] |
| | Finite-*T* excitations | Huang et al. [144] |
| | Magnetic properties | Huang et al. [144, 146] |
| | Phase stability | Huang et al. [144] |
| CoCuNi | Chemical SRO | Khan et al. [160] |
| | Magnetic properties | Khan et al. [160] |
| CoFe | Elastic properties | Ye et al. [204] |
| | Local lattice distortions | Chen et al. [113], Ye et al. [204] |
| | Phase stability | Chen et al. [113] |
| | Point defects | Chen et al. [113] |
| CoFeGaMnNi | Magnetic properties | Huang et al. [146] |
| CoFeMnMoNi | Magnetic properties | Huang et al. [146] |
| | Phase stability | Wu et al. [33] |
| CoFeMnNi | Elastic properties | Ge et al. [103] |
| | Finite-*T* excitations | Ge et al. [103], Zhao et al. [106] |
| | Local lattice distortions | Okamoto et al. [224] |
| | Magnetic properties | Wu et al. [33], Ge et al. [103], Huang et al. [146] |
| | SFE | Zhao et al. [106] |
| CoFeMnNiV | Magnetic properties | Huang et al. [146] |
| | Phase stability | Troparevsky et al. [17], Wu et al. [33] |
| CoFeNi | Chemical SRO | Feng et al. [161] |
| | Elastic properties | Song et al. [69], Ge et al. [103], Feng et al. [161], Ye et al. [204] |
| | Finite-*T* excitations | Ge et al. [103], Zhao et al. [106], Niu et al. [235] |
| | Local lattice distortions | Song et al. [69], Feng et al. [161], Ye et al. [204], Egami et al. [221], Okamoto et al. [224] |
| | Magnetic properties | Wu et al. [33], Song et al. [69], Ge et al. [103], Körmann et al. [142], Huang et al. [146], Niu et al. [235], Jin et al. [241] |
| | Phase stability | Troparevsky et al. [68], Feng et al. [161], Niu et al. [235] |
| | SFE | Zhao et al. [106] |
| CoMnNi | Elastic properties | Ge et al. [103] |

(*continued on next page*)

**Table 9** (*continued*)

| Alloy | Property | References |
|---|---|---|
| | Finite-$T$ excitations | Ge et al. [103], Niu et al. [235] |
| | Local lattice distortions | Okamoto et al. [224] |
| | Magnetic properties | Wu et al. [33], Ge et al. [103], Niu et al. [235] |
| | Phase stability | Niu et al. [235] |
| CoNi | Elastic properties | Ge et al. [103], Ye et al. [204] |
| | Finite-$T$ excitations | Ge et al. [103], Zhao et al. [106], Jin et al. [127] |
| | Local lattice distortions | Chen et al. [113], Ye et al. [204] |
| | Magnetic properties | Wu et al. [33], Ge et al. [103], Jin et al. [241] |
| | Phase stability | Chen et al. [113] |
| | Point defects | Zhao et al. [35], Chen et al. [113] |
| | SFE | Zhao et al. [106] |
| CoOsReRu | Finite-$T$ excitations | Gao et al. [24, 25] |
| | Phase stability | Gao et al. [24, 25] |
| CrCuFeMnNi | Magnetic properties | Huang et al. [146] |
| CrCuFeMoNi | Magnetic properties | Huang et al. [146] |
| CrCuMoW | Elastic properties | Tian et al. [198] |
| | Magnetic properties | Tian et al. [198] |
| | Phase stability | Tian et al. [198] |
| CrFe | Elastic properties | Ye et al. [204] |
| | Local lattice distortions | Chen et al. [113], Ye et al. [204] |
| | Phase stability | Chen et al. [113] |
| | Point defects | Chen et al. [113] |
| Cr–Fe | Chemical LRO | Wróbel et al. [159] |
| | Chemical SRO | Wróbel et al. [159] |
| | Magnetic properties | Wróbel et al. [159] |
| | Phase stability | Wróbel et al. [159] |
| CrFeMnNiTi | Phase stability | Troparevsky et al. [17], Wu et al. [33] |
| CrFeMnV | Magnetic properties | Huang et al. [146] |
| CrFeMoNiW | Elastic properties | Tian et al. [198] |
| | Magnetic properties | Tian et al. [198] |
| | Phase stability | Tian et al. [198] |
| CrFeMoTiV | Magnetic properties | Huang et al. [146] |
| CrFeMoV | Magnetic properties | Huang et al. [146] |
| CrFeMoW | Elastic properties | Tian et al. [198] |
| | Magnetic properties | Tian et al. [198] |
| | Phase stability | Tian et al. [198] |
| $CrFe_{1.2}MoW$ | Elastic properties | Tian et al. [198] |
| | Magnetic properties | Tian et al. [198] |
| | Phase stability | Tian et al. [198] |
| CrFeNi | Elastic properties | Ge et al. [103], Zaddach et al. [188], Ye et al. [204] |
| | Finite-$T$ excitations | Ge et al. [103] |
| | Local lattice distortions | Ye et al. [204] |
| | Magnetic properties | Ge et al. [103], Huang et al. [146] |
| | SFE | Zaddach et al. [188] |
| Cr–Fe–Ni | Chemical LRO | Wróbel et al. [159] |
| | Chemical SRO | Wróbel et al. [159] |
| | Magnetic properties | Wróbel et al. [159] |

(*continued on next page*)

**Table 9** (*continued*)

| Alloy | Property | References |
|---|---|---|
| | Phase stability | Wróbel et al. [159] |
| CrFeV | Magnetic properties | Huang et al. [146] |
| CrHfNbTiZr | Elastic properties | Fazakas et al. [189] |
| CrMnMoW | Elastic properties | Tian et al. [198] |
| | Magnetic properties | Tian et al. [198] |
| | Phase stability | Tian et al. [198] |
| CrMnTiV | Magnetic properties | Huang et al. [146] |
| CrMnV | Magnetic properties | Huang et al. [146] |
| Cr–Mo | Phase stability | Feng et al. [138] |
| CrMoNbV | Chemical SRO | Widom [184], Feng and Widom [202] |
| | Elastic properties | Feng and Widom [202] |
| | Finite-*T* excitations | Widom [184] |
| | Local lattice distortions | Widom [184], Feng and Widom [202] |
| | Magnetic properties | Huang et al. [146] |
| Cr–Mo–Nb–V | Finite-*T* excitations | Feng et al. [138] |
| | Phase stability | Feng et al. [138] |
| CrMoNiW | Elastic properties | Tian et al. [198] |
| | Magnetic properties | Tian et al. [198] |
| | Phase stability | Tian et al. [198] |
| CrMoTi | Elastic properties | Ge et al. [196] |
| | Finite-*T* excitations | Ge et al. [196] |
| | Magnetic properties | Huang et al. [146] |
| CrMoTiV | Elastic properties | Ge et al. [196] |
| | Finite-*T* excitations | Ge et al. [196] |
| | Magnetic properties | Huang et al. [146] |
| CrMoW | Elastic properties | Tian et al. [198] |
| | Magnetic properties | Tian et al. [198] |
| | Phase stability | Tian et al. [198] |
| CrNi | Local lattice distortions | Chen et al. [113] |
| | Phase stability | Chen et al. [113] |
| | Point defects | Chen et al. [113] |
| $Cr_{0.2}Ni_{0.8}$ | Finite-*T* excitations | Jin et al. [127] |
| | Point defects | Zhao et al. [35] |
| Cr–Ni | Chemical LRO | Wróbel et al. [159] |
| | Chemical SRO | Wróbel et al. [159] |
| | Magnetic properties | Wróbel et al. [159] |
| | Phase stability | Wróbel et al. [159] |
| CrW | Chemical SRO | Lederer et al. [164] |
| CuNi | Phase stability | Singh et al. [156] |
| CuNiPPdPt | Chemical SRO | Gao and Alman [220] |
| | Diffusion | Gao and Alman [220] |
| | Local lattice distortions | Gao and Alman [220] |
| $Cu_2NiZn$ | Chemical LRO | Singh et al. [156] |
| | Phase stability | Singh et al. [156] |

(*continued on next page*)

**Table 9** (*continued*)

| Alloy | Property | References |
|---|---|---|
| CuZr | Local lattice distortions | Egami et al. [221] |
| FeMnNi | Finite-*T* excitations | Niu et al. [235] |
| | Local lattice distortions | Okamoto et al. [224] |
| | Magnetic properties | Wu et al. [33], Huang et al. [146], Niu et al. [235] |
| | Phase stability | Niu et al. [235] |
| FeMnV | Magnetic properties | Huang et al. [146] |
| FeNi | Elastic properties | Ge et al. [103], Ye et al. [204] |
| | Finite-*T* excitations | Ge et al. [103], Zhao et al. [106], Jin et al. [127] |
| | Local lattice distortions | Chen et al. [113], Ye et al. [204] |
| | Magnetic properties | Wu et al. [33], Ge et al. [103], Jin et al. [241] |
| | Phase stability | Chen et al. [113] |
| | Point defects | Zhao et al. [35], Chen et al. [113] |
| | SFE | Zhao et al. [106] |
| $Fe_{0.2}Ni_{0.8}$ | Point defects | Zhao et al. [35] |
| Fe–Ni | Chemical LRO | Wróbel et al. [159] |
| | Chemical SRO | Wróbel et al. [159] |
| | Magnetic properties | Wróbel et al. [159] |
| | Phase stability | Wróbel et al. [159] |
| HfMoNbTaTiZr | Elastic properties | Zheng et al. [205] |
| | Local lattice distortions | Zheng et al. [205] |
| HfMoTaTiZr | Phonon spectrum | Körmann et al. [122] |
| HfNbTaTiVZr | Chemical SRO | Gao et al. [222] |
| | Local lattice distortions | Gao et al. [222] |
| HfNbTaTiZr | Chemical SRO | Gao and Alman [220] |
| | Diffusion | Gao and Alman [220] |
| | Elastic properties | Song et al. [69], Fazakas et al. [189], Li et al. [192], Zheng et al. [205] |
| | Local lattice distortions | Song et al. [69], Zheng et al. [205], Gao and Alman [220] |
| $Hf_{0.080}Nb_{0.308}Ta_{0.308}Ti_{0.177}Zr_{0.127}$ | Phase stability | Heidelmann et al. [246] |
| $Hf_{0.151}Nb_{0.069}Ta_{0.206}Ti_{0.046}Zr_{0.528}$ | Phase stability | Heidelmann et al. [246] |
| HfNbTaZr | Chemical SRO | Feng and Widom [202] |
| | Elastic properties | Feng and Widom [202] |
| | Local lattice distortions | Feng and Widom [202] |
| | Phase stability | Niu et al. [174] |
| HfNbTiVZr | Elastic properties | Fazakas et al. [189], Li et al. [193], Li [200] |
| | Phase stability | Li et al. [193] |
| HfNbTiZr | Chemical SRO | Wang et al. [216] |
| | Elastic properties | Song et al. [69], Li et al. [193] |
| | Local lattice distortions | Song et al. [69] |
| | Phase stability | Li et al. [193] |
| HfNbZr | Elastic properties | Song et al. [69], Fazakas et al. [189], Li et al. [193] |
| | Local lattice distortions | Song et al. [69] |
| | Phase stability | Li et al. [193] |
| | Phonon spectrum | Körmann et al. [122] |
| HfScTiZr | Elastic properties | Rogal et al. [206] |
| HfZr | Phase stability | Niu et al. [174] |

(*continued on next page*)

**Table 9** (*continued*)

| Alloy | Property | References |
|---|---|---|
| MoNb | Chemical LRO | Wang et al. [121], Schön et al. [168] |
| | Elastic properties | Wang et al. [121] |
| | Finite-*T* excitations | Wang et al. [121] |
| | Phase stability | Wang et al. [121], Schön et al. [168] |
| Mo–Nb | Phase stability | Huhn and Widom [135] |
| MoNbReTa | Phase stability | Wu et al. [33] |
| MoNbTa | Chemical LRO | Wang et al. [121], Schön et al. [168] |
| | Elastic properties | Wang et al. [121] |
| | Finite-*T* excitations | Wang et al. [121] |
| | Phase stability | Troparevsky et al. [68], Wang et al. [121], Schön et al. [168] |
| | Phonon spectrum | Körmann et al. [122] |
| MoNbTaTiV | Elastic properties | Yao et al. [203], Zheng et al. [205] |
| | Local lattice distortions | Zheng et al. [205] |
| | Phase stability | Yao et al. [203] |
| MoNbTaV | Chemical LRO | Wang et al. [121], Schön et al. [168] |
| | Chemical SRO | Toda-Caraballo et al. [32, 158] |
| | Elastic properties | Wang et al. [121] |
| | Finite-*T* excitations | Wang et al. [121] |
| | Local lattice distortions | Toda-Caraballo et al. [158] |
| | Phase stability | Wang et al. [121], Toda-Caraballo et al. [158], Schön et al. [168] |
| MoNbTaVW | Chemical LRO | Wang et al. [121], Schön et al. [168] |
| | Chemical SRO | Toda-Caraballo et al. [32, 158], Fernández-Caballero et al. [162], Schön et al. [168] |
| | Elastic properties | Wang et al. [121], Fazakas et al. [189], Zheng et al. [205] |
| | Finite-*T* excitations | Wang et al. [121] |
| | Local lattice distortions | Wu et al. [33], Toda-Caraballo et al. [158], Zheng et al. [205] |
| | Phase stability | Wu et al. [33], Wang et al. [121], Toda-Caraballo et al. [158], Schön et al. [168] |
| | Phonon spectrum | Körmann et al. [122] |
| MoNbTaW | Chemical LRO | Körmann and Sluiter [102], Wang et al. [121], Huhn and Widom [135], Huhn [136], Körmann et al. [163], Schön et al. [168], Singh et al. [169] |
| | Chemical SRO | Toda-Caraballo et al. [32], Huhn and Widom [135], Huhn [136], Widom et al. [137], Toda-Caraballo et al. [158], Körmann et al. [163], Singh et al. [169], Feng and Widom [202], Wang et al. [216] |
| | Elastic properties | Körmann and Sluiter [102], Wang et al. [121], Fazakas et al. [189], Li [200], Feng and Widom [202], Wang et al. [247] |
| | Finite-*T* excitations | Gao et al. [24, 25], Körmann and Sluiter [102], Wang et al. [121] |
| | Local lattice distortions | Körmann and Sluiter [102], Huhn and Widom [135], Widom et al. [137], Toda-Caraballo et al. [158], Feng and Widom [202] |
| | Phase stability | Gao et al. [24, 25], Wu et al. [33], Körmann and Sluiter [102], Wang et al. [121], Huhn and Widom [135], Huhn [136], Toda-Caraballo et al. [158], Körmann et al. [163], Schön et al. [168], Singh et al. [169], Wang et al. [247] |
| | Phonon spectrum | Körmann et al. [122] |
| Mo–Nb–Ta–W | Chemical SRO | Singh et al. [169] |
| | Phase stability | Singh et al. [169] |
| MoNbTi | Elastic properties | Ge et al. [196] |
| | Finite-*T* excitations | Ge et al. [196] |
| | Magnetic properties | Huang et al. [146] |
| MoNbTiV | Elastic properties | Cao et al. [191], Tian et al. [195], Ge et al. [196], Li [200] |
| | Finite-*T* excitations | Ge et al. [196] |

(*continued on next page*)

**Table 9** (*continued*)

| Alloy | Property | References |
|---|---|---|
| | Magnetic properties | Huang et al. [146] |
| | Phase stability | Cao et al. [191] |
| MoNbTiVZr | Elastic properties | Tian et al. [199], Zheng et al. [205] |
| | Local lattice distortions | Tian et al. [199], Zheng et al. [205] |
| | Phase stability | Tian et al. [199] |
| $MoNbTiV_xZr$ | Elastic properties | Tian et al. [190] |
| MoNbTiZr | Elastic properties | Tian et al. [190, 199] |
| | Local lattice distortions | Tian et al. [199] |
| | Phase stability | Tian et al. [199] |
| MoNbV | Chemical LRO | Wang et al. [121], Schön et al. [168] |
| | Elastic properties | Wang et al. [121], Ge et al. [196] |
| | Finite-*T* excitations | Wang et al. [121], Ge et al. [196] |
| | Magnetic properties | Huang et al. [146] |
| | Phase stability | Wang et al. [121], Schön et al. [168] |
| MoNbVW | Chemical LRO | Wang et al. [121], Schön et al. [168] |
| | Chemical SRO | Toda-Caraballo et al. [32, 158], Fernández-Caballero et al. [162], Wang et al. [216] |
| | Elastic properties | Wang et al. [121, 247] |
| | Finite-*T* excitations | Wang et al. [121] |
| | Local lattice distortions | Toda-Caraballo et al. [158] |
| | Phase stability | Wang et al. [121], Toda-Caraballo et al. [158], Schön et al. [168], Wang et al. [247] |
| MoNbW | Chemical LRO | Wang et al. [121], Schön et al. [168] |
| | Elastic properties | Wang et al. [121] |
| | Finite-*T* excitations | Wang et al. [121] |
| | Phase stability | Wang et al. [121], Schön et al. [168] |
| MoTa | Chemical LRO | Wang et al. [121], Schön et al. [168] |
| | Elastic properties | Wang et al. [121] |
| | Finite-*T* excitations | Wang et al. [121] |
| | Phase stability | Wang et al. [121], Schön et al. [168] |
| | Phonon spectrum | Körmann et al. [122] |
| Mo–Ta | Phase stability | Huhn and Widom [135] |
| $Mo_xTaTiWZr$ | Phase stability | Singh et al. [170] |
| $Mo_{x/2}Ta_yTi_{z/2}W_{x/2}Zr_{z/2}$ | Chemical SRO | Singh et al. [170] |
| | Elastic properties | Singh et al. [170] |
| | Phase stability | Singh et al. [170] |
| $Mo_xTa_yTi_{z/2}Zr_{z/2}$ | Elastic properties | Singh et al. [170] |
| | Phase stability | Singh et al. [170] |
| MoTaV | Chemical LRO | Wang et al. [121], Schön et al. [168] |
| | Elastic properties | Wang et al. [121] |
| | Finite-*T* excitations | Wang et al. [121] |
| | Phase stability | Wang et al. [121], Schön et al. [168] |
| MoTaVW | Chemical LRO | Wang et al. [121], Schön et al. [168] |
| | Chemical SRO | Toda-Caraballo et al. [32, 158], Fernández-Caballero et al. [162], Wang et al. [216] |
| | Elastic properties | Wang et al. [121, 247] |
| | Finite-*T* excitations | Wang et al. [121] |
| | Local lattice distortions | Toda-Caraballo et al. [158] |
| | Phase stability | Wang et al. [121], Toda-Caraballo et al. [158], Schön et al. [168], Wang et al. [247] |

(*continued on next page*)

**Table 9** (*continued*)

| Alloy | Property | References |
|---|---|---|
| MoTaW | Chemical LRO | Wang et al. [121], Schön et al. [168] |
| | Elastic properties | Wang et al. [121] |
| | Finite-*T* excitations | Wang et al. [121] |
| | Phase stability | Wang et al. [121], Schön et al. [168] |
| MoTiV | Elastic properties | Ge et al. [196] |
| | Finite-*T* excitations | Ge et al. [196] |
| | Magnetic properties | Huang et al. [146] |
| MoV | Chemical LRO | Wang et al. [121], Schön et al. [168] |
| | Elastic properties | Wang et al. [121] |
| | Finite-*T* excitations | Wang et al. [121] |
| | Phase stability | Wang et al. [121], Schön et al. [168] |
| MoVW | Chemical LRO | Wang et al. [121], Schön et al. [168] |
| | Elastic properties | Wang et al. [121] |
| | Finite-*T* excitations | Wang et al. [121] |
| | Phase stability | Wang et al. [121], Schön et al. [168] |
| MoW | Chemical LRO | Wang et al. [121], Schön et al. [168] |
| | Elastic properties | Wang et al. [121] |
| | Finite-*T* excitations | Wang et al. [121] |
| | Phase stability | Wang et al. [121], Schön et al. [168] |
| Mo–W | Phase stability | Huhn and Widom [135] |
| NbTa | Chemical LRO | Wang et al. [121], Schön et al. [168] |
| | Elastic properties | Wang et al. [121] |
| | Finite-*T* excitations | Wang et al. [121] |
| | Phase stability | Wang et al. [121], Schön et al. [168] |
| Nb–Ta | Phase stability | Huhn and Widom [135] |
| NbTaTiV | Phonon spectrum | Körmann et al. [122] |
| NbTaTiVW | Elastic properties | Zheng et al. [205] |
| | Local lattice distortions | Zheng et al. [205] |
| | Phonon spectrum | Körmann et al. [122] |
| NbTaV | Chemical LRO | Wang et al. [121], Schön et al. [168] |
| | Elastic properties | Wang et al. [121] |
| | Finite-*T* excitations | Wang et al. [121] |
| | Phase stability | Wang et al. [121], Schön et al. [168] |
| NbTaVW | Chemical LRO | Wang et al. [121], Schön et al. [168] |
| | Chemical SRO | Toda-Caraballo et al. [32, 158] |
| | Elastic properties | Wang et al. [121] |
| | Finite-*T* excitations | Wang et al. [121] |
| | Local lattice distortions | Toda-Caraballo et al. [158] |
| | Phase stability | Wang et al. [121], Toda-Caraballo et al. [158], Schön et al. [168] |
| | Phonon spectrum | Körmann et al. [122] |
| NbTaW | Chemical LRO | Wang et al. [121], Schön et al. [168] |
| | Elastic properties | Wang et al. [121] |
| | Finite-*T* excitations | Wang et al. [121] |
| | Phase stability | Wang et al. [121], Schön et al. [168] |
| NbTiV | Elastic properties | Song et al. [69] |
| | Local lattice distortions | Song et al. [69] |
| | Magnetic properties | Huang et al. [146] |
| NbTiVZr | Chemical SRO | Widom [184], Feng and Widom [202] |
| | Elastic properties | Li et al. [193], Tian et al. [199], Li [200], Feng and Widom [202] |
| | Finite-*T* excitations | Widom [184] |

(*continued on next page*)

**Table 9** (*continued*)

| Alloy | Property | References |
|---|---|---|
| | Local lattice distortions | Widom [184], Tian et al. [199], Feng and Widom [202] |
| | Phase stability | Li et al. [193], Tian et al. [199] |
| NbV | Chemical LRO | Wang et al. [121], Schön et al. [168] |
| | Elastic properties | Wang et al. [121] |
| | Finite-*T* excitations | Wang et al. [121] |
| | Phase stability | Wang et al. [121], Schön et al. [168] |
| Nb–V | Phase stability | Feng et al. [138] |
| NbVW | Chemical LRO | Wang et al. [121], Schön et al. [168] |
| | Elastic properties | Wang et al. [121] |
| | Finite-*T* excitations | Wang et al. [121] |
| | Phase stability | Wang et al. [121], Schön et al. [168] |
| | Phonon spectrum | Körmann et al. [122] |
| NbW | Chemical LRO | Wang et al. [121], Schön et al. [168] |
| | Chemical SRO | Lederer et al. [164] |
| | Elastic properties | Wang et al. [121] |
| | Finite-*T* excitations | Wang et al. [121] |
| | Phase stability | Wang et al. [121], Schön et al. [168] |
| Nb–W | Phase stability | Huhn and Widom [135] |
| NbZr | Phase stability | Li et al. [193] |
| NiPd | Finite-*T* excitations | Zhao et al. [106] |
| | Magnetic properties | Wu et al. [33] |
| | SFE | Zhao et al. [106] |
| NiPdPt | Chemical SRO | Khan et al. [160] |
| | Magnetic properties | Khan et al. [160] |
| $Ta_yTi_{z/2}W_xZr_{z/2}$ | Elastic properties | Singh et al. [170] |
| | Phase stability | Singh et al. [170] |
| TaV | Chemical LRO | Wang et al. [121], Schön et al. [168] |
| | Elastic properties | Wang et al. [121] |
| | Finite-*T* excitations | Wang et al. [121] |
| | Phase stability | Wang et al. [121], Schön et al. [168] |
| TaVW | Chemical LRO | Wang et al. [121], Schön et al. [168] |
| | Elastic properties | Wang et al. [121] |
| | Finite-*T* excitations | Wang et al. [121] |
| | Phase stability | Wang et al. [121], Schön et al. [168] |
| | Phonon spectrum | Körmann et al. [122] |
| TaW | Chemical LRO | Wang et al. [121], Schön et al. [168] |
| | Elastic properties | Wang et al. [121] |
| | Finite-*T* excitations | Wang et al. [121] |
| | Phase stability | Wang et al. [121], Schön et al. [168] |
| Ta–W | Chemical LRO | Singh et al. [169] |
| | Chemical SRO | Singh et al. [169] |
| | Phase stability | Huhn and Widom [135], Singh et al. [169, 170] |
| TiV | Phase stability | Li et al. [193] |
| VW | Chemical LRO | Wang et al. [121], Schön et al. [168] |
| | Elastic properties | Wang et al. [121] |
| | Finite-*T* excitations | Wang et al. [121] |
| | Phase stability | Wang et al. [121], Schön et al. [168] |
| | Phonon spectrum | Körmann et al. [122] |

## References


[1] J.-W. Yeh, Alloy design strategies and future trends in high-entropy alloys, JOM 65 (2013) 1759–1771, https://doi.org/10.1007/s11837-013-0761-6.
[2] B.S. Murty, J.W. Yeh, S. Ranganathan, High-entropy Alloys, Butterworth-Heinemann, 2014, https://doi.org/10.1016/b978-0-12-800251-3.00011-0.
[3] M.C. Gao, J.-W. Yeh, P.K. Liaw, Y. Zhang, High-entropy Alloys: Fundamentals and Applications, Springer, 2016, https://doi.org/10.1007/978-3-319-27013-5.
[4] J.W. Yeh, Y.L. Chen, S.J. Lin, S.K. Chen, High-entropy alloys—a new era of exploitation, Materials Science Forum, vol. 560, Trans Tech Publ, 2007, pp. 1–9, https://doi.org/10.4028/www.scientific.net/MSF.560.1.
[5] J.-W. Yeh, S.-K. Chen, S.-J. Lin, J.-Y. Gan, T.-S. Chin, T.-T. Shun, C.-H. Tsau, S.-Y. Chang, Nanostructured high-entropy alloys with multiple principal elements: novel alloy design concepts and outcomes, Adv. Eng. Mater. 6 (2004) 299–303, https://doi.org/10.1002/adem.200300567.
[6] B. Cantor, I. Chang, P. Knight, A. Vincent, Microstructural development in equiatomic multicomponent alloys, Mater. Sci. Eng., A 375 (2004) 213–218, https://doi.org/10.1016/j.msea.2003.10.257.
[7] J.-W. Yeh, Recent progress in high entropy alloys, Ann. Chim. Sci. Mat. 31 (2006) 633–648, https://doi.org/10.3166/acsm.31.633-648.
[8] S. Guo, C.T. Liu, Phase stability in high entropy alloys: formation of solid-solution phase or amorphous phase, Prog. Nat. Sci. Mater. Int. 21 (2011) 433–446, https://doi.org/10.1016/S1002-0071(12)60080-X.
[9] Y. Zhang, X. Yang, P. Liaw, Alloy design and properties optimization of high-entropy alloys, JOM 64 (2012) 830–838, https://doi.org/10.1007/s11837-012-0366-5.
[10] M.-H. Tsai, Physical properties of high entropy alloys, Entropy 15 (2013) 5338–5345, https://doi.org/10.3390/e15125338.
[11] B. Cantor, Multicomponent and high entropy alloys, Entropy 16 (2014) 4749–4768, https://doi.org/10.3390/e16094749.
[12] M.-H. Tsai, J.-W. Yeh, High-entropy alloys: a critical review, Mater. Res. Lett. 2 (2014) 107–123, https://doi.org/10.1080/21663831.2014.912690.
[13] Y. Zhang, T.T. Zuo, Z. Tang, M.C. Gao, K.A. Dahmen, P.K. Liaw, Z.P. Lu, Microstructures and properties of high-entropy alloys, Prog. Mater. Sci. 61 (2014) 1–93, https://doi.org/10.1016/j.pmatsci.2013.10.001.
[14] H. Diao, L.J. Santodonato, Z. Tang, T. Egami, P.K. Liaw, Local structures of high-entropy alloys (HEAs) on atomic scales: an overview, JOM 67 (2015) 2321–2325, https://doi.org/10.1007/s11837-015-1591-5.
[15] R. Kozak, A. Sologubenko, W. Steurer, Single-phase high-entropy alloys: an overview, Z. Kristallogr. Cryst. Mater. 230 (2015) 55–68, https://doi.org/10.1515/zkri-2014-1739.
[16] Z. Lu, H. Wang, M. Chen, I. Baker, J. Yeh, C. Liu, T. Nieh, An assessment on the future development of high-entropy alloys: summary from a recent workshop, Intermetallics 66 (2015) 67–76, https://doi.org/10.1016/j.intermet.2015.06.021.
[17] M.C. Troparevsky, J.R. Morris, M. Daene, Y. Wang, A.R. Lupini, G.M. Stocks, Beyond atomic sizes and Hume-Rothery rules: understanding and predicting high-entropy alloys, JOM 67 (2015) 2350–2363, https://doi.org/10.1007/s11837-015-1594-2.
[18] D. Raabe, C.C. Tasan, H. Springer, M. Bausch, From high-entropy alloys to high-entropy steels, Steel Res. Int. 86 (2015) 1127–1138, https://doi.org/10.1002/srin.201500133.
[19] J.-W. Yeh, Physical metallurgy of high-entropy alloys, JOM 67 (2015) 2254–2261, https://doi.org/10.1007/s11837-015-1583-5.
[20] E. Pickering, N. Jones, High-entropy alloys: a critical assessment of their founding principles and future prospects, Int. Mater. Rev. 61 (2016) 183–202, https://doi.org/10.1080/09506608.2016.1180020.
[21] M.-H. Tsai, Three strategies for the design of advanced high-entropy alloys, Entropy 18 (2016) 252, https://doi.org/10.3390/e18070252.
[22] Y. Ye, Q. Wang, J. Lu, C. Liu, Y. Yang, High-entropy alloy: challenges and prospects, Mater. Today 19 (2016) 349–362, https://doi.org/10.1016/j.mattod.2015.11.026.
[23] H. Diao, R. Feng, K. Dahmen, P. Liaw, Fundamental deformation behavior in high-entropy alloys: an overview, Curr. Opin. Solid State Mater. Sci. 21 (2017) 252–266, https://doi.org/10.1016/j.cossms.2017.08.003.
[24] M. Gao, C. Zhang, P. Gao, F. Zhang, L. Ouyang, M. Widom, J. Hawk, Thermodynamics of concentrated solid solution alloys, Curr. Opin. Solid State Mater. Sci. 21 (2017) 238–251, https://doi.org/10.1016/j.cossms.2017.08.001.
[25] M.C. Gao, P. Gao, J.A. Hawk, L. Ouyang, D.E. Alman, M. Widom, Computational modeling of high-entropy alloys: structures, thermodynamics and elasticity, J. Mater. Res. 32 (2017) 3627–3641, https://doi.org/10.1557/jmr.2017.366.
[26] Z. Li, D. Raabe, Strong and ductile non-equiatomic high-entropy alloys: design, processing, microstructure, and mechanical properties, JOM 69 (2017) 2099–2106, https://doi.org/10.1007/s11837-017-2540-2.
[27] D.B. Miracle, High-entropy alloys: a current evaluation of founding ideas and core effects and exploring “nonlinear alloys”, JOM 69 (2017) 2130–2136, https://doi.org/10.1007/s11837-017-2527-z.
[28] D. Miracle, O. Senkov, A critical review of high entropy alloys and related concepts, Acta Mater. 122 (2017) 448–511, https://doi.org/10.1016/j.actamat.2016.08.081.
[29] Y. Qiu, S. Thomas, M.A. Gibson, H.L. Fraser, N. Birbilis, Corrosion of high entropy alloys, npj Mater. Degrad. 1 (2017) 15, https://doi.org/10.1038/s41529-017-0009-y.
[30] Y. Shi, B. Yang, P.K. Liaw, Corrosion-resistant high-entropy alloys: a review, Metals 7 (2017) 43, https://doi.org/10.3390/met7020043.
[31] F. Tian, A review of solid-solution models of high-entropy alloys based on *ab initio* calculations, Front. Mater. 4 (2017) 36, https://doi.org/10.3389/fmats.2017.00036.
[32] I. Toda-Caraballo, J.S. Wróbel, D. Nguyen-Manh, P. Pérez, P.E.J. Rivera-Díaz-del Castillo, Simulation and modeling in high entropy alloys, JOM 69 (2017) 2137–2149, https://doi.org/10.1007/s11837-017-2524-2.
[33] Z. Wu, M.C. Troparevsky, Y.F. Gao, J.R. Morris, G.M. Stocks, H. Bei, Phase stability, physical properties and strengthening mechanisms of concentrated solid solution alloys, Curr. Opin. Solid State Mater. Sci. 21 (2017) 267–284, https://doi.org/10.1016/j.cossms.2017.07.001.
[34] Y. Zhang, S. Zhao, W.J. Weber, K. Nordlund, F. Granberg, F. Djurabekova, Atomic-level heterogeneity and defect dynamics in concentrated solid-solution alloys, Curr. Opin. Solid State Mater. Sci. 21 (2017) 221–237, https://doi.org/10.1016/j.cossms.2017.02.002.
[35] S. Zhao, W.J. Weber, Y. Zhang, Unique challenges for modeling defect dynamics in concentrated solid-solution alloys, JOM 69 (2017) 2084–2091, https://doi.org/10.1007/s11837-017-2461-0.
[36] P. Chen, C. Lee, S.-Y. Wang, M. Seifi, J.J. Lewandowski, K.A. Dahmen, H. Jia, X. Xie, B. Chen, J.-W. Yeh, C.-W. Tsai, T. Yuan, P.K. Liaw, Fatigue behavior of high-entropy alloys: a review, Sci. China Technol. Sci. 61 (2018) 168–178, https://doi.org/10.1007/s11431-017-9137-4.
[37] S. Praveen, H.S. Kim, High-entropy alloys: potential candidates for high-temperature applications — an overview, Adv. Eng. Mater. 20 (2018) 1700645, https://doi.org/10.1002/adem.201700645.
[38] O. N. Senkov, D. B. Miracle, K. J. Chaput, J.-P. Couzinie, Development and exploration of refractory high entropy alloys—a review, J. Mater. Res. http://10.1557/jmr.2018.153, in press.
[39] W. Zhang, P.K. Liaw, Y. Zhang, Science and technology in high-entropy alloys, Sci. China Mater. 61 (2018) 2–22, https://doi.org/10.1007/s40843-017-9195-8.
[40] P. Hohenberg, W. Kohn, Inhomogeneous electron gas, Phys. Rev. 136 (1964) B864–B871, https://doi.org/10.1103/PhysRev.136.B864.
[41] W. Kohn, L.J. Sham, Self-consistent equations including exchange and correlation effects, Phys. Rev. 140 (1965) A1133–A1138, https://doi.org/10.1103/PhysRev.140.A1133.
[42] J. Hafner, C. Wolverton, G. Ceder, Toward computational materials design: the impact of density functional theory on materials research, MRS Bull. 31 (2006) 659–668, https://doi.org/10.1557/mrs2006.174.
[43] E.K. Gross, R.M. Dreizler, Density Functional Theory, 337 Springer Science & Business Media, 2013, https://doi.org/10.1007/978-1-4757-9975-0.
[44] D.M. Ceperley, B. Alder, Ground state of the electron gas by a stochastic method, Phys. Rev. Lett. 45 (1980) 566–569, https://doi.org/10.1103/PhysRevLett.45.566.
[45] J.P. Perdew, Density-functional approximation for the correlation energy of the inhomogeneous electron gas, Phys. Rev. B 33 (1986) 8822–8824, https://doi.org/10.1103/PhysRevB.33.8822.
[46] J.P. Perdew, J.A. Chevary, S.H. Vosko, K.A. Jackson, M.R. Pederson, D.J. Singh, C. Fiolhais, Atoms, molecules, solids, and surfaces: applications of the generalized gradient approximation for exchange and correlation, Phys. Rev. B 46 (1992) 6671–6687, https://doi.org/10.1103/PhysRevB.46.6671.
[47] J.P. Perdew, K. Burke, M. Ernzerhof, Generalized gradient approximation made simple, Phys. Rev. Lett. 77 (1996) 3865–3868, https://doi.org/10.1103/PhysRevLett.77.3865.
[48] B. Grabowski, T. Hickel, J. Neugebauer, *Ab initio* study of the thermodynamic properties of nonmagnetic elementary fcc metals: exchange-correlation-related error bars and chemical trends, Phys. Rev. B 76 (2007) 024309, https://doi.org/10.1103/PhysRevB.76.024309.
[49] F. Körmann, A. Dick, T. Hickel, J. Neugebauer, Pressure dependence of the Curie temperature in bcc iron studied by *ab initio* simulations, Phys. Rev. B 79 (2009) 184406, https://doi.org/10.1103/PhysRevB.79.184406.
[50] L. Zhou, F. Körmann, D. Holec, M. Bartosik, B. Grabowski, J. Neugebauer, P.H. Mayrhofer, Structural stability and thermodynamics of CrN magnetic phases from *ab initio* calculations and experiment, Phys. Rev. B 90 (2014) 184102, https://doi.org/10.1103/PhysRevB.90.184102.
[51] L.-F. Zhu, B. Grabowski, J. Neugebauer, Efficient approach to compute melting properties fully from *ab initio* with application to Cu, Phys. Rev. B 96 (2017) 224202, https://doi.org/10.1103/PhysRevB.96.224202.
[52] U. von Barth, L. Hedin, A local exchange-correlation potential for the spin polarized case. I, J. Phys. C. 5 (1972) 1629–1642, https://doi.org/10.1088/0022-3719/5/13/012.
[53] C. Wang, B. Klein, H. Krakauer, Theory of magnetic and structural ordering in iron, Phys. Rev. Lett. 54 (1985) 1852–1855, https://doi.org/10.1103/PhysRevLett.54.1852.
[54] L. Kaufman, H. Bernstein, Computer Calculation of Phase Diagrams, Academic Press, Inc., New York, 1970.
[55] M. Hillert, Phase Equilibria, Phase Diagrams and Phase Transformations: Their Thermodynamic Basis, 2, Cambridge University Press, 2007, https://doi.org/10.1017/CBO9780511812781.
[56] N. Saunders, A.P. Miodownik, Calphad (Calculation of Phase Diagrams): A Comprehensive Guide, Pergamon, Oxford, New York, 1998http://www.sciencedirect.com/science/bookseries/14701804/1.
[57] A.V. Ruban, I.A. Abrikosov, Configurational thermodynamics of alloys from first principles: effective cluster interactions, Rep. Prog. Phys. 71 (2008) 046501, https://doi.org/10.1088/0034-4885/71/4/046501.
[58] J. Cao, B.J. Berne, A Born-Oppenheimer approximation for path integrals with an application to electron solvation in polarizable fluids, J. Chem. Phys. 99 (1993) 2902–2916, https://doi.org/10.1063/1.465198.
[59] F. Körmann, A. Dick, B. Grabowski, B. Hallstedt, T. Hickel, J. Neugebauer, Free

energy of bcc iron: integrated *ab initio* derivation of vibrational, electronic, and magnetic contributions, Phys. Rev. B 78 (2008) 033102, https://doi.org/10.1103/PhysRevB.78.033102.
[60] B. Grabowski, T. Hickel, J. Neugebauer, Formation energies of point defects at finite temperatures, Phys. Status Solidi B 248 (2011) 1295–1308, https://doi.org/10.1002/pssb.201046302.
[61] B. Alling, F. Körmann, B. Grabowski, A. Glensk, I.A. Abrikosov, J. Neugebauer, Strong impact of lattice vibrations on electronic and magnetic properties of paramagnetic Fe revealed by disordered local moments molecular dynamics, Phys. Rev. B 93 (2016) 224411, https://doi.org/10.1103/PhysRevB.93.224411.
[62] X. Zhang, B. Grabowski, F. Körmann, C. Freysoldt, J. Neugebauer, Accurate electronic free energies of the 3*d*,4*d*, and 5*d* transition metals at high temperatures, Phys. Rev. B 95 (2017) 165126, https://doi.org/10.1103/PhysRevB.95.165126.
[63] B. Grabowski, L. Ismer, T. Hickel, J. Neugebauer, *Ab initio* up to the melting point: anharmonicity and vacancies in aluminum, Phys. Rev. B 79 (2009) 134106, https://doi.org/10.1103/PhysRevB.79.134106.
[64] F. Körmann, T. Hickel, J. Neugebauer, Influence of magnetic excitations on the phase stability of metals and steels, Curr. Opin. Solid State Mater. Sci. 20 (2016) 77–84, https://doi.org/10.1016/j.cossms.2015.06.001.
[65] X. Zhang, B. Grabowski, T. Hickel, J. Neugebauer, Calculating free energies of point defects from *ab initio*, Comput. Mater. Sci. 148 (2018) 249–259, https://doi.org/10.1016/j.commatsci.2018.02.042.
[66] L. Rogal, P. Bobrowski, F. Körmann, S. Divinski, F. Stein, B. Grabowski, Computational engineering of sublattice ordering in a hexagonal AlHfScTiZr high entropy alloy, Sci. Rep. 7 (2017) 2209, https://doi.org/10.1038/s41598-017-02385-w.
[67] F. Otto, Y. Yang, H. Bei, E. George, Relative effects of enthalpy and entropy on the phase stability of equiatomic high-entropy alloys, Acta Mater. 61 (2013) 2628–2638, https://doi.org/10.1016/j.actamat.2013.01.042.
[68] M.C. Troparevsky, J.R. Morris, P.R.C. Kent, A.R. Lupini, G.M. Stocks, Criteria for predicting the formation of single-phase high-entropy alloys, Phys. Rev. X 5 (2015) 011041, https://doi.org/10.1103/PhysRevX.5.011041.
[69] H. Song, F. Tian, Q.-M. Hu, L. Vitos, Y. Wang, J. Shen, N. Chen, Local lattice distortion in high-entropy alloys, Phys. Rev. Mater. 1 (2017) 023404, https://doi.org/10.1103/PhysRevMaterials.1.023404.
[70] F. Tian, L. Delczeg, N. Chen, L.K. Varga, J. Shen, L. Vitos, Structural stability of $NiCoFeCrAl_x$ high-entropy alloy from *ab initio* theory, Phys. Rev. B 88 (2013) 085128, https://doi.org/10.1103/PhysRevB.88.085128.
[71] W.-R. Wang, W.-L. Wang, S.-C. Wang, Y.-C. Tsai, C.-H. Lai, J.-W. Yeh, Effects of Al addition on the microstructure and mechanical property of $Al_xCoCrFeNi$ high-entropy alloys, Intermetallics 26 (2012) 44–51, https://doi.org/10.1016/j.intermet.2012.03.005.
[72] X. Sun, H. Zhang, S. Lu, X. Ding, Y. Wang, L. Vitos, Phase selection rule for Al-doped CrMnFeCoNi high-entropy alloys from first-principles, Acta Mater. 140 (2017) 366–374, https://doi.org/10.1016/j.actamat.2017.08.045.
[73] M. Schick, B. Hallstedt, A. Glensk, B. Grabowski, T. Hickel, M. Hampl, J. Gröbner, J. Neugebauer, R. Schmid-Fetzer, Combined *ab initio*, experimental, and CALPHAD approach for an improved thermodynamic evaluation of the Mg–Si system, CALPHAD 37 (2012) 77–86, https://doi.org/10.1016/j.calphad.2012.02.001.
[74] B. Kaplan, D. Korbmacher, A. Blomqvist, B. Grabowski, Finite temperature *ab initio* calculated thermodynamic properties of orthorhombic $Cr_3C_2$, CALPHAD 53 (2016) 72–77, https://doi.org/10.1016/j.calphad.2016.03.006.
[75] A. Zunger, S.-H. Wei, L.G. Ferreira, J.E. Bernard, Special quasirandom structures, Phys. Rev. Lett. 65 (1990) 353–356, https://doi.org/10.1103/PhysRevLett.65.353.
[76] L. Vitos, Total-energy method based on the exact muffin-tin orbitals theory, Phys. Rev. B 64 (2001) 014107, https://doi.org/10.1103/PhysRevB.64.014107.
[77] L. Vitos, I.A. Abrikosov, B. Johansson, Anisotropic lattice distortions in random alloys from first-principles theory, Phys. Rev. Lett. 87 (2001) 156401, https://doi.org/10.1103/PhysRevLett.87.156401.
[78] P.E. Blöchl, Projector augmented-wave method, Phys. Rev. B 50 (1994) 17953–17979, https://doi.org/10.1103/PhysRevB.50.17953.
[79] G. Kresse, J. Furthmüller, Efficiency of ab-initio total energy calculations for metals and semiconductors using a plane-wave basis set, Comp. Mater. Sci. 6 (1996) 15–50, https://doi.org/10.1016/0927-0256(96)00008-0.
[80] G. Kresse, J. Furthmüller, Efficient iterative schemes for *ab initio* total-energy calculations using a plane-wave basis set, Phys. Rev. B 54 (1996) 11169–11186, https://doi.org/10.1103/PhysRevB.54.11169.
[81] L. Vitos, Computational Quantum Mechanics for Materials Engineers: The EMTO Method and Applications, Springer Science & Business Media, 2007, https://doi.org/10.1007/978-1-84628-951-4.
[82] J. Korringa, On the calculation of the energy of a Bloch wave in a metal, Physica 13 (1947) 392–400, https://doi.org/10.1016/0031-8914(47)90013-X.
[83] W. Kohn, N. Rostoker, Solution of the Schrödinger equation in periodic lattices with an application to metallic lithium, Phys. Rev. 94 (1954) 1111, https://doi.org/10.1103/PhysRev.94.1111.
[84] Z. Leong, J.S. Wróbel, S.L. Dudarev, R. Goodall, I. Todd, D. Nguyen-Manh, The effect of electronic structure on the phases present in high entropy alloys, Sci. Rep. 7 (2017) 39803, https://doi.org/10.1038/srep39803.
[85] N.D. Mermin, Thermal properties of the inhomogeneous electron gas, Phys. Rev. 137 (1965) A1441–A1443, https://doi.org/10.1103/PhysRev.137.A1441.
[86] B. Grabowski, P. Söderlind, T. Hickel, J. Neugebauer, Temperature-driven phase transitions from first principles including all relevant excitations: the fcc-to-bcc transition in Ca, Phys. Rev. B 84 (2011) 214107, https://doi.org/10.1103/PhysRevB.84.214107.
[87] F. Körmann, A.A.H. Breidi, S.L. Dudarev, N. Dupin, G. Ghosh, T. Hickel, P. Korzhavyi, J.A. Muñoz, I. Ohnuma, Lambda transitions in materials science: recent advances in CALPHAD and first-principles modelling, Phys. Status Solidi B 251 (2014) 53–80, https://doi.org/10.1002/pssb.201350136.
[88] A.V. Ruban, S. Khmelevskyi, P. Mohn, B. Johansson, Temperature-induced longitudinal spin fluctuations in Fe and Ni, Phys. Rev. B 75 (2007) 054402, https://doi.org/10.1103/PhysRevB.75.054402.
[89] F. Körmann, A. Dick, T. Hickel, J. Neugebauer, Rescaled Monte Carlo approach for magnetic systems: *ab initio* thermodynamics of bcc iron, Phys. Rev. B 81 (2010) 134425, https://doi.org/10.1103/PhysRevB.81.134425.
[90] F. Körmann, A. Dick, T. Hickel, J. Neugebauer, Role of spin quantization in determining the thermodynamic properties of magnetic transition metals, Phys. Rev. B 83 (2011) 165114, https://doi.org/10.1103/PhysRevB.83.165114.
[91] F. Körmann, B. Grabowski, P. Söderlind, M. Palumbo, S.G. Fries, T. Hickel, J. Neugebauer, Thermodynamic modeling of chromium: strong and weak magnetic coupling, J. Phys. Condens. Matter 25 (2013) 425401, https://doi.org/10.1088/0953-8984/25/42/425401.
[92] I.A. Abrikosov, A. Ponomareva, P. Steneteg, S. Barannikova, B. Alling, Recent progress in simulations of the paramagnetic state of magnetic materials, Curr. Opin. Solid State Mater. Sci. 20 (2016) 85–106, https://doi.org/10.1016/j.cossms.2015.07.003.
[93] G. Inden, Approximate description of the configurational specific heat during a magnetic order-disorder transformation, Proceeding of the 5th project meeting CALPHAD, III.4.1–13, 1976.
[94] G. Inden, The role of magnetism in the calculation of phase diagrams, Phys. B + C 103 (1981) 82–100, https://doi.org/10.1016/0378-4363(81)91004-4.
[95] P.-W. Ma, S.L. Dudarev, Constrained density functional for noncollinear magnetism, Phys. Rev. B 91 (2015) 054420, https://doi.org/10.1103/PhysRevB.91.054420.
[96] B. Gyorffy, A. Pindor, J. Staunton, G. Stocks, H. Winter, A first-principles theory of ferromagnetic phase transitions in metals, J. Phys. F 15 (1985) 1337–1386, https://doi.org/10.1088/0305-4608/15/6/018.
[97] V.P. Antropov, M.I. Katsnelson, B.N. Harmon, M. van Schilfgaarde, D. Kusnezov, Spin dynamics in magnets: equation of motion and finite temperature effects, Phys. Rev. B 54 (1996) 1019–1035, https://doi.org/10.1103/PhysRevB.54.1019.
[98] B. Fultz, L. Anthony, J. Robertson, R. Nicklow, S. Spooner, M. Mostoller, Phonon modes and vibrational entropy of mixing in Fe–Cr, Phys. Rev. B 52 (1995) 3280–3285, https://doi.org/10.1103/PhysRevB.52.3280.
[99] B. Fultz, Vibrational thermodynamics of materials, Prog. Mater. Sci. 55 (2010) 247–352, https://doi.org/10.1016/j.pmatsci.2009.05.002.
[100] V.L. Moruzzi, J.F. Janak, K. Schwarz, Calculated thermal properties of metals, Phys. Rev. B 37 (1988) 790–799, https://doi.org/10.1103/PhysRevB.37.790.
[101] D. Ma, B. Grabowski, F. Körmann, J. Neugebauer, D. Raabe, *Ab initio* thermodynamics of the CoCrFeMnNi high entropy alloy: importance of entropy contributions beyond the configurational one, Acta Mater. 100 (2015) 90–97, https://doi.org/10.1016/j.actamat.2015.08.050.
[102] F. Körmann, M. Sluiter, Interplay between lattice distortions, vibrations and phase stability in NbMoTaW high entropy alloys, Entropy 18 (2016) 403, https://doi.org/10.3390/e18080403.
[103] H. Ge, H. Song, J. Shen, F. Tian, Effect of alloying on the thermal-elastic properties of 3d high-entropy alloys, Mater. Chem. Phys. 210 (2018) 320–326, https://doi.org/10.1016/j.matchemphys.2017.10.046.
[104] J.C. Slater, et al., Introduction to Chemical Physics, McGraw-Hill Book Company, Inc., 1939.
[105] J. Dugdale, D. MacDonald, The thermal expansion of solids, Phys. Rev. 89 (1953) 832–834, https://doi.org/10.1103/PhysRev.89.832.
[106] S. Zhao, G.M. Stocks, Y. Zhang, Stacking fault energies of face-centered cubic concentrated solid solution alloys, Acta Mater. 134 (2017) 334–345, https://doi.org/10.1016/j.actamat.2017.05.001.
[107] F. Otto, A. Dlouhý, K.G. Pradeep, M. Kuběnová, D. Raabe, G. Eggeler, E.P. George, Decomposition of the single-phase high-entropy alloy CrMnFeCoNi after prolonged anneals at intermediate temperatures, Acta Mater. 112 (2016) 40–52, https://doi.org/10.1016/j.actamat.2016.04.005.
[108] Z. Li, F. Körmann, B. Grabowski, J. Neugebauer, D. Raabe, *Ab initio* assisted design of quinary dual-phase high-entropy alloys with transformation-induced plasticity, Acta Mater. 136 (2017) 262–270, https://doi.org/10.1016/j.actamat.2017.07.023.
[109] C. Freysoldt, B. Grabowski, T. Hickel, J. Neugebauer, G. Kresse, A. Janotti, C.G. Van de Walle, First-principles calculations for point defects in solids, Rev. Mod. Phys. 86 (2014) 253–305, https://doi.org/10.1103/RevModPhys.86.253.
[110] A. Glensk, B. Grabowski, T. Hickel, J. Neugebauer, Breakdown of the Arrhenius law in describing vacancy formation energies: the importance of local anharmonicity revealed by *ab initio* thermodynamics, Phys. Rev. X 4 (2014) 011018, https://doi.org/10.1103/PhysRevX.4.011018.
[111] Y. Gong, B. Grabowski, A. Glensk, F. Körmann, J. Neugebauer, R.C. Reed, Temperature dependence of the Gibbs energy of vacancy formation of fcc Ni, Phys. Rev. B 97 (2018) 214106, https://doi.org/10.1103/PhysRevB.97.214106.
[112] S. Middleburgh, D. King, G. Lumpkin, M. Cortie, L. Edwards, Segregation and migration of species in the CrCoFeNi high entropy alloy, J. Alloys Compd. 599 (2014) 179–182, https://doi.org/10.1016/j.jallcom.2014.01.135.
[113] W. Chen, X. Ding, Y. Feng, X. Liu, K. Liu, Z. Lu, D. Li, Y. Li, C. Liu, X.-Q. Chen, Vacancy formation enthalpies of high-entropy FeCoCrNi alloy via first-principles calculations and possible implications to its superior radiation tolerance, J. Mater. Sci. Technol. 34 (2018) 355–364, https://doi.org/10.1016/j.jmst.2017.11.005.
[114] S. Zhao, T. Egami, G.M. Stocks, Y. Zhang, Effect of d electrons on defect properties in equiatomic NiCoCr and NiCoFeCr concentrated solid solution alloys, Phys. Rev.

Mater. 2 (2018) 013602, https://doi.org/10.1103/PhysRevMaterials.2.013602.
[115] G. Velişa, E. Wendler, S. Zhao, K. Jin, H. Bei, W.J. Weber, Y. Zhang, Delayed damage accumulation by athermal suppression of defect production in concentrated solid solution alloys, Mater. Res. Lett. 6 (2018) 136–141, https://doi.org/10.1080/21663831.2017.1410863.
[116] S. Baroni, S. de Gironcoli, A. Dal Corso, P. Giannozzi, Phonons and related crystal properties from density-functional perturbation theory, Rev. Mod. Phys. 73 (2001) 515–562, https://doi.org/10.1103/RevModPhys.73.515.
[117] G. Kresse, J. Furthmüller, J. Hafner, *Ab initio* force constant approach to phonon dispersion relations of diamond and graphite, Europhys. Lett. 32 (1995) 729–734, https://doi.org/10.1209/0295-5075/32/9/005.
[118] K. Parlinski, Z.Q. Li, Y. Kawazoe, First-principles determination of the soft mode in cubic $ZrO_2$, Phys. Rev. Lett. 78 (1997) 4063–4066, https://doi.org/10.1103/PhysRevLett.78.4063.
[119] D. Alfè, G.D. Price, M.J. Gillan, Thermodynamics of hexagonal-close-packed iron under Earth's core conditions, Phys. Rev. B 64 (2001) 045123, https://doi.org/10.1103/PhysRevB.64.045123.
[120] Y. Wang, S.-L. Shang, H. Fang, Z.-K. Liu, L.-Q. Chen, First-principles calculations of lattice dynamics and thermal properties of polar solids, npj Comput. Mater. 2 (2016) 16006, https://doi.org/10.1038/npjcompumats.2016.6.
[121] Y. Wang, M. Yan, Q. Zhu, W.Y. Wang, Y. Wu, X. Hui, R. Otis, S.-L. Shang, Z.-K. Liu, L.-Q. Chen, Computation of entropies and phase equilibria in refractory V–Nb–Mo–Ta–W high-entropy alloys, Acta Mater. 143 (2018) 88–101, https://doi.org/10.1016/j.actamat.2017.10.017.
[122] F. Körmann, Y. Ikeda, B. Grabowski, M.H.F. Sluiter, Phonon broadening in high entropy alloys, npj Comput. Mater. 3 (2017) 36, https://doi.org/10.1038/s41524-017-0037-8.
[123] T.B. Boykin, N. Kharche, G. Klimeck, M. Korkusinski, Approximate bandstructures of semiconductor alloys from tight-binding supercell calculations, J. Phys.: Condens. Matter 19 (2007) 036203, https://doi.org/10.1088/0953-8984/19/3/036203.
[124] P.B. Allen, T. Berlijn, D.A. Casavant, J.M. Soler, Recovering hidden Bloch character: unfolding electrons, phonons, and slabs, Phys. Rev. B 87 (2013) 085322, https://doi.org/10.1103/PhysRevB.87.085322.
[125] Y. Ikeda, A. Carreras, A. Seko, A. Togo, I. Tanaka, Mode decomposition based on crystallographic symmetry in the band-unfolding method, Phys. Rev. B 95 (2017) 024305, https://doi.org/10.1103/PhysRevB.95.024305.
[126] Y. Ikeda, F. Körmann, B. Dutta, A. Carreras, A. Seko, J. Neugebauer, I. Tanaka, Temperature-dependent phonon spectra of magnetic random solid solutions, npj Comput. Mater. 4 (2018) 7, https://doi.org/10.1038/s41524-018-0063-1.
[127] K. Jin, S. Mu, K. An, W. Porter, G. Samolyuk, G. Stocks, H. Bei, Thermophysical properties of Ni-containing single-phase concentrated solid solution alloys, Mater. Des. 117 (2017) 185–192, https://doi.org/10.1016/j.matdes.2016.12.079.
[128] F. Körmann, A. Dick, B. Grabowski, T. Hickel, J. Neugebauer, Atomic forces at finite magnetic temperatures: phonons in paramagnetic iron, Phys. Rev. B 85 (2012) 125104, https://doi.org/10.1103/PhysRevB.85.125104.
[129] Y. Ikeda, A. Seko, A. Togo, I. Tanaka, Phonon softening in paramagnetic bcc Fe and its relationship to the pressure-induced phase transition, Phys. Rev. B 90 (2014) 134106, https://doi.org/10.1103/PhysRevB.90.134106.
[130] F. Körmann, P.-W. Ma, S.L. Dudarev, J. Neugebauer, Impact of magnetic fluctuations on lattice excitations in fcc nickel, J. Phys.: Condens. Matter 28 (2016) 076002, https://doi.org/10.1088/0953-8984/28/7/076002.
[131] F. Körmann, B. Grabowski, B. Dutta, T. Hickel, L. Mauger, B. Fultz, J. Neugebauer, Temperature dependent magnon-phonon coupling in bcc Fe from theory and experiment, Phys. Rev. Lett. 113 (2014) 165503, https://doi.org/10.1103/PhysRevLett.113.165503.
[132] A.I. Duff, T. Davey, D. Korbmacher, A. Glensk, B. Grabowski, J. Neugebauer, M.W. Finnis, Improved method of calculating *ab initio* high-temperature thermodynamic properties with application to ZrC, Phys. Rev. B 91 (2015) 214311, https://doi.org/10.1103/PhysRevB.91.214311.
[133] A. Glensk, B. Grabowski, T. Hickel, J. Neugebauer, Understanding anharmonicity in fcc materials: from its origin to *ab initio* strategies beyond the quasiharmonic approximation, Phys. Rev. Lett. 114 (2015) 195901, https://doi.org/10.1103/PhysRevLett.114.195901.
[134] B. Grabowski, S. Wippermann, A. Glensk, T. Hickel, J. Neugebauer, Random phase approximation up to the melting point: impact of anharmonicity and nonlocal many-body effects on the thermodynamics of Au, Phys. Rev. B 91 (2015) 201103, https://doi.org/10.1103/PhysRevB.91.201103.
[135] W.P. Huhn, M. Widom, Prediction of A2 to B2 phase transition in the high-entropy alloy Mo-Nb-Ta-W, JOM 65 (2013) 1772–1779, https://doi.org/10.1007/s11837-013-0772-3.
[136] W.P. Huhn, Thermodynamics from First Principles: Prediction of Phase Diagrams and Materials Properties using Density Functional Theory, Carnegie Mellon University, 2014, http://repository.cmu.edu/dissertations/369.
[137] M. Widom, W.P. Huhn, S. Maiti, W. Steurer, Hybrid Monte Carlo/molecular dynamics simulation of a refractory metal high entropy alloy, Metall. Mater. Trans. A 45 (2014) 196–200, https://doi.org/10.1007/s11661-013-2000-8.
[138] R. Feng, P.K. Liaw, M.C. Gao, M. Widom, First-principles prediction of high-entropy-alloy stability, npj Comput. Mater. 3 (2017) 50, https://doi.org/10.1038/s41524-017-0049-4.
[139] L.J. Santodonato, Y. Zhang, M. Feygenson, C.M. Parish, M.C. Gao, R.J. Weber, J.C. Neuefeind, Z. Tang, P.K. Liaw, Deviation from high-entropy configurations in the atomic distributions of a multi-principal-element alloy, Nat. Commun. 6 (2015) 5964, https://doi.org/10.1038/ncomms6964.
[140] R. Feng, M.C. Gao, C. Zhang, W. Guo, J.D. Poplawsky, F. Zhang, J.A. Hawk, J.C. Neuefeind, Y. Ren, P.K. Liaw, Phase stability and transformation in a light-weight high-entropy alloy, Acta Mater. 146 (2018) 280–293, https://doi.org/10.1016/j.actamat.2017.12.061.
[141] M.C. Gao, M. Widom, Information entropy of liquid metals, J. Phys. Chem. B 122 (2018) 3550–3555, https://doi.org/10.1021/acs.jpcb.7b10723.
[142] F. Körmann, D. Ma, D.D. Belyea, M.S. Lucas, C.W. Miller, B. Grabowski, M.H.F. Sluiter, "Treasure maps" for magnetic high-entropy-alloys from theory and experiment, Appl. Phys. Lett. 107 (2015) 142404, https://doi.org/10.1063/1.4932571.
[143] S. Huang, W. Li, X. Li, S. Schönecker, L. Bergqvist, E. Holmström, L.K. Varga, L. Vitos, Mechanism of magnetic transition in FeCrCoNi-based high entropy alloys, Mater. Des. 103 (2016) 71–74, https://doi.org/10.1016/j.matdes.2016.04.053.
[144] S. Huang, Á. Vida, A. Heczel, E. Holmström, L. Vitos, Thermal expansion, elastic and magnetic properties of FeCoNiCu-based high-entropy alloys using first-principle theory, JOM 69 (2017) 2107–2112, https://doi.org/10.1007/s11837-017-2565-6.
[145] S. Huang, X. Li, H. Huang, E. Holmström, L. Vitos, Mechanical performance of $FeCrCoMnAl_x$ high-entropy alloys from first-principle, Mater. Chem. Phys. 210 (2018) 37–42, https://doi.org/10.1016/j.matchemphys.2017.08.061.
[146] S. Huang, E. Holmström, O. Eriksson, L. Vitos, Mapping the magnetic transition temperatures for medium-and high-entropy alloys, Intermetallics 95 (2018) 80–84, https://doi.org/10.1016/j.intermet.2018.01.016.
[147] A.I. Liechtenstein, M. Katsnelson, V. Antropov, V. Gubanov, Local spin density functional approach to the theory of exchange interactions in ferromagnetic metals and alloys, J. Magn. Magn. Mater. 67 (1987) 65–74, https://doi.org/10.1016/0304-8853(87)90721-9.
[148] A.V. Ruban, S. Shallcross, S. Simak, H.L. Skriver, Atomic and magnetic configurational energetics by the generalized perturbation method, Phys. Rev. B 70 (2004) 125115, https://doi.org/10.1103/PhysRevB.70.125115.
[149] J. Yin, M. Eisenbach, D.M. Nicholson, A. Rusanu, Effect of lattice vibrations on magnetic phase transition in bcc iron, Phys. Rev. B 86 (2012) 214423, https://doi.org/10.1103/PhysRevB.86.214423.
[150] A. Lindmaa, R. Lizárraga, E. Holmström, I. Abrikosov, B. Alling, Exchange interactions in paramagnetic amorphous and disordered crystalline CrN-based systems, Phys. Rev. B 88 (2013) 054414, https://doi.org/10.1103/PhysRevB.88.054414.
[151] A.L. Wysocki, J.K. Glasbrenner, K.D. Belashchenko, Thermodynamics of itinerant magnets in a classical spin-fluctuation model, Phys. Rev. B 78 (2008) 184419, https://doi.org/10.1103/PhysRevB.78.184419.
[152] D.P. Landau, K. Binder, A Guide to Monte Carlo Simulations in Statistical Physics, 4 edn., Cambridge University Press, 2014, https://doi.org/10.1017/CBO9781139696463.
[153] K. Sato, P.H. Dederics, H. Katayama-Yoshida, Curie temperatures of III-V diluted magnetic semiconductors calculated from first principles, Europhys. Lett. 61 (2003) 403–408, https://doi.org/10.1209/epl/i2003-00191-8.
[154] C. Niu, A.J. Zaddach, A.A. Oni, X. Sang, J.W.H. III, J.M. LeBeau, C.C. Koch, D.L. Irving, Spin-driven ordering of Cr in the equiatomic high entropy alloy NiFeCrCo, Appl. Phys. Lett. 106 (2015) 161906, https://doi.org/10.1063/1.4918996.
[155] B. Wu, Z. Xie, J. Huang, J. Lin, Y. Yang, L. Jiang, J. Huang, G. Ye, C. Zhao, S. Yang, B. Sa, Microstructures and thermodynamic properties of high-entropy alloys CoCrCuFeNi, Intermetallics 93 (2018) 40–46, https://doi.org/10.1016/j.intermet.2017.10.018.
[156] P. Singh, A.V. Smirnov, D.D. Johnson, Atomic short-range order and incipient long-range order in high-entropy alloys, Phys. Rev. B 91 (2015) 224204, https://doi.org/10.1103/PhysRevB.91.224204.
[157] A. Tamm, A. Aabloo, M. Klintenberg, M. Stocks, A. Caro, Atomic-scale properties of Ni-based FCC ternary, and quaternary alloys, Acta Mater. 99 (2015) 307–312, https://doi.org/10.1016/j.actamat.2015.08.015.
[158] I. Toda-Caraballo, J.S. Wróbel, S.L. Dudarev, D. Nguyen-Manh, P.E.J. Rivera-Díaz-del Castillo, Interatomic spacing distribution in multicomponent alloys, Acta Mater. 97 (2015) 156–169, https://doi.org/10.1016/j.actamat.2015.07.010.
[159] J.S. Wróbel, D. Nguyen-Manh, M.Y. Lavrentiev, M. Muzyk, S.L. Dudarev, Phase stability of ternary fcc and bcc Fe-Cr-Ni alloys, Phys. Rev. B 91 (2015) 024108, https://doi.org/10.1103/PhysRevB.91.024108.
[160] S.N. Khan, J.B. Staunton, G.M. Stocks, Statistical physics of multicomponent alloys using KKR-CPA, Phys. Rev. B 93 (2016) 054206, https://doi.org/10.1103/PhysRevB.93.054206.
[161] W. Feng, Y. Qi, S. Wang, Effects of short-range order on the magnetic and mechanical properties of $FeCoNi(AlSi)_x$ high entropy alloys, Metals 7 (2017) 482, https://doi.org/10.3390/met7110482.
[162] A. Fernández-Caballero, J.S. Wróbel, P.M. Mummery, D. Nguyen-Manh, Short-range order in high entropy alloys: theoretical formulation and application to Mo-Nb-Ta-V-W system, J. Phase Equilib. Diffus. 38 (2017) 391–403, https://doi.org/10.1007/s11669-017-0582-3.
[163] F. Körmann, A.V. Ruban, M.H.F. Sluiter, Long-ranged interactions in bcc NbMoTaW high-entropy alloys, Mater. Res. Lett. 5 (2017) 35–40, https://doi.org/10.1080/21663831.2016.1198837.
[164] Y. Lederer, C. Toher, K.S. Vecchio, S. Curtarolo, The search for high entropy alloys: a high-throughput ab-initio approach. (2017), https://arxiv.org/abs/1711.
[165] M.C. Nguyen, L. Zhou, W. Tang, M.J. Kramer, I.E. Anderson, C.-Z. Wang, K.-M. Ho, Cluster-expansion model for complex quinary alloys: application to Alnico permanent magnets, Phys. Rev. Appl. 8 (2017) 054016, https://doi.org/10.1103/PhysRevApplied.8.054016.
[166] M. Ogura, T. Fukushima, R. Zeller, P.H. Dederichs, Structure of the high-entropy alloy $Al_xCrFeCoNi$: fcc versus bcc, J. Alloys Compd. 715 (2017) 454–459, https://doi.org/10.1016/j.jallcom.2017.04.318.
[167] Y. Ma, Q. Wang, C. Li, L.J. Santodonato, M. Feygenson, C. Dong, P.K. Liaw,

Chemical short-range orders and the induced structural transition in high-entropy alloys, Scr. Mater. 144 (2018) 64–68, https://doi.org/10.1016/j.scriptamat.2017.09.049.
[168] C.G. Schön, T. Duong, Y. Wang, R. Arróyave, Probing the entropy hypothesis in highly concentrated alloys, Acta Mater. 148 (2018) 263–279, https://doi.org/10.1016/j.actamat.2018.01.028.
[169] P. Singh, A.V. Smirnov, D.D. Johnson, Ta-Nb-Mo-W refractory high-entropy alloys: anomalous ordering behavior and its intriguing electronic origin, Phys. Rev. Mater. 2 (2018) 055004, https://doi.org/10.1103/PhysRevMaterials.2.055004.
[170] P. Singh, A. Sharma, A.V. Smirnov, M.S. Diallo, P.K. Ray, G. Balasubramanian, D.D. Johnson, Design of high-strength refractory complex solid-solution alloys, npj Comput. Mater. 4 (2018) 16, https://doi.org/10.1038/s41524-018-0072-0.
[171] P. Singh, A. Marshal, A.V. Smirnov, A. Sharma, G. Balasubramanian, K.G. Pradeep, D.D. Johnson, Tuning phase-stability and short-range order through Al-doping in $(CoCrFeMn)_{100-x}Al_x$ high entropy alloys, https://arxiv.org/abs/1803.06771, (2018).
[172] B.E. Warren, X-ray Diffraction, Courier Corporation, 1969.
[173] J.M. Cowley, Diffraction Physics, North-Holland, Amsterdam, 1975, https://www.elsevier.com/books/diffraction-physics/cowley/978-0-444-82218-5.
[174] C. Niu, W. Windl, M. Ghazisaeidi, Multi-cell Monte Carlo relaxation method for predicting phase stability of alloys, Scr. Mater. 132 (2017) 9–12, https://doi.org/10.1016/j.scriptamat.2017.01.001.
[175] B. Gyorffy, G. Stocks, Concentration waves and Fermi surfaces in random metallic alloys, Phys. Rev. Lett. 50 (1983) 374–377, https://doi.org/10.1103/PhysRevLett.50.374.
[176] J. Staunton, D.D. Johnson, F. Pinski, Compositional short-range ordering in metallic alloys: band-filling, charge-transfer, and size effects from a first-principles all-electron Landau-type theory, Phys. Rev. B 50 (1994) 1450–1472, https://doi.org/10.1103/PhysRevB.50.1450.
[177] F. Ducastelle, Order and Phase Stability in Alloys, (1991) North-Holland.
[178] J.M. Sanchez, F. Ducastelle, D. Gratias, Generalized cluster description of multicomponent systems, Phys. A 128 (1984) 334–350, https://doi.org/10.1016/0378-4371(84)90096-7.
[179] A. Zunger, First-principles statistical mechanics of semiconductor alloys and intermetallic compounds, Springer, 1994, pp. 361–419, https://doi.org/10.1007/978-1-4615-2476-2_23.
[180] J.W.D. Connolly, A.R. Williams, Density-functional theory applied to phase transformations in transition-metal alloys, Phys. Rev. B 27 (1983) 5169–5172, https://doi.org/10.1103/PhysRevB.27.5169.
[181] I. Toda-Caraballo, P.E.J. Rivera-Díaz-del Castillo, Modelling solid solution hardening in high entropy alloys, Acta Mater. 85 (2015) 14–23, https://doi.org/10.1016/j.actamat.2014.11.014.
[182] M.Y. Lavrentiev, D. Nguyen-Manh, S. Dudarev, Magnetic cluster expansion model for bcc-fcc transitions in Fe and Fe-Cr alloys, Phys. Rev. B 81 (2010) 184202, https://doi.org/10.1103/PhysRevB.81.184202.
[183] M.Y. Lavrentiev, J. Wróbel, D. Nguyen-Manh, S. Dudarev, M. Ganchenkova, Magnetic cluster expansion model for random and ordered magnetic face-centered cubic Fe-Ni-Cr alloys, J. Appl. Phys. 120 (2016) 043902, https://doi.org/10.1063/1.4958981.
[184] M. Widom, Entropy and diffuse scattering: comparison of NbTiVZr and CrMoNbV, Metall. Mater. Trans. A 47 (2016) 3306–3311, https://doi.org/10.1007/s11661-015-3095-x.
[185] A. Sher, M. van Schilfgaarde, A.-B. Chen, W. Chen, Quasichemical approximation in binary alloys, Phys. Rev. B 36 (1987) 4279, https://doi.org/10.1103/PhysRevB.36.4279.
[186] S. Curtarolo, W. Setyawan, G.L. Hart, M. Jahnatek, R.V. Chepulskii, R.H. Taylor, S. Wang, J. Xue, K. Yang, O. Levy, M.J. Mehl, H.T. Stokes, D.O. Demchenko, D. Morgan, AFLOW: an automatic framework for high-throughput materials discovery, Comp. Mater. Sci. 58 (2012) 218–226, https://doi.org/10.1016/j.commatsci.2012.02.005.
[187] F. Tian, L.K. Varga, N. Chen, L. Delczeg, L. Vitos, *Ab initio* investigation of high-entropy alloys of 3*d* elements, Phys. Rev. B 87 (2013) 075144, https://doi.org/10.1103/PhysRevB.87.075144.
[188] A.J. Zaddach, C. Niu, C.C. Koch, D.L. Irving, Mechanical properties and stacking fault energies of NiFeCrCoMn high-entropy alloy, JOM 65 (2013) 1780–1789, https://doi.org/10.1007/s11837-013-0771-4.
[189] É. Fazakas, V. Zadorozhnyy, L.K. Varga, A. Inoue, D.V. Louzguine-Luzgin, F. Tian, L. Vitos, Experimental and theoretical study of $Ti_{20}Zr_{20}Hf_{20}Nb_{20}X_{20}$ (X = V or Cr) refractory high-entropy alloys, Int. J. Refract. Met. Hard Mater. 47 (2014) 131–138, https://doi.org/10.1016/j.ijrmhm.2014.07.009.
[190] F.Y. Tian, L.K. Varga, N.X. Chen, J. Shen, L. Vitos, *Ab initio* design of elastically isotropic $TiZrNbMoV_x$ high-entropy alloys, J. Alloys Compd. 599 (2014) 19–25, https://doi.org/10.1016/J.Jallcom.2014.01.237.
[191] P. Cao, X. Ni, F. Tian, L.K. Varga, L. Vitos, *Ab initio* study of $Al_xMoNbTiV$ high-entropy alloys, J. Phys.: Condens. Matter 27 (2015) 075401, https://doi.org/10.1088/0953-8984/27/7/075401.
[192] S. Li, X. Ni, F. Tian, *Ab initio* predicted alloying effects on the elastic properties of $Al_xHf_{1-x}NbTaTiZr$ high entropy alloys, Coatings 5 (2015) 366–377, https://doi.org/10.3390/coatings5030366.
[193] X. Li, F. Tian, S. Schonecker, J. Zhao, L. Vitos, *Ab initio*-predicted micro-mechanical performance of refractory high-entropy alloys, Sci. Rep. 5 (2015) 12334, https://doi.org/10.1038/srep12334.
[194] C. Niu, A.J. Zaddach, C.C. Koch, D.L. Irving, First principles exploration of near-equiatomic NiFeCrCo high entropy alloys, J. Alloys Compd. 672 (2016) 510–520, https://doi.org/10.1016/j.jallcom.2016.02.108.
[195] F. Tian, D. Wang, J. Shen, Y. Wang, An *ab initio* investigation of ideal tensile and shear strength of TiVNbMo high-entropy alloy, Mater. Lett. 166 (2016) 271–275, https://doi.org/10.1016/j.matlet.2015.12.064.
[196] H. Ge, F. Tian, Y. Wang, Elastic and thermal properties of refractory high-entropy alloys from first-principles calculations, Comp. Mater. Sci. 128 (2017) 185–190, https://doi.org/10.1016/j.commatsci.2016.11.035.
[197] S. Huang, A. Vida, W. Li, D. Molnár, S.K. Kwon, E. Holmström, B. Varga, L.K. Varga, L. Vitos, Thermal expansion in FeCrCoNiGa high-entropy alloy from theory and experiment, Appl. Phys. Lett. 110 (2017) 241902, https://doi.org/10.1063/1.4985724.
[198] F. Tian, L.K. Varga, L. Vitos, Predicting single phase CrMoWX high entropy alloys from empirical relations in combination with first-principles calculations, Intermetallics 83 (2017) 9–16, https://doi.org/10.1016/j.intermet.2016.12.007.
[199] L.-Y. Tian, G. Wang, J.S. Harris, D.L. Irving, J. Zhao, L. Vitos, Alloying effect on the elastic properties of refractory high-entropy alloys, Mater. Des. 114 (2017) 243–252, https://doi.org/10.1016/j.matdes.2016.11.079.
[200] X. Li, First-principles study of the third-order elastic constants and related anharmonic properties in refractory high-entropy alloys, Acta Mater. 142 (2018) 29–36, https://doi.org/10.1016/j.actamat.2017.09.041.
[201] X. Li, S. Schönecker, W. Li, L.K. Varga, D.L. Irving, L. Vitos, Tensile and shear loading of four fcc high-entropy alloys: a first-principles study, Phys. Rev. B 97 (2018) 094102, https://doi.org/10.1103/PhysRevB.97.094102.
[202] B. Feng, M. Widom, Elastic stability and lattice distortion of refractory high entropy alloys, Mater. Chem. Phys. 210 (2018) 309–314, https://doi.org/10.1016/j.matchemphys.2017.06.038.
[203] H. Yao, J. Qiao, J. Hawk, H. Zhou, M. Chen, M. Gao, Mechanical properties of refractory high-entropy alloys: experiments and modeling, J. Alloys Compd. 696 (2017) 1139–1150, https://doi.org/10.1016/j.jallcom.2016.11.188.
[204] Y. Ye, Y. Zhang, Q. He, Y. Zhuang, S. Wang, S. Shi, A. Hu, J. Fan, Y. Yang, Atomic-scale distorted lattice in chemically disordered equimolar complex alloys, Acta Mater. 150 (2018) 182–194, https://doi.org/10.1016/j.actamat.2018.03.008.
[205] S.-M. Zheng, W.-Q. Feng, S.-Q. Wang, Elastic properties of high entropy alloys by MaxEnt approach, Comput. Mater. Sci. 142 (2018) 332–337, https://doi.org/10.1016/j.commatsci.2017.09.060.
[206] Ł. Rogal, F. Czerwinski, P. Jochym, L. Litynska-Dobrzynska, Microstructure and mechanical properties of the novel Hf25Sc25Ti25Zr25 equiatomic alloy with hexagonal solid solutions, Mater. Des. 92 (2016) 8–17, https://doi.org/10.1016/j.matdes.2015.11.104.
[207] M.J. Mehl, J.E. Osburn, D.A. Papaconstantopoulos, B.M. Klein, Structural properties of ordered high-melting-temperature intermetallic alloys from first-principles total-energy calculations, Phys. Rev. B 41 (1990) 10311–10323, https://doi.org/10.1103/PhysRevB.41.10311.
[208] G. Steinle-Neumann, L. Stixrude, R.E. Cohen, First-principles elastic constants for the hcp transition metals Fe, Co, and Re at high pressure, Phys. Rev. B 60 (1999) 791–799, https://doi.org/10.1103/PhysRevB.60.791.
[209] G. Grimvall, Thermophysical Properties of Materials, Elsevier, 1999, http://www.sciencedirect.com/science/book/9780444827944.
[210] S. Pugh, XCII. Relations between the elastic moduli and the plastic properties of polycrystalline pure metals, Lond. Edinb. Dubl. Philos. Mag. 45 (1954) 823–843, https://doi.org/10.1080/14786440808520496.
[211] D.G. Pettifor, Theoretical predictions of structure and related properties of intermetallics, Mater. Sci. Technol. 8 (1992) 345–349, https://doi.org/10.1179/mst.1992.8.4.345.
[212] C. Zener, Elasticity and Anelasticity of Metals, University of Chicago Press, 1948.
[213] A.G. Every, General closed-form expressions for acoustic waves in elastically anisotropic solids, Phys. Rev. B 22 (1980) 1746–1760, https://doi.org/10.1103/PhysRevB.22.1746.
[214] P. Souvatzis, O. Eriksson, M. Katsnelson, S. Rudin, Entropy driven stabilization of energetically unstable crystal structures explained from first principles theory, Phys. Rev. Lett. 100 (2008) 095901, https://doi.org/10.1103/PhysRevLett.100.095901.
[215] M. Born, K. Huang, Dynamical Theory of Crystal Lattices, Clarendon Press, 1954.
[216] W.Y. Wang, S.L. Shang, Y. Wang, F. Han, K.A. Darling, Y. Wu, X. Xie, O.N. Senkov, J. Li, X.D. Hui, K.A. Dahmen, P.K. Liaw, L.J. Kecskes, Z.-K. Liu, Atomic and electronic basis for the serrations of refractory high-entropy alloys, npj Comput. Mater. 3 (2017) 23, https://doi.org/10.1038/s41524-017-0024-0.
[217] C. Dong, Q. Wang, J. Qiang, Y. Wang, N. Jiang, G. Han, Y. Li, J. Wu, J. Xia, From clusters to phase diagrams: composition rules of quasicrystals and bulk metallic glasses, J. Phys. D: Appl. Phys. 40 (2007) R273–R291, https://doi.org/10.1039/C5RA28088E.
[218] C. Varvenne, A. Luque, W.A. Curtin, Theory of strengthening in fcc high entropy alloys, Acta Mater. 118 (2016) 164–176, https://doi.org/10.1016/j.actamat.2016.07.040.
[219] C. Varvenne, G. Leyson, M. Ghazisaeidi, W. Curtin, Solute strengthening in random alloys, Acta Mater. 124 (2017) 660–683, https://doi.org/10.1016/j.actamat.2016.09.046.
[220] M.C. Gao, D.E. Alman, Searching for next single-phase high-entropy alloy compositions, Entropy 15 (2013) 4504–4519, https://doi.org/10.3390/e15104504.
[221] T. Egami, M. Ojha, O. Khorgolkhuu, D.M. Nicholson, G.M. Stocks, Local electronic effects and irradiation resistance in high-entropy alloys, JOM 67 (2015) 2345–2349, https://doi.org/10.1007/s11837-015-1579-1.
[222] M.C. Gao, B. Zhang, S. Yang, S. Guo, Senary refractory high-entropy alloy HfNbTaTiVZr, Metall. Mater. Trans. A 47 (2016) 3333–3345, https://doi.org/10.1007/s11661-015-3105-z.
[223] H.S. Oh, D. Ma, G.P. Leyson, B. Grabowski, E.S. Park, F. Körmann, D. Raabe, Lattice distortions in the FeCoNiCrMn high entropy alloy studied by theory and experiment, Entropy 18 (2016) 321, https://doi.org/10.3390/e18090321.

[224] N.L. Okamoto, K. Yuge, K. Tanaka, H. Inui, E.P. George, Atomic displacement in the CrMnFeCoNi high-entropy alloy — a scaling factor to predict solid solution strengthening, AIP Adv. 6 (2016) 125008, https://doi.org/10.1063/1.4971371.
[225] O. Grässel, L. Krüger, G. Frommeyer, L. Meyer, High strength Fe–Mn–(Al, Si) TRIP/TWIP steels development — properties — application, Int. J. Plast. 16 (2000) 1391–1409, https://doi.org/10.1016/S0749-6419(00)00015-2.
[226] D. Pierce, J. Jiménez, J. Bentley, D. Raabe, C. Oskay, J. Wittig, The influence of manganese content on the stacking fault and austenite/$\epsilon$-martensite interfacial energies in Fe–Mn–(Al–Si) steels investigated by experiment and theory, Acta Mater. 68 (2014) 238–253, https://doi.org/10.1016/j.actamat.2014.01.001.
[227] P.R. Thornton, T.E. Mitchell, P.B. Hirsch, The dependence of cross-slip on stacking-fault energy in face-centred cubic metals and alloys, Philos. Mag. 7 (1962) 1349–1369, https://doi.org/10.1080/14786436208213168.
[228] S. Huang, W. Li, S. Lu, F. Tian, J. Shen, E. Holmström, L. Vitos, Temperature dependent stacking fault energy of FeCrCoNiMn high entropy alloy, Scr. Mater. 108 (2015) 44–47, https://doi.org/10.1016/j.scriptamat.2015.05.041.
[229] L. Patriarca, A. Ojha, H. Sehitoglu, Y.I. Chumlyakov, Slip nucleation in single crystal FeNiCoCrMn high entropy alloy, Scr. Mater. 112 (2016) 54–57, https://doi.org/10.1016/j.scriptamat.2015.09.009.
[230] M. Beyramali Kivy, M. Asle Zaeem, Generalized stacking fault energies, ductilities, and twinnabilities of CoCrFeNi-based face-centered cubic high entropy alloys, Scr. Mater. 139 (2017) 83–86, https://doi.org/10.1016/j.scriptamat.2017.06.014.
[231] Y.H. Zhang, Y. Zhuang, A. Hu, J.J. Kai, C.T. Liu, The origin of negative stacking fault energies and nano-twin formation in face-centered cubic high entropy alloys, Scr. Mater. 130 (2017) 96–99, https://doi.org/10.1016/j.scriptamat.2016.11.014.
[232] Z. Zhang, H. Sheng, Z. Wang, B. Gludovatz, Z. Zhang, E.P. George, Q. Yu, S.X. Mao, R.O. Ritchie, Dislocation mechanisms and 3D twin architectures generate exceptional strength-ductility-toughness combination in CrCoNi medium-entropy alloy, Nat. Commun. 8 (2017) 14390, https://doi.org/10.1038/ncomms14390.
[233] S. Alkan, A. Ojha, H. Sehitoglu, Determination of latent hardening response for FeNiCoCrMn for twin-twin interactions, Acta Mater. 147 (2018) 149–164, https://doi.org/10.1016/j.actamat.2017.12.058.
[234] H. Huang, X. Li, Z. Dong, W. Li, S. Huang, D. Meng, X. Lai, T. Liu, S. Zhu, L. Vitos, Critical stress for twinning nucleation in CrCoNi-based medium and high entropy alloys, Acta Mater. 149 (2018) 388–396, https://doi.org/10.1016/j.actamat.2018.02.037.
[235] C. Niu, C.R. LaRosa, J. Miao, M.J. Mills, M. Ghazisaeidi, Magnetically-driven phase transformation strengthening in high entropy alloys, Nat. Commun. 9 (2018) 1363, https://doi.org/10.1038/s41467-018-03846-0.
[236] P.J.H. Denteneer, W. van Haeringen, Stacking-fault energies in semiconductors from first-principles calculations, J. Phys. C 20 (1987) L883–L887, https://doi.org/10.1088/0022-3719/20/32/001.
[237] A. Abbasi, A. Dick, T. Hickel, J. Neugebauer, First-principles investigation of the effect of carbon on the stacking fault energy of Fe–C alloys, Acta Mater. 59 (2011) 3041–3048, https://doi.org/10.1016/j.actamat.2011.01.044.
[238] N. Medvedeva, M. Park, D.V. Aken, J. Medvedeva, First-principles study of Mn, Al and C distribution and their effect on stacking fault energies in fcc Fe, J. Alloys Compd. 582 (2014) 475–482, https://doi.org/10.1016/j.jallcom.2013.08.089.
[239] Z. Li, K.G. Pradeep, Y. Deng, D. Raabe, C.C. Tasan, Metastable high-entropy dual-phase alloys overcome the strength-ductility trade-off, Nature 534 (2016) 227–230, https://doi.org/10.1038/nature17981.
[240] K. Jasiewicz, S. Kaprzyk, J. Tobola, Interplay of crystal structure preference and magnetic ordering in high entropy CrCoFeNiAl alloys, Acta Phys. Pol. A 133 (2018) 511–513, https://doi.org/10.12693/APhysPolA.133.511.
[241] K. Jin, B.C. Sales, G.M. Stocks, G.D. Samolyuk, M. Daene, W.J. Weber, Y. Zhang, H. Bei, Tailoring the physical properties of Ni-based single-phase equiatomic alloys by modifying the chemical complexity, Sci. Rep. 6 (2016) 20159, https://doi.org/10.1038/srep20159.
[242] O. Schneeweiss, M. Friák, M. Dudová, D. Holec, M. Šob, D. Kriegner, V. Holý, P. Beran, E.P. George, J. Neugebauer, A. Dlouhý, Magnetic properties of the CrMnFeCoNi high-entropy alloy, Phys. Rev. B 96 (2017) 014437, https://doi.org/10.1103/PhysRevB.96.014437.
[243] S. Huang, H. Huang, W. Li, D. Kim, S. Lu, X. Li, E. Holmström, S.K. Kwon, L. Vitos, Twinning in metastable high-entropy alloys, Nat. Commun. 9 (2018) 2381, https://doi.org/10.1038/s41467-018-04780-x.
[244] F.X. Zhang, S. Zhao, K. Jin, H. Bei, D. Popov, C. Park, J.C. Neuefeind, W.J. Weber, Y. Zhang, Pressure-induced fcc to hcp phase transition in Ni-based high entropy solid solution alloys, Appl. Phys. Lett. 110 (2017) 011902, https://doi.org/10.1063/1.4973627.
[245] J. Ding, Q. Yu, M. Asta, R.O. Ritchie, Tunable stacking fault energies bytailoring local chemical order in CrCoNi medium-entropy alloys. https://arxiv.org/abs/1806.00718.
[246] M. Heidelmann, M. Feuerbacher, D. Ma, B. Grabowski, Structural anomaly in the high-entropy alloy ZrNbTiTaHf, Intermetallics 68 (2016) 11–15, https://doi.org/10.1016/j.intermet.2015.08.013.
[247] W.Y. Wang, J. Wang, D. Lin, C. Zou, Y. Wu, Y. Hu, S.-L. Shang, K.A. Darling, Y. Wang, X. Hui, J. Li, L.J. Kecskes, P.K. Liaw, Z.-K. Liu, Revealing the microstates of body-centered-cubic (BCC) equiatomic high entropy alloys, J. Phase Equilib. Diffus. 38 (2017) 404–415, https://doi.org/10.1007/s11669-017-0565-4.